Improving upon the dosimetry of yttrium-90 radioembolization for primary and metastatic hepatic tumours

S. Peter Kim

Biomedical and Biological Engineering

McGill University, Montreal

August, 2021

A thesis submitted to McGill University

in partial fulfillment of the requirements

for the degree of Master of Engineering

"Education is our passport to the future, for tomorrow belongs only to the people who prepare for it today."

- Malcolm X

ABSTRACT

Radioembolization has seen a great resurgence in interest due to increases in computing resources and advances in image reconstruction algorithms. In particular, radioembolization has seen significant research interest in its dosimetry. Dosimetry is the study of absorbed doses and provides quantitative measures to help determining patient efficacy and safety values for radiation treatments. The purpose of this work was to build upon the existing radioembolization knowledge and improve upon its dosimetry. This was achieved through two parts. In the first step, a comprehensive literature review explored all the dosimetric methodologies available and elucidated the underlying rationales behind each dosimetry model. It was found that radioembolization's dosimetry was transitioning from MIRD based modeling to more image-based methodologies and applying dosemetric assumptions derived from microsphere biodistributions. More importantly, many dosimetric implementations were found to be heterogeneously utilized without any standardization. In the second step, important dosimetry parameters were characterized with the goal to measure any dosimetric uncertainties and analyze its causes. The implementation variations in self-calibration and tissue mass density parameters were investigated. These dose estimates were calculated with the mono-compartmental and local deposition methods to provide quantitative analysis through a clinical dataset. Our results suggested that the organs at risk calibration should be implemented for count to activity conversions and that homogeneous tissue mass densities would be an ideal implementation for dosimetry. To help address a common imaging limitation within the liver, a practical, but empirically supported mean dose correction was derived. Lastly, a Monte Carlo benchmark dosimetry software was created for any future dosimetry benchmarking needs.

Acknowledgements

I would like to thank my supervisor and mentor, Dr Shirin Abbasinejad Enger who has always made the time to both advocate for my professional and personal growth. She has been always open to answer any questions. Without her support, I would not be where I am today. Furthermore, I would like to thank Claire Cohalan and Daniel Juneau for providing their clinical insights and their constant support.

I also acknowledge support by Collaborative Health Research Project (CHRP grant number 523394-18) and the Canada Research Chair (Grant numbers 252135 and 252136).

Contents

List of Figures

List of Tables

List of Abbreviations

AAPM	American Association of Physicists in Medicine
CT	Computed Tomography
DPK	Dose Point Kernel
DVH	Cumulative Dose Volume Histogram
HU	Houndsfield Unit or CT unit
FWHM	Full Width Half Max
Geant4	**GE**ometry **AN**d **T**racking 4
IAEA	International Atomic Energy Agency
ICRU	**I**nternational **C**ommission on **R**adiation **U**nits and measurements
LOR	Line Of Response
MEGP	Medium Energy and General Purpose
MLEM	Maximum Likelihood Expectation Maximum
MIRD	Medical Internal Radiation Dose
MRI	Magnetic Resonance Imaging
OSEM	Ordered Subset Expectation Maximum
PET	Positron Emission Tomography
ROI	Region(s) of Interest
SPECT	Single Photon Emission Computed Tomography
TG	Task Group
^{90}**Y**	Yttrium-90

List of Symbols

A	radioactive activity	Bq
A	atomic mass number	
β^-	electron/beta particle	
β^+	positron particle	
Bq	activity	s^{-1}
E	energy	eV
ϵ	initial photon energy	J
E_{max}	maximum energy	eV
E_{mean}	average energy	eV
$I(x)$	photon beam intensity as a function of distance travelled	$\mathrm{lm/cm}$
$I(0)$	photon beam intensity before travelling any distance	lm
$t_{1/2}$	half-life	s
m	mass	kg
Z	atomic number	
λ	decay constant	s^{-1}
μ	linear attenuation coefficient	cm^{-1}
γ	gamma particle	

This thesis is dedicated to my brother, Jean Kim.

Chapter 1

Introduction

Cancer is defined as an abnormal cell growth with the potential to spread to other parts of the body. Over the years, different approaches have been developed to combat cancer. Several cancer hallmarks have been defined in the biological realm, which has lead to the greater understanding of the biological mechanisms in cancer formation and, consequently, in ways to combat them (Hanahan and Weinberg, 2011). Treatments taking advantage of such biological mechanisms are defined as molecular therapies.

Radiation therapy, or radiotherapy, is a select group of treatments that apply radiation to either control or kill cancer. Rather than combat cancer through biological mechanisms, ionizing radiation is used to directly kill cancerous cells by irrevocably damaging them. Comprehensive planning before treatment allows for precise and safe treatment delivery. Radiotherapy is generally divided into two categories: external beam and internal radiation. External beam therapy directs ionizing radiation to a particular tumour site, most commonly through the MV photons created with a linear accelerator. This treatment is external because radiation is directed from outside the patient. On the contrary, treatments where radiation stems from inside the patient are called internal radiation therapies. These therapies include brachytherapy and targeted radiation therapies.

Brachytherapy is a form of radiation treatment that implants a radioactive source inside or near a patient's tumour providing a high dose to the tumour and a low dose to

the normal tissues. Targeted radiation therapies are an interplay between brachytherapy and molecular therapies. A radioactive source is connected to a molecular probe that targets tumour cells through biological mechanisms. The main difference between internal radiation treatments lie in their targeting ability. Brachytherapy treatments stay localized in one area; however, targeted radiation therapies have biological targets that are more systemic in nature.

1.1 Radioembolization

Radioembolization is a radiation treatment that uniquely falls within no distinct category. Due to its open source nature and nuclear imaging requirements, radioembolization is labeled as a nuclear medicine based internal radiation therapy. However, "seeds" or microspheres containing radioactive yttrium-90 (^{90}Y) sources are injected near tumour sites, similar to brachytherapy, while physiological mechanisms are used for targeted tumour treatment, akin to targeted radiation therapies. In this capacity, radioemboliztion may be categorized as a hybrid between brachytherapy and targeted radiation therapy.

With technological advancements in imaging and reconstruction methodologies improving its therapeutic potential, clinical trials have been conducted testing radioembolization as a first-line curative therapy (Salem et al., 2019; Tai et al., 2020; Edeline et al., 2020). Importantly, questions regarding its efficacy and safety have arisen. These questions are tied to its dosimetry.

1.2 Dosimetry

Fundamental to any radiation treatment, dosimetry is the quantitative study of measuring, calculating, and assessing the effects of radiation on an object, typically within

the human body. These dosimetric metrics create quantitative references for comparisons that allow for the optimization of maximally irradiating tumours while sparing neighboring healthy tissues. The importance of dosimetry is profound. Without dosimetry, radiation treatments cease to be useful. Every treatment becomes a shot in the dark without a benchmark for comparison.

1.3 Objectives

The main objective of this thesis was to improve upon the dosimetry of radioembolization. As a multi-disciplinary treatment, the first goal was to understand radioembolization as a whole from its treatment rationales to all the available technological modalities utilized. Once the entire treatment process was understood, the relevant dosimetric variables could be found. This was accomplished through a comprehensive literature review investigating both the clinical and technical variables relevant within radioembolization. The second goal was to characterize any dosimetric uncertainties and improve upon them. This was achieved by (1) creating state-of-the-art dosimetric algorithms, (2) utilizing patient data, and (3) applying dosimetric algorithms on patient data to compare the absorbed dose differences in different dosimetric variables. These research objective were focused on SPECT/CT Yttrium-90 (^{90}Y) image-based dosimetry.

1.4 Contribution of Authors

This thesis was written entirely by S. Peter Kim. The thesis core work consists of two manuscripts; one that has been published in Physica Medica, and another that will be submitted for peer-review.

The first manuscript, "A guide to ^{90}Y radioembolization and its dosimetry", S. Peter

Kim, Claire Cohalan, Neil Kopek, and Shirin A. Enger, presents a review paper conducted by S. Peter Kim. Claire Cohalan provided the necessary imaging expertise related to medical imaging while Neil Kopek provided the clinical insights related to the Liver. Shirin. A. Enger provided general guidance and supervision.

The second manuscript "Characterizing SPECT/CT Dosimetry following radioembolization with Yttrium-90 microspheres", S. Peter Kim, Daniel Juneau, Claire Cohalan, Shirin A. Enger, presents work conducted by S. Peter Kim. Daniel Juneau provided clinical guidance and direction related to ^{90}Y's treatment. Claire Cohalan provided imaging expertise and analysis support. Shirin A. Enger provided general guidance and supervision.

Chapter 2

Background

Radioembolization is a radiation treatment at its core. As an internal radiation therapy, medical imaging is required to non-invasively visualize the locations of these radioactive sources. Thus, a thorough understanding of physics principles related to radioactivity, radiation, interaction with matter, medical imaging, and absorbed dose is required to understand radioembolization's benefits and limitations.

2.1 Radioactivity

2.1.1 Decay processes

Radioembolization utilizes a radioactive source to kill cancer. A radioactive source is an atom that is unstable and returns to a more stable form. This process of returning to its stable form is called radioactive decay. Radioactive decay, also known as nuclear decay, decay, and nuclear disintegration is a stochastic process by which an unstable parent nucleus emits a particle to transform into a more stable daughter nucleus (*Nuclear Medicine Physics* 2015). This daughter nucleus may be radioactive itself and further decay to a more stable form.

There are many different decay processes that may occur and are dependent on the radioactive source in question. Radioactive sources may decay through a single decay process or have multiple types of decays. A decay process defines the type of particle

that is emitted from the nucleus, which then provides a general indication of the particle interactions that may occur. Radioembolization utilizes ^{90}Y, which primarily decays through beta (β^-) emission, but may sporadically emit positron (β^+) and gamma (γ) particles. Typical decay schemes utilize nomenclature including Z and A. In this context, Z stands for atomic number i.e. the number of protons in an atom while A stands for atomic mass number, which is the sum of protons and neutrons. ^{90}Y specific decay processes are described below.

Beta decay

(β^-) or beta decay involves a neutron-rich parent nucleus P. The neutron in the parent nucleus P is transformed to produce a proton in the daughter nucleus D and ejects an electron (β^-) and an electronic antineutrino $(\bar{v_e})$. The general relationship for β^- decay is given:

$$ {}^{A}_{Z}P- >^{A}_{Z+1} D + \beta^- + \bar{v}_e \tag{2.1} $$

Positron decay

In positron or β^+ decay, a proton-rich parent nucleus P transforms a proton into a neutron and ejects a positron and an electronic neutrino (v_e). The general relationship for β^+ decay is shown as:

$$ {}^{A}_{Z}P- >^{A}_{Z-1} D + \beta^+ + v_e \tag{2.2} $$

Gamma decay

After another mode of ^{90}Y decay, gamma decay occurs when the nucleus is left in an excited state with excess energy (*Nuclear Medicine Physics* 2015). This excess energy is released and emitted through the form of a photon. When a photon is created in

this way, it is called a gamma ray. Gamma decay is represented below where ${}^{A}_{Z}P^{*}$ represents an excited nucleus:

$$ {}^{A}_{Z}P^{*} - >^{A}_{Z} D + \gamma \tag{2.3} $$

2.1.2 Activity

When a radioactive source is characterized, the decay process is used to define the type of particle emitted. However, a radioactive source is also typically characterized by another metric called activity. Activity is defined as a rate in which all decay processes occur per unit of time. Activity has units in decays per second or Bequerel (Bq).

A similar, but distinct metric, the radioactive decay constant λ is the probability that a specific atom or radioactive source will decay per unit time. This constant is the defining characteristic between different radioactive nuclides. It is expressed below where $t_{1/2}$ represents the half-life of a specific nuclide:

$$ \lambda_{nuclide} = \frac{ln2}{t_{1/2}} \tag{2.4} $$

A general formalism may be defined for all radioactive decay processes through the activity $A(t)$ and its radioactive decay constant (λ) (*Nuclear Medicine Physics* 2015). Assuming the simplest form of radioactive decay occurs, a radioactive parent P decays into a single daughter nucleus D with a decay constant λ_p. This is mathematically represented by the activity of parent nuclei P at time t with an initial activity $A_p(0)$ and is seen below:

$$ A_p(t) = A_p(0)e^{-\lambda_p t} \tag{2.5} $$

Equation 2.5 may be expanded to include $N_p(0)$, which represents the initial number of identical radioactive atoms.

$$A_p(t) = A_p(0)e^{-\lambda_p t} = \lambda_p N_p(0)e^{-\lambda_p t} \tag{2.6}$$

Called the decay law, equation 2.5 and 2.6 defines the rate at which decays occur after a period of time and applies to all radioactive nuclides regardless of their decay process (*Nuclear Medicine Physics* 2015).

2.2 Radiation physics and dosimetry

2.2.1 Ionizing vs non-ionizing radiation

Activity and decay processes measure an intrinsic property of a specific radioactive atom; however, such metrics do not provide information on how these emitted particles interact with matter. All emitted particles have a kinetic energy or radiation that they may impart to their traveling medium. Depending on their particle type and kinetic energy, they will interact differently with matter. These emitted particles may be classified as ionizing or non-ionizing particles. Ionizing particles are those that may create ions and are divided into two categories: directly and indirectly ionizing. In contrast, non-ionizing particles do not have sufficient energy to remove particles from an atom and, thus, are defined as particles that cannot create ions within their interacting medium.

Directly ionizing particles are charged and include electrons, protons, alpha particles and heavy ions. These ionizing particles interact through Coulomb interactions between the medium's nuclei or orbital electrons (*Quantitative Nuclear Medicine Imaging: Concepts, Requirements and Methods* 2014). Indirectly ionizing particles are particles that lack any charge such as photons (γ rays and X-rays) and neutrons, but can still cause ionizing effects. These particles ionize matter through a two-step process. First, a neutral particle interacts with the medium's atoms to release a charged particle. Second,

the released charged particles then interact within the medium. Within radioemoblization, electron and photon interactions are the main particle interactions typically studied.

2.2.2 Electron interactions

Electron interactions occur through Coloumb forces when an incident electron interacts with atoms within a medium. The type of electron interaction depends on the location of the incident electron's collision within a medium's atoms. When an incident electron interacts with an orbital electron, either an ionization or excitation event may occur. An ionization event is when an orbital electron is ejected from its orbital to its surrounding. This ejected electron may then undergo further interactions. An excitation event is defined as a transfer of orbital electron to a higher shell (Podgoršak et al., 2006). An incident electron may also interact with the nuclei of the medium's atom. When this occurs, an electron will lose energy in a slowing down process that is called bremsttrahlung and emit a photon. The loss of energy from the electron may be between zero and the initial electron's kinetic energy. The resulting bremsttrahlung photon will have the energy that was lost due to deceleration.

2.2.3 Photon interactions

Photons may undergo various interactions with the atoms of the medium where the probability of an interaction depends on its energy hv and the atomic number Z of the medium's atoms (Podgoršak et al., 2006). Within imaging and radiation treatments, the photoelectric effect, Rayleigh scattering, and Compton scattering are the three main interactions that may occur. In the context of photon interactions, a tightly bound electron is defined as having a binding energy E_B that is higher than the energy of any interacting photon while a free electron had a binding energy that was lower than the interacting photon energy. Fig. 2.1 demonstrates the relative predominance of

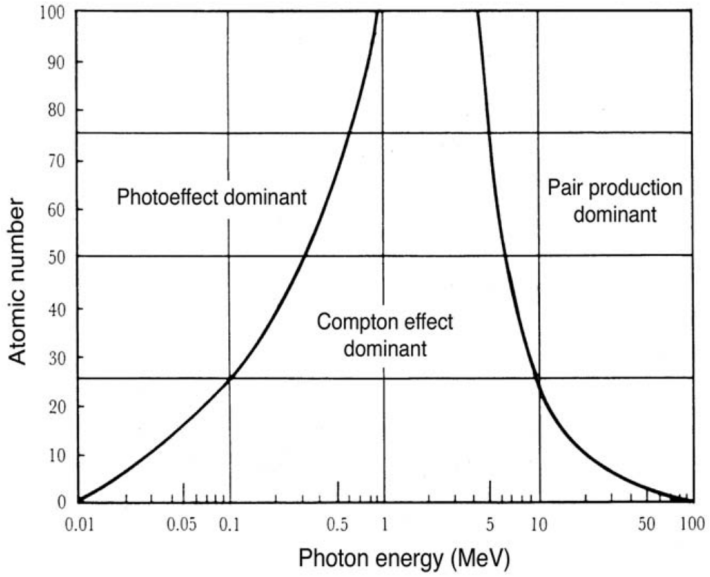

FIGURE 2.1: The energy hv of the photon and on the atomic number Z of the medium's material determines the probability of a photon interaction. Reproduced from (Podgoršak et al., 2006)

three photon interactions. In general, the photoelectric effect predominates at low photon energies, the Compton effect at intermediate energies and pair production at high photon energies. Although not completely relevant to radioembolization SPECT/CT dosimetry, pair production is a dominant interaction that creates an electron and a positron when a high energy photon interacts with the electrons of the medium.

Photoelectric effect

In the photoelectric effect, a photon interacts with a tightly bound electron in a medium and is absorbed while an orbital electron (photoelectron) is ejected from the atom. The photoelectric effect further creates a vacancy in an orbital electron shell, which in turn may lead to the emission of characteristic x rays. The energy of the photoelectron E_K is given as:

$$E_K = hv - E_B \tag{2.7}$$

The probability that a photoelectric event occurs is proportional to $Z^4/(hv)^3$.

Rayleigh (Coherent) scattering

In Rayleigh scattering, the photon interacts with a orbital electron and is scattered at a small angle without losing any of its energy. No energy is transferred to a charged particle (i.e. electron) and plays an inconsequential role in dosimetry, but is important for imaging. The probability for Rayleigh scattering is proportional to $(Z/hv)^2$.

Compton (Incoherent) scattering

In Compton scattering, a photon interacts with a 'free' orbital electron and causes an ejection of a recoil (Compton) electron and scattering of the initial photon at an angle θ. The energy of the scatter photon hv' and the kinetic energy of the recoil electron E_k where ϵ is the energy of the initial photon are given as:

$$E_k = hv\frac{\epsilon(1 - cos\theta)}{1 + \epsilon(1 - cos\theta)} \tag{2.8}$$

$$hv' = hv\frac{1}{1 + \epsilon(1 - cos\theta)} \tag{2.9}$$

The probability for Compton scattering decreases with increasing energy, and is proportional to Z.

2.2.4 Absorbed dose

Absorbed dose is a metric defined as the energy imparted by directly or indirectly ionizing particles to the interacting medium. The dose is defined as the mean energy (E_{mean}) imparted by ionizing radiation to mass m in a finite volume V by:

$$D = \frac{dE_{mean}}{dm} \tag{2.10}$$

The energy imparted E_{mean} is the sum of all energy entering the volume of interest minus all the energy leaving the volume (Podgoršak et al., 2006). The unit of absorbed dose is joule per kilogram (J/kg) and is called gray (Gy).

Dose is solely a physical quantity. However, dose may indicate a rough measure on the effects of ionizing radiation. This is due to the greater number of ionization events that typically occur when the deposited dose is calculated to be greater. Thus, generally a greater dose leads to more tissue damage (*Quantitative Nuclear Medicine Imaging: Concepts, Requirements and Methods* 2014).

2.3 SPECT/CT

2.3.1 CT

Computed tomography or CT is a medical imaging modality that creates a $3D$ image through a series of X-ray projections. X-ray projections measure linear attenuation coefficients that represent the penetrability of X-rays within a medium. This penetrability is mathematically defined by the Beer-Lambert law where the incident beam $I(0)$ travels a distance x through a material with attenuation coefficient u:

$$I(x) = I(0)e^{-\int_0^x u(x),dx} \tag{2.11}$$

CT creates a $3D$ image by combining a series of X-ray projections at varying angles. Called a tomographic reconstruction, CT images are typically reconstructed with the filter-back projection. Briefly, the steps include a Fourier transformation of projection data, multiplying by a filter, then back-transforming the projection data. These steps are adequate in obtaining an image because the filter-back projection is based on the Radon transform, central-section theorem, and Fourier based filters. Fig. 2.2 summarizes this process. When looking at Fig. 2.2, it can be seen that blurring streaks are present within the back-projected images. These streaks are a natural limitation to

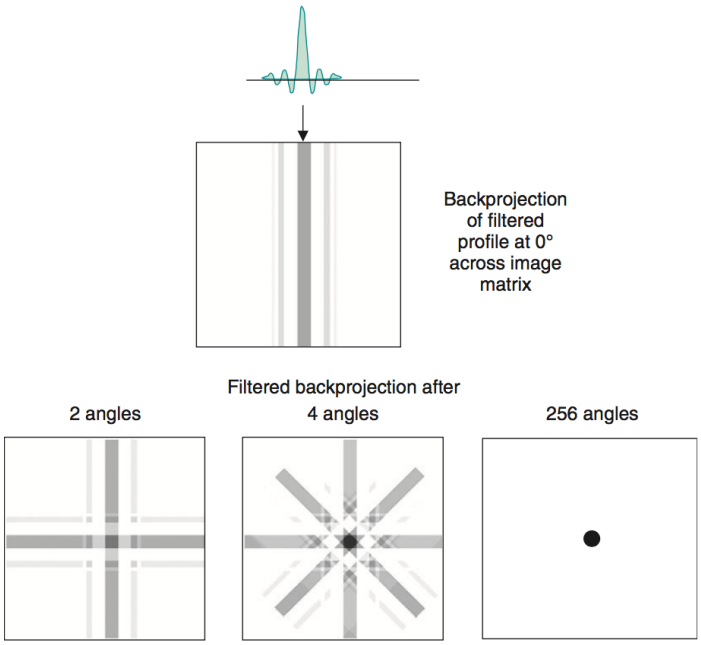

FIGURE 2.2: The filter-back projection algorithm is demonstrated here and visualizes how multiple projections back-projected will create a reconstructed image. Figure is Reproduced from (*Physics in Nuclear Medicine* 2012)

the regular back-projection algorithm and therefore a filter of $1/|r|$ is convolved to the back-projected image to mitigate the blurring (*Physics in Nuclear Medicine* 2012)

There are multiple types of CT modalities. CT modalities differ in their collection of projection data. The most common CT modalities collect their projections either through a fan-beam or helical geometry. Thus, as the name implies, these modalities are respectively called fan-beam or helical CTs. For these modalities, a filter-back projection algorithm is still utilized for reconstruction, but the resulting reconstructed units may slightly differ due to different interpolation processes.

2.3.2 SPECT

Parallel to CT, single photon emission tomography (SPECT) is an imaging modality that creates a $3D$ image through a series of gamma projections at multiple angles. Instead of utilizing an external X-ray source; however, a gamma camera collects the internal radiation source locations that have been injected within a patient before imaging. These imaging sources are typically pure gamma emitters and may be attached

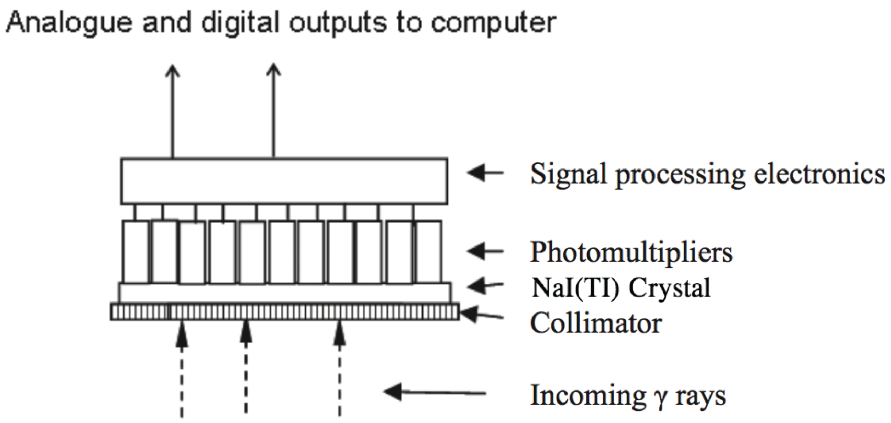

FIGURE 2.3: Illustrates the hardware components of a gamma camera. Modified from (*Nuclear Medicine Physics* 2015).

to a protein such as albumin or contained within microspheres. Unlike CT projections, SPECT projections measures counts or detects the number of gamma rays that hit a detector. In other words, SPECT, provides the activity for radioactive sources at specific spatial locations.

Gamma Camera Basics

The gamma camera is the main component of a SPECT machine. Located on a gantry, the gamma camera rotates around the patient to collect its projections. The components of a gamma camera consists of the collimator, which defines the lines of response (LOR), the radiation detector, which counts incident γ photons, the computer system, which uses data from the detector to create 2-D histograms, and the gantry (*Nuclear Medicine Physics* 2015). The components of a gamma camera are shown in Fig. 2.3.

The radiation detector within a typical gamma camera is composed of NaI(TI) phosphor crystal coupled to a couple hundred photon-multiplier tubes (PMTs). The crystal is a scintillator that converts gamma rays to scintillating near visible or visible photons. The PMTs create signals that are then proportional to the scintillating light generated in the crystal. This signal gets converted from an analog to digital signal and travels to the computer. Spatial information may be found by comparing the size of signal from

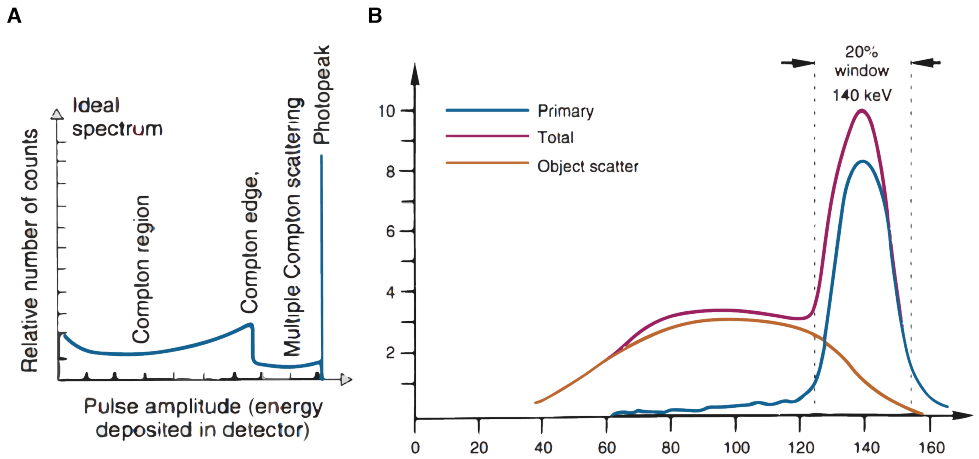

FIGURE 2.4: Visualizes a) an ideal energy spectrum and b) a more realistic energy spectrum. Modified from (*Physics in Nuclear Medicine* 2012)

different PMTs whereas the collection of all signals may be used for energy information (*Nuclear Medicine Physics* 2015; *Physics in Nuclear Medicine* 2012).

An important consideration, many gamma rays scatter and affect the accuracy and reliability of an image. When a gamma ray scatters within a patient's body, the gamma ray's original emission origin is lost. Instead, the location of the scatter will be labeled as the original radioactive source's location. The collimator's role is to combat this limitation by allowing only gamma rays that are parallel to the collimator holes or LORs to enter. However, collimators are not perfect and LORs that are not directly parallel may still be detected by the gamma camera. Moreover, gamma rays that have become parallel due to scattering will still be collected.

The issues of spatial scatter may be potentially corrected through the characteristics of a radionuclide's energy spectrum. An energy spectrum is a graphical figure that is created if all the detected gamma rays were to be collected for a specific radioactive source, which is then sorted by energy bins. In the gamma camera, not all photon deposits all their energy in the detector volume. Fig. 2.4a demonstrates the photon interactions that cause the different peaks in an ideal situation. The photopeak is defined as the energy range where a gamma ray has been deposited all of its energy in the sensitive volume of the detector. The photopeak represents the true LOR signals of the gamma camera. Therefore, an important consideration of gamma cameras, and in

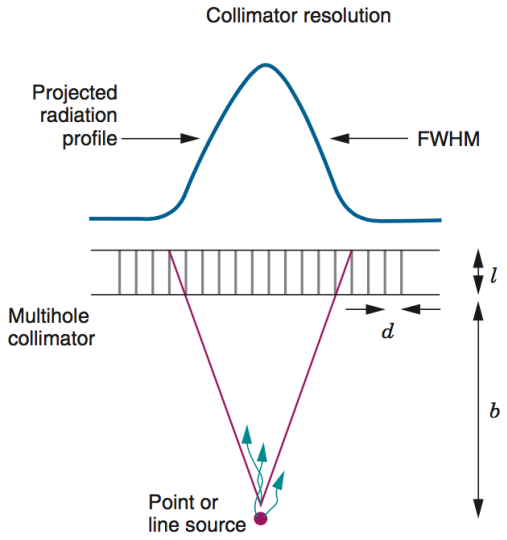

FIGURE 2.5: Demonstrates how a point source becomes blurred with the use of a Collimator. The blurring depends on the distance to the collimator (b), collimator diameter (d), and length of collimator holes (l). Reproduced from (*Physics in Nuclear Medicine* 2012)

consequence SPECT imaging is to set a proper energy detection threshold around the photopeak. When performed correctly, this permits the collection of the true LOR signals while ignoring the gamma rays that may have scattered. A typical energy window is represented as a percentage threshold around the photopeak. Fig. 2.4b illustrates an example where a 20% photopeak around 140 keV is set. In other words, all gamma rays that produce photons within 126-158 keV in the gamma crystal is assumed to be the true signal.

Spatial System Resolution

In an ideal situation where gamma rays only parallel to the collimator are collected and stored, a perfect spatial representation of the radioactive sources should exist. However, hardware limitations caused by the radiation detector, electronic hardware, and collimator lead to blurring that affects the spatial accuracies in the resulting image. The spatial blurring causes are divided into two categories: intrinsic or collimator based. The intrinsic blurring is caused by both photon scattering within the gamma cameras' crystal or the statistical uncertainties associated with the PMT electronics (*Physics in*

Nuclear Medicine 2012). On the other hand, the collimator blur is defined as the spatial spreading of the activity of a single point source. This is visualized in Fig. 2.5

Represented mathematically by a Gaussian function, the amount of blurring is defined in terms of full width at half maximum (FWHM) for both the intrinsic and collimator resolutions. The FWHM defined as half the height of a Gaussian peak and represents the minimum resolution that allows for the differentiation in spatial location of a gamma camera.

Based on the variables in Fig. 2.5, the collimator resolution is determined by:

$$FWHM_{collimator} = \frac{d}{l}(l + b) \tag{2.12}$$

The system resolution is an important metric used within gamma and SPECT imaging that measures the minimal spatial resolve of the camera. It represents the total blurring that occurs to the original activity's spatial distribution. The system resolution measured in FWHM adds the individual intrinsic and collimator resolution in quadrature as seen below:

$$FWHM_{system} = \sqrt{FWHM^2_{intrinsic} + FWHM^2_{collimator}} \tag{2.13}$$

SPECT Reconstruction

Although the CT projections and SPECT projections are in principle similar in the acquisition process, there are additional limitations for SPECT imaging. SPECT's limitations occur due to photon scattering within a patient's body, radioactivity statistics, as well as the hardware inefficiencies within the different components of the gamma camera. Therefore, the FBP is inadequate for SPECT projections reconstruction and requires a different algorithm.

Maximum Likelihood Algorithms

The Maximum Likelihood Expectation Maximum (MLEM) algorithm is the most popular algorithm used within SPECT reconstructions. Based on the maximum likelihood rationale, the MLEM algorithm estimates the parameters of a probability distribution based on observed data. Statistically speaking, the MLEM attempts to find the expectation of a specific probability distribution using only one set of observed data. This is made possible by deriving an iterative algorithm that allows an initial image estimate to be updated through a correction step. In today's terminology, this process would be considered an unsupervised machine learning technique. Within the nuclear imaging community, however, MLEM is a prevalent reconstruction technique that has been used for decades. For SPECT reconstructions, the projections of observed data are used to estimate the original activity distribution, or the expectation, within a patient by taking advantage of the fact that the collected data within its projections is detected in a Poisson nature. Typically for an unbiased image to be acquired, many acquisitions must be made to find an expected average. Fortunately, the MLEM algorithm solves this problem by reconstructing an image that will theoretically be the mathematical expected image based on one acquisition.

The MLEM algorithm starts with an equation to relay the relationship between projections and the image data. The equation below models this relationship where $\hat{y_j}^{(k)}$ represents the projection estimate at iteration k, found by converting an estimate $\lambda_j^{(k)}$ at a specific iteration step. A_{ij} is the system matrix that organizes how every pixel or voxel maps to the measurements of our projections. b_i is an additive variable that represents noise and scatter events that may present in the projection data.

$$\hat{y_j}^{(k)} = \sum_j A_{ij}\lambda_j^{(k)} + b_i \tag{2.14}$$

The MLEM is a iterative algorithm and has an iterative component where k is the iteration number and $\lambda_j^{(1)}$ starts with a positive uniform image.

$$\lambda_j^{(k+1)} = \frac{\lambda_j^{(k)}}{\sum_i A_{ij}} \sum_i A_{ij} \frac{y_i}{\hat{y_j}^{(k)}} \tag{2.15}$$

Equation 2.15 contains a correction step that allows the update of the image estimate, which has been proven that with every iteration, the updated image has a greater likelihood to be the expected image and has guaranteed convergence (i.e. will reach the expected image after enough iterations) (Shepp and Vardi, 1982; *Nuclear Medicine Physics* 2015).

The MLEM is a mathematically proven algorithm. However, due to its iterative process it is very slow, which has historically meant its clinical use has been limited. Instead, an accelerated algorithm called the ordered subset expectation maximum (OSEM) has become the standard clinical reconstruction algorithm for SPECT. This algorithm takes the same principles as the MLEM, but divides the projection data into subsets and iterates over each subset a specified number of times (Hudson and Larkin, 1994). This algorithm has been shown to accelerate the algorithm by a factor of the number of subsets utilized. However, OSEM has no guarantee of convergence and produces nosier images than the MLEM algorithm (*Nuclear Medicine Physics* 2015).

2.3.3 ^{90}Y SPECT/CT Parameters

Essentially a pure β^- emitter, ^{90}Y is an ideal therapeutic source that emits particles with enough range to completely treat the tumour while sparing the surrounding healthy tissues. This characteristic makes ^{90}Y an ideal radioactive source for treating cancers such as hepatocellular carcinoma where tumours are large and sources are deposited in the tumour peripheries (Campbell, Bailey, and Burton, 2000). However, ^{90}Y is not an ideal imaging source because it does not contain any primary gamma emissions. Instead, ^{90}Y SPECT images are acquired through bremsstrahlung photons. This introduces many issues related to its imaging. Bremsstrahlung photons create a continuous photon spectrum with energies ranging from zero to the initial β^- emission energy.

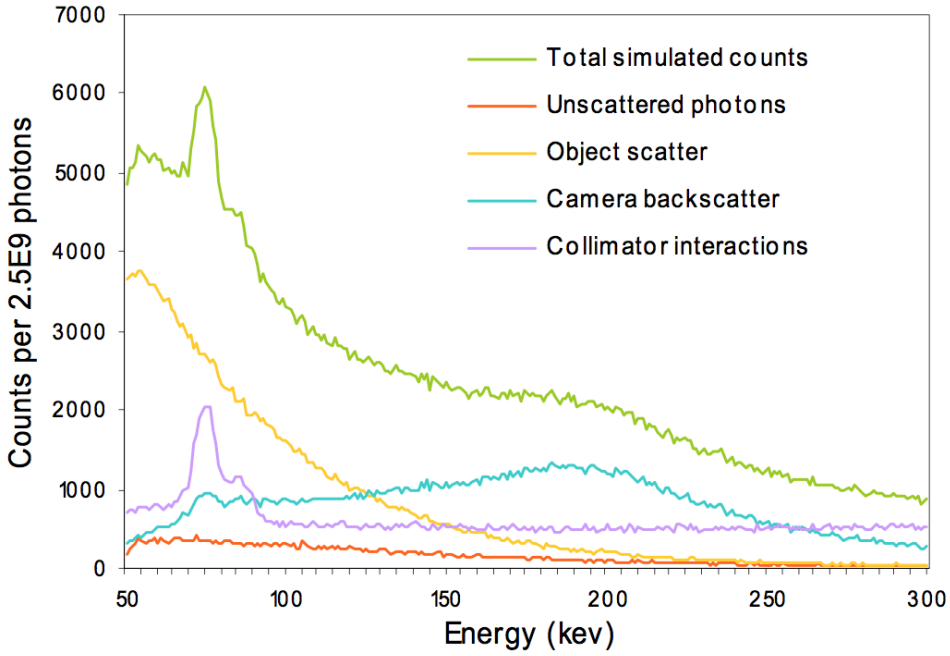

FIGURE 2.6: Simulated spectrum and its components for ^{90}Y point source in water, positioned 10 cm from camera face using MEGP collimation. Reproduced from (Heard et al., 2003)

This introduces an important question regarding the determination of the most ideal ^{90}Y photopeak.

Monte Carlo simulations have suggested that the most ideal photopeak spectrum ranges between 100-160 keV (Rong, Du, and Frey, 2012b; Heard et al., 2003). Fig. 2.6 demonstrates the components of the counts detected within a medium energy general purpose (MEGP) collimator. It can be seen that the detected ratio of primary bremsstralung to total counts is extremely low. The detected counts are dominated by those created by photon interactions. This emphasizes the need for proper reconstruction protocols, specifically correction for photon scatter, if ^{90}Y images are to be utilized quantitatively. Fortunately, newer SPECT reconstruction protocols have demonstrated that proper corrections for scatter, produce images as quantitative as PET (Siman, Mikell, and Kappadath, 2016a; Porter et al., 2018; Dewaraja et al., 2017b; Yue et al., 2016). Based on such studies, Monte Carlo scatter corrections are likely the most ideal correction method for producing quantitative SPECT images in ^{90}Y imaging.

A crucial aside, SPECT is typically filtered after reconstruction. This filtering is added because of the infiltrating noise that is intrinsic within MLEM like reconstructions when reconstructed with many iterations (*Quantitative Nuclear Medicine Imaging: Concepts, Requirements and Methods* 2014). Although adequate for qualitative images, adding a post-blurring filter adds more spatial blur, which further degrades the spatial resolution and decreases the quantitative accuracy of the reconstructed images. Post-reconstruction filtering is not recommended for quantitative images in SPECT.

Chapter 3

Literature Review

Preface

Radioembolization involves multiple clinical steps and requires interdisciplinary collaboration between professionals in interventional radiology, radiation oncology, nuclear medicine, and medical physics. This treatment mixes many clinical and technical topics into one, which makes determining relevant factors such as parameters that pertain to dosimetry difficult to realize. In this chapter, this review article synthesizes the current literature and investigates the different dosimetry methodologies. It further attempts to clarify the assumptions that are implemented within radioembolization dosimetry as well as the limitations that they may hold.

A guide to ^{90}Y radioembolization and its dosimetry

Abstract

Radioembolization gains continuous traction as a primarily palliative radiation treatment for hepatic tumours. A form of nuclear medicine therapy, Yttrium-90 containing microspheres are catheter guided and injected into the right, left, or a specifically selected hepatic artery. A multitude of comprehensive planning steps exist to ensure a thorough and successful treatment. Clear clinical and physiological guidelines have

been established and nuclear imaging is used to plan and verify dose distributions. Radioembolization's treatment rationale is based on tumour and blood vessel dynamics that allow a targeted treatment approach. However, radioembolization's dosimetry is grossly oversimplified. In fact, the currently utilized clinical dosimetric standards (e.g. partition method) have persisted since the 1990s. Moreover, the multitude of radioembolization's intertwining components lies disjointed within the literature. Particularly relevant to new readers, this review provides a methodical guide that presents the treatment rationale behind every clinical step. The emerging dosimetry methods and its factors are further discussed to provide a comprehensive review on an essential research direction.

3.1 Introduction

Radioembolization, selective internal radiation therapy (SIRT), intra-arterial radiation therapy, or trans-arterial radioembolization (TARE) are all various names for the same clinical procedure. Radioembolization is a specific type of nuclear medicine therapy used to treat primary or metastasized hepatic tumours. It is administered when other minimally invasive treatments have failed and is primarily palliative. During treatment, a catheter is used to guide and inject Yttrium-90 (^{90}Y) containing microspheres into the right, left, or a specifically selected hepatic artery. Due to unique hepatic blood flow, the microspheres are distributed preferentially to the tumour arteries, where they are permanently deposited. The tumour is then irradiated by the particles emitted by ^{90}Y.

^{90}Y is a pure beta-emitter with a half-life of 64.04 hours that disintegrates into stable zirconium-90 (^{90}Zr) by emitting beta particles with a maximum energy of 2.27 MeV and an average energy of 0.937 MeV. Within soft tissue, the released beta energy has a maximum penetration range of 11 mm with an average range of 2.5 mm. Since ^{90}Y deposits most of its energy within the first few millimeters, its therapeutic dose is concentrated

at the microspheres location (Roeske et al., 2008). Currently, there are two commercially available ^{90}Y microsphere products,the glass (Therasphere; BTG plc, UK) and resin microspheres (SIR-spheres; Sirtex Medical Limited, North Sydney, Australia). Both of these spheres are biocompatible, but not biodegradable. Theraspheres have average diameters of 20–30 μm with a standard activity that may range from 3 GBq to 20 GBq per vial. Within a vial of 3 GBq, there are around 22,000 to 72,000 microspheres per milligram, resulting to an average activity of 2500 Bq per microsphere (Kennedy et al., 2004; *Package Insert- Therapshere Yttrium-90 Glass Microspheres*). In contrast, the diameters of SIR-spheres range from 20 to 60 μm with an average activity of 50 Bq per microsphere. Normally, each resin vial has a standard activity of 3 GBq and a range of 30–50 million microspheres (Kennedy et al., 2004; *Package Insert* 2016). Highlights between the two differing microsphere products can be seen in the European Association of Nuclear medicine (EANM) guidelines (Giammarile et al., 2011). Contained within pre-packaged vials, both types of ^{90}Y microspheres are delivered, then their activity is measured right before treatment.

Radioembolization involves multiple clinical steps spanning over numerous multidisciplinary fields. There exists a plethora of articles on this treatment modality, yet there is a lack of a study that comprehensively describes the rationale behind the entire radioembolization process. Overall, this review has two objectives. The first aim is to provide a full scope of radioembolization that ties together the rationale and background behind every treatment step. Building on the discussed background, the second aim is to provide a comprehensive review by presenting the most relevant literature related to patient specific radioembolization treatments and its newly emerging dosimetry.

3.2 Methods

As a multi-disciplinary and multi-step treatment, the topics of emphasis were purposefully constrained to patient-based studies and image-based dosimetry; therefore, only

97 of around 130 original sources were listed to provide a comprehensive and succinct discussion on radioembolization. To provide the understanding and rationale behind each treatment process, background articles on liver vasculature, related nuclear imaging modalities, current clinical dosimetry methods, novel clinical studies, and review articles were included. Search words such as "patient based radioembolization", "imaged based radioembolization", "post-image dosimetry" "radioembolization", "PET/CT", "SPECT/CT", "angiography", and "primary radioembolization treatments" were inputted into specific databases. The most common databases used were Pubmed and WorldCat.

3.3 Results and Discussion

A relatively complete picture of radioembolization can be obtained by reading from the list of suggested articles within Appendix A Table 3.6. It is important to note that each of the suggested articles assumes a certain level of familiarity and only provides insight into selective segments of this treatment. In other words, none of the presented studies provide a comprehensive overview of every treatment step. Furthermore, dose response effect studies based on clinical dosimetric methods are not included in this review due to the rationale that emerging image based dosimetry methods are more dosimetrically representative. However, a previous review has amassed such results (Cremonesi et al., 2014).

3.3.1 Treatment Overview

Radioembolization requires planning that involves patient evaluation and pre-treatment imaging, the treatment itself, and finally, shortly after the treatment is completed, post-treatment verification. The multiple clinical steps are listed in Fig. 3.1. To start, patients are clinically examined for relative and absolute contraindications such as insufficient liver function or extensive and untreated portal hypertension (Giammarile et al., 2011). After a clinical evaluation, patients undergo further preliminary steps that include

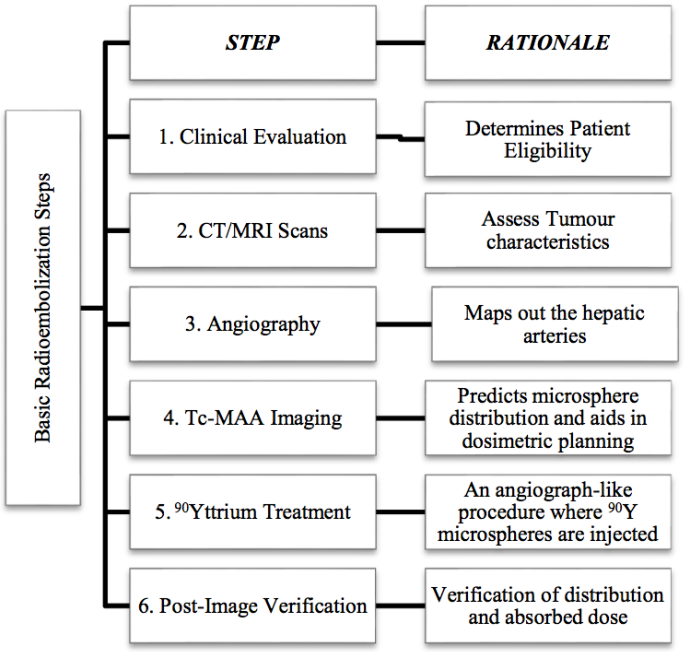

FIGURE 3.1: Clinical steps involved in the ^{90}Y radioembolization process.

imaging with a triple phase computed tomography (CT) and/or magnetic resonance imaging (MRI) to assess the liver for liver patency, extrahepatic disease, and tumoural and non-tumoural volumes (Cremonesi et al., 2014). Since radioembolization is artery based, pre-treatment workups include an angiography as well as planar scintigraphy imaging (planar imaging) and single photon emission computed tomography (SPECT) co-registered with CT (SPECT/CT) for injected ^{99m}Technetium magroaggregated albumin (Tc-MAA). Tc-MAA images are used to verify vessel mapping and to visualize any additional arteries that may lead to extrahepatic microsphere distribution. Tc-MAA distribution is also used to calculate what is called the lung shunting percentage or lung shunting fraction (LSF). The LSF estimates the total ^{90}Y microsphere deposition within the lungs and quantifies the risk of developing radiation pneumonitis, a serious side effect. Consequently, radioembolization has lung safety thresholds; if the LSF is too high, patients are deemed ineligible for treatment.

During the treatment itself, an interventional radiologist places a catheter percutaneously via a patient's femoral artery and guides it to the correct hepatic artery under X-ray fluoroscopy. Connected to the catheter, a vial containing ^{90}Y microspheres

TABLE 3.1: ECOG performance ranking description.

Grade	ECOG Performance Status
0	Fully active, able to carry on all pre-disease performance without restriction
1	Restricted in physically strenuous activity but ambulatory and able to carry out work of a light or sedentary nature, e.g., light house work, office work
2	Ambulatory and capable of all self-care but unable to carry out any work activities; up and about more than 50% of waking hours
3	Capable of only limited self-care; confined to bed or chair more than 50% of waking hours
4	Completely disabled; cannot carry on any self-care; totally confined to bed or chair
5	Dead

is infused into the body. Differences exist in the administration of the two different microsphere products. Due to their higher embolic tendency (See 3.3.8 Treatment), ^{90}Y resin microspheres are successively infused with saline and 5% dextrose whereas glass microspheres are infused by saline alone (Coldwell et al., 2011; Dezarn et al., 2011a; Ahmadzadehfar et al., 2015; Koran et al., 2016). Recently, an alternate transradial approach has been deemed feasible. This approach involves a catheter placement via a patient's radial artery and demonstrates advantages such as patient preferability and lower cost, albeit with greater technical challenges (Kis, Mills, and Hoffe, 2016). Directly after treatment, the patient has follow-up imaging with SPECT/CT or PET/CT scans to check for the microsphere distribution and to verify the dose. The review of the different treatment steps will be discussed in detail in the coming subsections.

3.3.2 Patient eligibility

Prior to radioembolization, patients must be deemed suitable for treatment. Radioembolization is used as a primarily palliative treatment, i.e. to preserve the functional capacity of the hepatic tissue (Lau et al., 2012). Eligibility stems from the existing functionality and the potential radiation tolerance of a patient's hepatic parenchyma. Such predictions are divided into three sections indicating when a patient should have treatment, when patient treatment is possible, or when a patient is ineligible for treatment. These indications are respectively labeled indications, relative contraindications, and absolute contraindications. Patient eligibility can be particular to different steps of the treatment plan. In many cases a patient may be eligible under the initial clinical evaluation, but later become ineligible during the pre-treatment imaging workup step of radioembolization (Coldwell et al., 2011).

In general, most articles refer to the Radioembolization Brachytherapy Oncology Consortium (REBOC) guidelines and manufacturing recommendations when discussing radioembolization patient selections (*Package Insert- Therapshere Yttrium-90 Glass Microspheres*; *Package Insert* 2016; Kennedy et al., 2007). The EANM has also complied patient selection guidelines for the treatment of liver cancer and metastases (Giammarile et al., 2011). The important patient indications include an unequivocal and measurable liver tumour based on CT/MRI scans, a liver-dominant tumour burden, and a life expectancy of at least 3 months (Coldwell et al., 2011; Kennedy et al., 2007).

Radiation dose to organs at risk is assessed through pre-treatment imaging with an angiography and Tc-MAA to avoid severe side effects such as radiation pneumonitis, gastrointestinal ulceration, and/or gastrointestinal bleeding due to extrahepatic microsphere deposition (Riaz, Awais, and Salem, 2014). Patients are further ineligible for treatment if they have factors such as a compromised portal vein, are pregnant, or have liver failure (Coldwell et al., 2011; Kennedy et al., 2007). The treatment eligibility has relative contraindications as well, which are based on a case-by-case basis and left to the discretion of the physician. Some factors include patients with a limited hepatic reserve, poor kidney function, or an Eastern Cooperation Oncology Group (ECOG) performance status of 2–4 (Coldwell et al., 2011; Kennedy et al., 2007; Salem and Thurston, 2006). Grading levels of the ECOG status are explained in Table 3.1. However, age and prior surgical resection are not considered to be contraindications, making radioembolization appealing for palliative therapy (Kennedy, 2014).

With restricting clinical factors well set for radioembolization, there are ideal patients who are predicted to have a good tolerance to the treatment. These patients normally show an ECOG status of less than 2, normal bilirubin levels, normal liver synthetic function (albumin greater than 3 mg/dL), a lack of ascites, and less than 50% tumour burden (Coldwell et al., 2011). It has been shown that ECOG status rather than a tumour's clinical stage is the more reliable factor in a patient's treatment tolerance (Salem and Thurston, 2006). For metastatic tumours, lower bilirubin levels were also found

TABLE 3.2: Patient Eligibility Specifications

Ideal Patient
1. ECOG < 2
2. No ascites
3. Less than 50% tumour burden
4. Albumin $>$ 3mg/dl
5. Bilirubin $<$ 2mg/dl
Indications
1. CT/MRI established tumour
2. Liver dominant tumour
3. Life Expectancy $>$ 12 weeks
Relative Contraindications
1. Excessive tumour burden without hepatic reserve
2. Compromised portal vein when super-selective catherization cannot be performed
3. Prior radiotherpay
4. ECOG 2-4
5. Creatine $>$ 2.5mg/dl
6. Abnormal bone marrow funtion
7. Bilirubin levels ($>$ 2mg/dl) with no reversible cause
*Absolute Contraindications**
Clinical Evaluations
1. Ascites and/or other symptoms of liver failure
2. Pregnant
3. Capecitabine last 2 months or planned to be administered in the future
Tc-MAA Imaging
1. $>$ 30 Gy predicted to lungs or $>$ 20% LSF**
2. Any extrahepatic deposition within the gastrointestinal tract
3. Extensively compromised portal vein
4. For repeated treatments, a 50 Gy cumulative lung dose should not be surpassed

* Steps are based on Fig. 3.1
** See 3.3.9 Current Clinical Dosimetric methods for Gy value explanations

to be reliable indicators for radioembolization tolerance (Salem and Thurston, 2006; Kennedy, 2014). Overall criteria and specificities of eligibility are presented in Table 3.2. For ^{90}Y treatment, it should be stated that the institutional and corresponding product eligibilities should always be consulted (*Package Insert- Therapshere Yttrium-90 Glass Microspheres*; *Package Insert* 2016).

3.3.3 Standard liver vasculature

As the name implies, radioembolization is built around the hepatic vasculature where the injected radioactive microspheres travel and permanently localize within the hepatic arteries. Macroscopically, hepatic vascularization is comprised of a dual blood supply where the portal vein provides 75–80% of the hepatic blood supply and the hepatic arteries provide 20–25% of the blood (Vollmar and Menger, 2009; Bierman et al., 1951). The portal vein provides partly deoxygenated but nutrient rich blood to the liver from the gastrointestinal tract while the hepatic arteries provide the oxygenated blood (Vollmar and Menger, 2009). Branches of the portal vein further divide and pass between hepatic lobules and eventually end up as sinusoids. Lobules are hexagonally functional units of the liver, otherwise known as hepatic parenchyma, and contain hepatocytes, bile of canaliculi, sinusoids, and a central vein. Hepatic tumours almost exclusively derive their blood supply from the hepatic arteries while the normal parenchyma is perfused through the portal veins. For a more thorough physiological investigation on hepatic perfusions, reviewing Van de Wiele (2012) is suggested (Wiele et al., 2012). With preferential hepatic perfusion being the basis for radioembolization, select hepatic artery catherization provides a way for the microspheres to target malignant hepatic tumours while sparing the normal tissue (Bierman et al., 1951). Therefore, a background on the most common hepatic vasculature is given.

The standard hepatic vasculature scheme starts with the celiac axis (Hoven et al., 2014). The first major branch off the aorta, the celiac artery then trifurcates into the left gastric artery (LGA), splenic artery, and the common hepatic artery (CHA). From there, the CHA continues to bi- furcate into the proper hepatic artery (PHA) and the gastroduodenal artery (GDA) and more distally the PHA divides into the right and left hepatic arteries at the hilar plate. Moreover, both hepatic arteries continually branch and decrease in size to perfuse the hepatic parenchyma and eventually make up the microvasculature of the hepatocytes, which is later discussed in 3.11 Liver Microcirculation & Distribution. Fig. 3.2 illustrates an example of a patient's hepatic vasculature.

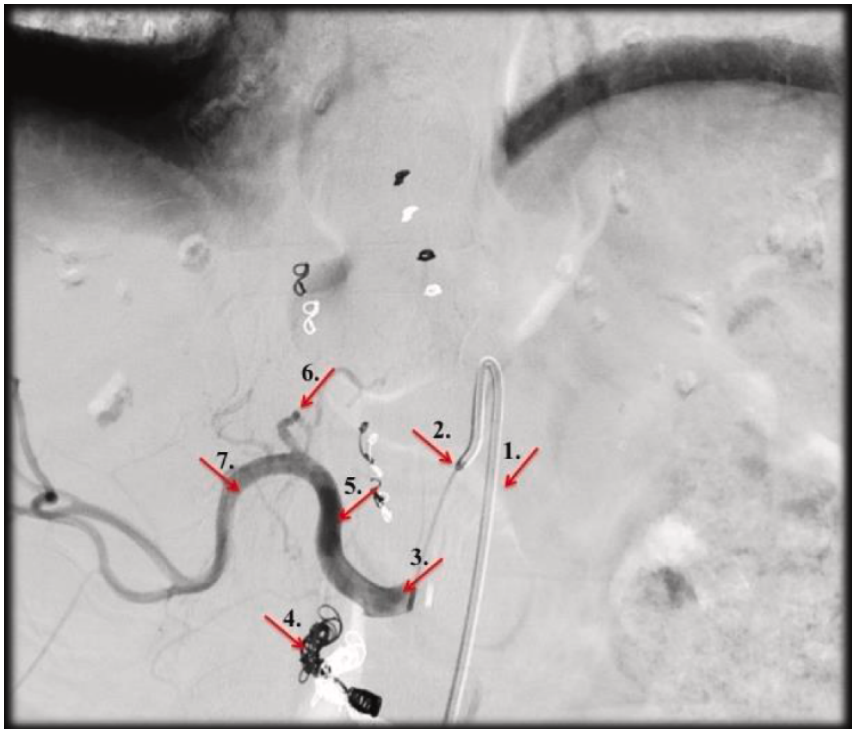

FIGURE 3.2: A digital subtraction angiography is shown for a patient being planned for right lobe radioembolization. The different parts of the hepatic vessels are labeled: 1. Catheter in the celiac trunk, 2. Microcatheter that is extended to 3. The common hepatic artery, 4. A gastroduodenal artery that is coil embolized, 5. Proper hepatic artery, 6. Left hepatic artery, 7. Right hepatic artery.

3.3.4 Angiography

In an ideal scenario, radioembolization microspheres will localize solely within the hepatic tumour's vasculature. In reality, radioembolization microspheres localize within both the healthy and tumour liver tissue. Many variations exist within the overall hepatic vasculature that may lead to additional complications. In fact, hepatic vessel variations are quite common and can be expected in 45% of patients (Michels, 1966). If such vessel variations do exist, the variable hepatic vasculature may cause extrahepatic deposition, which results in the irradiation of non- hepatic healthy tissue.

Due to such variations in vasculature, an angiography is used to map patient-specific arteries (Hoven et al., 2014; Vesselle et al., 2015). The goal of an angiographic evaluation is three fold: it is to guide the delivery catheter positioning, evaluate pre-treatment

blood flow, and to determine the variant arteries that may lead to extrahepatic microsphere deposition [8,13]. Van den Hoven et al. (2014) found that only 49% of patients had their aberrant hepatic arteries correctly identified from a standard CT scan and only 86% during angiography (Hoven et al., 2014). Thus, several modifications were recommended to the standard process including, but not limited to the use of a multiphase liver CT before an angiography, the use of C-arm cone beam CT, catheter directed CT angiography (CTA), and an evaluation of SPECT/CT co-registered images from Tc-MAA (Hoven et al., 2014; Uliel et al., 2012a). Once an angiography has been performed and possible variant vessels identified, coil embolization (also called coil occlusion or skeletonization) is recommended (Dezarn et al., 2011a; Kennedy et al., 2007; Salem and Thurston, 2006; Uliel et al., 2012a). Coil embolization involves a catheter and a metal cable that has attached collagen fibres. The metal cable is pre-formed as a spiral that is set straight. When released from a catheter, the pre-straightened coil spirals into its natural form that occludes most of the aberrant vessel. The attached collagen fibres then induce thrombosis, which blocks the rest of the vessel and prevents unwanted microsphere deposition. Coil embolization in turn directs microsphere flow to the targeted region. Depending on the variant arteries, the size of the arteries, and possible angiographic preferences, coil embolization is a calculated choice. On one hand, prophylactic embolization is seen as the safer option as the dangers of grave clinical complications such as gastrointestinal ulceration and bleeding out- weigh the dangers of coil embolization (Salem and Thurston, 2006). On the other, coil embolization is avoided in the most experienced centers due to complications and limited benefits of an embolized treatment (Braat et al., 2015). At our institution, coil embolization is administered when necessary such as when shunts to the gastrointestinal track are visible. Fig. 3.2 further demonstrates an angiogram and the relevant vessels for a patient being treated for radioembolization.

Coil embolization's effectiveness depends on the patient's coagulation speed and the effectiveness of the actual embolization. In some patients, their de-coagulation speed

may be faster than others when the induced thrombosis is cleared up and blood flow is resumed (re-canalization). In others, the initial coils may not have been packed tight enough to induce thrombosis in the first place. This problem is easily remedied through additional packing of coils. Moreover, some patients may have new vessels (collaterals) develop leading to resumed blood flow back to the targeted organ. Whatever the case, the best preparation method must be determined and evaluated for a patient undergoing radioembolization treatment.

3.3.5 Tc-MAA pre-treatment imaging

After an angiography, Tc-MAA is used to predict the potential distribution of ^{90}Y microspheres. Tc-MAA is normally provided in a vial of 10 ml solution containing $4.8x10^6$ aggregated albumin particles where 90% or more are between 10 and 90 μm in diameter. The particles may measure outside such parameters, but still have a maximum range from 0 to 150 μm (Dezarn et al., 2011a). With a short physical half-life of 6 hours and a continual bio-degradation of ^{99m}Tc from MAA, it is recommended that the Tc-MAA imaging to be done at least within 60 minutes of administration. An adult activity consists of 185 MBq Tc-MAA suspended in normal saline. If the whole liver is treated, the right and left hemilivers will be injected with 111 MBq and 74 MBq, respectively (Uliel et al., 2012a).

After injection, a gamma detection system produces a whole-body image. Planar imaging may be used to assess Tc-MAA depositions, but studies suggest a tomographic imaging modality such as a SPECT scan or a combination of SPECT and CT to provide a more accurate check of the Tc-MAA bio-distribution (Kennedy et al., 2007). It was found that planar imaging might not provide adequate detection, especially when extrahepatic sites or a non-homogenous Tc-MAA distribution is present. However, planar imaging is still clinically adopted although SPECT/CT has been proven to be more accurate for determining the distribution of Tc-MAA and the quantification of its LSF (Kao et al., 2014; Hamami et al., 2009; Allred et al., 2018a).

The Tc-MAA image is then compared to the previously assessed angiograph where the injected particle distribution is compared to the pre-planned vasculature. Ideally, the Tc-MAA microspheres are all contained within the imaged angiographic vasculature; however, the Tc-MAA microsphere distribution and the angiographically predicted distribution can differ (Uliel et al., 2012a). There are multiple causes for this discrepancy. A catheter may have been misplaced distally or past the branching point that excludes the part of the liver to be treated. New parasite vessels may have sprouted between the time the angiography was performed and the time Tc-MAA was injected. A hepatic artery may have been missed during the angiographic treatment. If any of the above scenarios are illustrated, a second angiography and a subsequent Tc-MAA injection is recommended to confirm the new vascularization (Barentsz et al., 2011). Additionally, extrahepatic activity may be seen from Tc-MAA. To combat unwanted extrahepatic activity, solutions such as additional coiling, more distal placement of the catheter, and/or super selective catherization (radiation segmentectomy) during treatment are further suggested. Coiling would physically block the ^{90}Y microspheres from passing through a specific vessel. More distal catheter placement prevents less reflux of microspheres, if any, due to the catheter physically being farther from any arterial branching. Similarly, super-selective catherization keeps microsphere localization within specifically perfused segments within the liver (for further detail see 3.3.8 Treatment).

On top of overall vessel discrepancies, the distribution within the same vasculature may have unusual Tc-MAA accumulations in both extrahepatic and intrahepatic sites (Uliel et al., 2012a). To plan a safe treatment, awareness of this heterogeneous distribution is needed to attribute a specific distribution to a cause. A variety of factors such as presence of necrotic lesions, prior trans-arterial chemoembolization (TACE) treatments, invasion of tumour within hepatic arteries, aggregation of Tc-MAA particles, or variable flow dynamics within the liver may result in heterogeneous distribution. Proficient knowledge on the causes of discrepant Tc-MAA distributions and the necessary

steps to combat them is required for an accurate radioembolization treatment plan and later, if calculated, for its dosimetry.

3.3.6 The lung shunt fraction (LSF)

Theoretically, the ^{90}Y microspheres should embolize within the tumour's hepatic terminal arteries (See 3.3.11 Liver Microcirculation & Distribution). However, arteriovenous blood vessel shunts may provide ^{90}Y microspheres a direct vascular path to the lungs, which may then cause lung irradiation (Kennedy et al., 2007). To predict this, Tc-MAA distribution is used to calculate the LSF. Estimated by the ratio of counts in the lungs to the summed counts in the lungs and liver, the LSF uses planar imaging or SPECT/CT count data for its calculations. In other words, the LSF is the fraction of Tc-MAA particles that made its way into the lungs due to arteriovenous shunts. It is worth noting that there are variations in size, density, and number between Tc-MAA particles and ^{90}Y microspheres; however, Tc-MAA particles are still used to predict the undesirable ^{90}Y microsphere deposition within the lungs. (Uliel et al., 2012a).

Depending on the imaging modality used, there exist limitations that can affect the calculation of the LSF (Lopez et al., 2019). Planar imaging has limitations that include uncorrected attenuation effects between the liver and lungs, lack of anatomical references for contouring, and a single standard lung mass value of 1 kg. These limitations combine to negatively affect the LSF calculations. In regards to SPECT/CT, a misregistration between the SPECT and CT data or truncated lungs due to a limited SPECT/CT field of view (FOV) will produce inaccurate LSF calculations.

3.3.7 Liver Segmentation Schemes

The Brisbane nomenclature is considered the standard liver seg- mentation scheme. Introduced and accepted by the International Hepato-Pancreato-Biliary Association (IHPBA), this standard was created to resolve the ambiguities presented by Couinard and

Healey [30]. According to the Brisbane nomenclature, there are three orders of division based on the liver's internal anatomy: two hemilivers, sections or sectors, and segments [30]. The first-order division divides the left and right hemiliver by a plane called the midplane of the liver, commonly known as Cantlie's line. The second-order divisions divide the liver into smaller sections or sectors and have two distinct anatomical methods of dividing the liver. The liver sections are divided based on Healey's divisions, which are dependent on hepatic arteries and bile ducts. The liver sectors are based on Couinard's divisions, which are dependent on the portal veins. Both are considered correct divisions, but sections and sectors are not synonymous to each other and are considered distinct second-order divisions. In contrast, both third-order divisions are called segments based on Couinard's eight segments. Each of Couinard's segments is functionally independent and has its own vascular flow and biliary drainage (Germain et al., 2014).

In regards to radioembolization, Couinard's divisions are primarily used. The Couinard liver segmentation includes 'lobes', 'livers', 'sectors', and 'segments' (Germain et al., 2014). In essence, the Couinard classifications are identical to Brisbane's standard, with the term 'livers' instead of 'hemilivers'. Furthermore, the surface anatomical method may be used to separate the liver into two lobes. The lobes are divided into the right and left lobes and are separated by the falciform ligament. The right lobe consists of segments 4–8 while the left lobe consists of segments 2 and 3. To note, most radioembolization literature references the differing treatment based on Couinard's "lobular" anatomy even though the Brisbane standard discourages its use (Vouche et al., 2013; Seidensticker et al., 2012; Lewandowski et al., 2016).

3.3.8 Treatment

Radioembolization treatments are dependent on the tumour's location, number of tumours, arterial perfusion, and the liver's functional capacity. If a tumour is localized within a single liver segment and supplied by one main artery or arterial branch, super

selective catherization or radiation segmentectomy is suggested. Radiation segmentectomy is when ^{90}Y based microspheres are infused within two or less hepatic segments (Riaz et al., 2011). This treatment administers high doses of radiation to the tumour and reduces the dose coverage to non-tumoural hepatic tissue. A less precise option, radiation lobectomy is an approach that treats either an entire right or left hepatic lobe. When surgical resection is not amenable or if the future liver remnant is deemed insufficient to sustain adequate hepatic function, radiation lobectomy is recommended. The effects of radiation lobectomy are two-fold; it aids in tumour control and produces contralateral lobe hypertrophy (Vouche et al., 2013; Lewandowski et al., 2016). Contralateral lobe hypertrophy is an interesting result of radioembolization where the non-irradiated hepatic lobe increases in hepatic parenchyma size. Vouche et al. (2013) have postulated that radiation induced parenchymal lesions and a decreased blood supply shrinks the irradiated lobe and induces the portal flow to redirect towards the contralateral lobe (Vouche et al., 2013). This portal flow redirection induces the contralateral lobe to increase in size and, correspondingly, increase its functionality. Additionally, radiation lobectomy provides tumour control during the regenerative phase after treatment, providing a logical step before surgical resection (Lewandowski et al., 2016).

The last radioembolization option is whole liver treatment and is required when many diffuse tumours are localized within both of the lobes. There are two methods of administering the same dose to the whole liver: sequentially through bi-lobar treatment or singularly through simultaneous treatment of both lobes. If treated sequentially, one lobe is treated first and after at least 30 days with sufficient liver regeneration the second lobe is treated (Salem and Thurston, 2006). When comparing the two, sequential radioembolization has resulted in fewer adverse side effects such as lower overall bilirubin levels and lower risks of developing radioembolization induced liver disease (REILD) (Seidensticker et al., 2012). Therefore, sequential liver treatment has become the more standard recommendation.

If feasible, more segmented therapy might be performed. If a singular artery branch is identified to perfuse the targeted tumour(s) then a more selective treatment can be used to infuse the microspheres. This serves to avoid extrahepatic deposition as well as to make treatment more spatially localized, providing higher dosages to the tumour and less intrahepatic radiation to the normal tissue. However, radioembolization is currently used as a primarily palliative treatment making more segmented treatments less likely and procedures such as sequential liver treatment the norm. Regardless, every ^{90}Y treatment should be delivered as selectively as possible to reduce irradiation of the normal liver parenchyma (Giammarile et al., 2011).

Further considerations are necessary to ensure an optimal or accurate radioembolization treatment. Lau et al. (2012) have provided ^{90}Y activity recommendations depending on the number of tumours, patient specifications, and type of treatment (Lau et al., 2012). The same authors have also recommended threshold values to prevent REILD. Other considerations include similar catheter placement during ^{90}Y microsphere treatment as during Tc-MAA injections, otherwise up to 30% of differing activity may be measured and the resulting microsphere distribution may differ (Gulec, Mesoloras, and Stabin, 2006). For SIR-spheres, a higher number of microspheres is injected to reach the same prescribed activity as each microsphere has less activity (50 Bq) compared to each Therasphere (2500 Bq) (Kennedy et al., 2004; Giammarile et al., 2011). The greater number of SIR-spheres may cause an embolic effect called flow stasis, at which point microsphere administration should stop regardless of an incomplete administration of the total prescribed activity (Dezarn et al., 2011a). Since the initial prescribed calculations are based on the volume of the target, accurate volume measurements are necessary. Hepatic volume measurements should only include the tumour volume perfused by the targeted arteries (Giammarile et al., 2011; Salem and Thurston, 2006). The treatment itself should completely administer the dose throughout the whole tumour, which is achieved by injecting microspheres into all the arteries that perfuse the different parts of the tumours.

3.3.9 Current Clinical Dosimetric Methods

When it comes to radioembolization's current clinical dosimetry, the ^{90}Y microspheres are calibrated, measured, and administered in activity (GBq). However, radiation therapy doses are normally planned in Gy (J/kg) to quantify absorbed dose from a radiation source in tissue. Likewise, radioembolization plans the prescribed doses to the patient in Gy, but converts it into prescribed activity before treatment.

The prescribed activity may not always be the activity that was administered. Differences between the prescribed and administered activity may exist due to an incomplete treatment. Aforementioned, SIR-spheres are known to have embolic tendencies that call for a halt in microsphere administration and may also have residual activity left after a complete treatment. Theraspheres may have approximately up to 5% of its residual activity left within the microsphere vial after every treatment (Giammarile et al., 2011; Coldwell et al., 2011). The calculation of the administered activity is simply the residual activity or the activity left in the microsphere vial after treatment subtracted from the prescribed activity. The theoretical range of the residual activity is between zero and the prescribed activity. More importantly, the absorbed dose should be corrected for the activity that was actually administered to the patent.

For absorbed dose calculations, radioembolization applies the MIRD formalism and directly translates activity in Bq to absorbed dose in Gy. For instance, the MIRD formula presented in Eq. 3.1 presents the simplest case where all the activity localizes within the volume of the perfused liver. Eq. 3.1 converts administered activity to absorbed dose by assuming that 1 GBq of administered activity per kg of tissue (liver) mass provides an absorbed dose of 49.38 ± 0.5 Gy, typically rounded up to 50 Gy. This is based on the assumption that ^{90}Y distributes uniformly within the tumourous tissue and healthy hepatic parenchyma to provide an evenly distributed absorbed dose.

$$D[\text{Gy}] = 50[\text{J/GBq}] \text{ x } \frac{A[\text{GBq}]}{m[\text{kg}]}$$
$$D[\text{Gy}] = \text{Dose to Specified Liver Volume} \tag{3.1}$$

In Eq. 3.1, A[GBq] represents the activity of the perfused liver while m[kg] represents the mass of the perfused liver. The derivation of this equation may be seen elsewhere (Dezarn et al., 2011a; Gulec, Mesoloras, and Stabin, 2006). A CT scan measures the liver volume that is then used to find its corresponding mass, which is achieved by multiplying the liver's density in g/cm^3 by its volume in cm^3 (Gulec, Mesoloras, and Stabin, 2006). As discussed before (See 3.3.6 Lung Shunt Fraction), the administered activity may directly shunt to the lungs. This causes extrahepatic deposition and changes the absorbed dose distributed to the liver. If there is any lung shunting, the dose to the lung or liver may be calculated if the total activity is partitioned between the liver and lung volumes as seen in Eq. 3.3. Eq. 3.2, derived from Eq. 3.1, calculates the absorbed dose to the lungs and requires the tissue mass and partitioned activity of the lungs. Accordingly, the absorbed dose to the perfused liver is calculated given the mass and partitioned activity of the perfused liver. Illustrated later, this equation is seen in Eq. 3.14 and is also called the mono-compartmental method. Importantly, both dose estimations rely on the lung volume and the LSF, which is presented in Table 3.3.

$$D_{lung}[Gy] = 50[J/GBq] \text{ x } \frac{A[GBq]}{m[kg]}$$
$$D_{lung}[Gy] = \text{Dose to Lung} \tag{3.2}$$

The corresponding activities in question may be calculated as seen in Eqs. 3.3-3.5. A_{lung} liver represents the partitioned activity within the perfused liver while A_{lung} represents the activity within the lungs.

$$A_{total}[GBq] = A_{liver} + A_{lung} \tag{3.3}$$

$$A_{liver} = A_{total} \text{ x 1-LSF} \tag{3.4}$$

TABLE 3.3: Description for calculation of LSF.

LSF Calculation	$LSF = \frac{counts_{lung}}{counts_{lung}+counts_{liver}} x100$	for lung shunt percentage
SIR-Sphere (Resin)	LSF	Activity Given
	$> 20\%$	No Activity
	$15 - 20\%$	Reduced by 40%
	$10 - 15\%$	Reduced by 20%
	$< 10\%$	Give full amount of activity
TheraSphere (Glass)	Upper Lung Shunt Activity Limit: LSF [%] × A[GBq] = 0.61 GBq A[GBq] = Activity prescribed during pre-treatment dosimetry	

These calculations are recommended based on planar scintigraphic imaging, but SPECT/CT derived data is much more reliable.

$$\left.\begin{array}{l} A_{total} = A_{total} \text{ x LSF} \\ A_{total}[GBq] = \text{Total Administered Activities} \end{array}\right] \tag{3.5}$$

Table 3.3 presents the manufacturer's recommended lung shunt thresholds. Depicted in percentages or fractions, the recommendations provide no direct information on the threshold absorbed-doses to the lungs. However, both SIR-sphere and Therasphere threshold values are based on a maximum dose of 30 Gy for a lung mass of 1.0 kg (Dezarn et al., 2011a). These values were established because patients who received an estimated singular lung dose greater than 30 Gy and/or had a cumulative dose greater than 50 Gy for repeated treatments developed radiation pneumonitis (Ho et al., 1997; Leung et al., 1995). It should be emphasized that these absorbed dose values were calculated from the LSF using planar imaging and the MIRD method of Eq. 3.2 (Leung et al., 1994). Thus, patient eligibility was set at an upper threshold of 30 Gy under these specific conditions.

As previously discussed, the LSF may further be calculated by SPECT/CT images. Recently, Allred et al. (2018) demonstrated that planar imaging overestimated the LSF by up to 44% while SPECT/CT images showed a maximum deviation of 13% (Gulec, Mesoloras, and Stabin, 2006). A poor correlation was further shown between LSFs calculated from planar and SPECT/CT imaging of Tc-MAA. Due to such poor correlations, the authors postulated that the previous thresholds of LSF, which were based on

TABLE 3.4: Prescribed Dose for Tumour Load

Resin		Reduced Load for Resin based on Lung Shunt	
		Lung Shunt Percentage	Activity of Spheres
Empiric Method	>50% Tumour Load = 3 GBq	<10%	Full prescribed activity
	25–50% Tumour Load = 2.5 GBq	10–15%	Reduce activity by 20%
	< 25% Tumour Load = 2 GBq	15–20%	Reduce activity by 40%
		> 20%	Do not give SIR-Spheres

planar imaging, should be adjusted for those calculated by SPECT/CT (Allred et al., 2018a; Ho et al., 1997; Leung et al., 1995). Currently, all of the dosimetric equations use LSF in their calculations obtained through either planar or SPECT/CT imaging, but clinically planar imaging is more readily adopted.

In clinical practice, radioembolization dosimetry is calculated from different dosimetric equations to set the treatment prescribed dose as a prescribed activity. There are currently four different clinical dosimetric methods that are dependent on the type of microsphere. Three dosimetric methods are available if resin or SIR-microspheres are used. The first dosimetric method is the empiric method that bases its recommended activity on the percent tumour involvement on the whole liver. This method relies solely on CT or MRI images to determine the liver size and tumour burden percentage, but is now abandoned due to its low safety margins regarding radiation-induced side effects (Lau et al., 2012; Kennedy et al., 2007; Smits et al., 2015). The empiric method shown in Table 3.4 prescribes an activity based on the tumour burden. When used in the past, the activity was reduced based on the LSF.

Formulated after the empiric formula, the body surface area (BSA) is the most commonly used method due to its simplicity and ease of use. This method assumes that the size of the patient's whole liver correlates with the patient's BSA (Vauthey et al., 2002). Thus, a prescribed activity could appropriately be adjusted to a patient's malignant liver volume without the need for liver volumetry on cross-sectional imaging (Smits et al., 2015). Similarly to the empiric method, the BSA could also take into account the LSF to reduce unwanted radiation within the lungs (Table 3.4). The activity prescribed is calculated as described in Eqs. 3.6 and 3.7:

$$A[GBq] = \text{(BSA-.2)} + \frac{\text{tumour volume}}{\text{tumour volume} + \text{liver volume}} \tag{3.6}$$

$$\text{BSA} = 0.20247 \text{ x height[m]}^{0.725} \text{ x weight[kg]}^{0.425} \tag{3.7}$$

In Eq. 3.6, A[GBq] stands for prescribed activity and the tumour and liver volumes may be analyzed from the patient's CT or MRI scans. With no explicit method given, the absorbed dose calculations should use the MIRD equations (Eqs. 3.1, 3.2, 3.14). It is important to note, however, that the BSA prescribed activity and the absorbed dose to the whole liver were found to be poorly correlated to one another and had a 2.5 fold difference (Lam et al., 2014; Grosser et al., 2015). It was found that larger livers were relatively underdosed while smaller livers were overdosed with the BSA method. Other limitations to the BSA equation include a disregard to the tumour-to-normal liver ratio (T/N) and establishment of an artificial limit to the injected ^{90}Y activity from 1 to 3 GBq (Kao et al., 2011). To clarify, the T/N ratio is a compartmental or tumour-specific ratio that measures the relative difference of microsphere deposition between the tumourous and non-tumourous tissue per unit mass. This ratio is estimated from the Tc-MAA image as the activity of the tumour (A_{tumour}) liver (A_{normal} liver) in counts are divided by the mass of the tumour (m_{tumour}) and normal liver (m_{normal} liver) in kg. The T/N ratio ends up unitless and is demonstrated in Eq. 3.8.

$$\textbf{T/N Ratio from Tc-MAA Image} = \frac{A_{\text{tumour}}/m_{\text{tumour}}}{A_{\text{normal liver}}/m_{\text{normal liver}}} \tag{3.8}$$

The most accurate of these three SIR-sphere dosimetric equations is called the partition method or model and is the only SIR dosimetric equation formulated directly from the MIRD methodology. In essence, the partition method partitions the previously described perfused liver into tumourous and non-tumourous (normal liver) volumes and includes the lungs, resulting in three separate compartments for dosimetry (Ho et al., 1997; Ho et al., 1996). Taking into account the T/N ratio, the LSF, and the masses of the

normal liver (m_{normal}) and tumours (m_{tumour}), the partition method is the most patient specific method of the three SIR-sphere equations (Kao et al., 2012). With CT/MRI partitioned masses, the partition method preserves the dosimetric viability that may have been lost due to any volumetric liver changes caused by previous treatments (e.g. surgery). The lung partition is normally determined through the calculation of the LSF (Table 3.3) with Tc-MAA planar imaging or SPECT/CT. LSF inclusion provides a more representative proportion of administered activity that the total perfused liver may receive. The Tc-MAA image is additionally used to calculate the T/N ratio (Eq. 3.8). This ratio allows the partition method to prescribe an activity that is limited by the maximum dose acceptable to the normal liver and is seen below:

$$\begin{aligned} A[GBq] &= \frac{D[Gy] \text{ x } (\frac{T}{N} \text{ x } m_{tumour}[kg] + m_{liver}[kg])}{50[J/GBq] \text{ x } (1 - LSF)} \\ D[Gy] &= \text{Maximum Dose for Perfused Normal Liver} \\ A[GBq] &= \text{Total Prescribed Activity} \end{aligned} \tag{3.9}$$

Depending on whether or not SIR-spheres have been administered, the absorbed dose to the different partitioned volumes may be calculated from the prescribed or administrated activity. Stemming directly from the MIRD method, the absorbed dose to the normal liver (D_{normal})and tumour (D_{tumour}), takes the MIRD formula (Eq. 3.1), and accounts for the liver partitions to produce Eqs. 3.10 and 3.11 (Dezarn et al., 2011a). A_{normal}, A_{tumour}, and A_{lung} represents the respectively partitioned activities within the normal liver, tumourous liver, and lungs. The absorbed dose to the lung is calculated in the same way as in Eq. 3.2 while the Alung is calculated as in Eq. 3.5. To find the A_{normal} and A_{tumour}, the Tc-MAA counts within the tumour and normal liver regions of interest (ROIs) are divided to find a counts ratio. Counts are assumed to be proportional to activity, hence the count ratio is equivalent to the activity ratio. Not to be confused with the T/N ratio, this activity ratio along with a calculated A_{lung} is input into Eq. 3.12 to find the resulting A_{normal} and A_{tumour} activities.

$$D[Gy] = \frac{50[J/GBq](A_{total}) \text{ x } (1 - LSF)}{(m_{normal}[kg] + \frac{T}{N} \text{ x } m_{tumour}[kg])} \tag{3.10}$$

$$D_{tumour} = T/N \text{ x } D_{normal} \tag{3.11}$$

$$\begin{aligned} A_{total} &= A_{normal} + A_{tumour} + A_{lung} \\ A_{total} &= \text{Total Administered Activity} \end{aligned} \tag{3.12}$$

While the partition method is the most accurate among the current clinical dosimetric methods, this method still has many limitations. Logistics of the partition model may require a strong working relationship between the nuclear medicine physician and the interventional radiologist; otherwise, the nuclear medicine physician may not be properly informed about the heterogeneities within the vasculature and the appropriate delineations of the ROIs (Kao et al., 2011). Furthermore, the partition method is based on the assumption that correct ROIs were drawn on the image. Depending on the institution, physician, tumour characteristics, and the resolution of the image, the ROIs may vary or be inaccurate. The ROIs considered are the partitioned volumes: tumour within the liver, normal liver, and lung. Tumours that are well defined and large such as hepatocellular carcinomas (HCC) are commonly prescribed doses with the partition method because of their clear ROIs. However, if ROIs cannot be well defined and partitioned, then the partition method cannot be accurately used. In addition, the T/N ratio lacks a standardized methodology, which leads to further variability in dosimetric reports (Mikell et al., 2016).

Compared to SIR-microspheres, the glass microspheres or Theraspheres have only one dosimetric method known as the mono- compartmental method (*Package Insert- Therapshere Yttrium-90 Glass Microspheres*; Gulec, Mesoloras, and Stabin, 2006). When calculating the prescribed activity (Eq. 3.13), the assumption that 1 GBq of administered activity per kg of tissue mass equates to 50 Gy is inherently factored in. In contrast to the partition method, the mono-compartmental method only takes into account the total perfused liver volume without partitioning the liver into more discrete and separate

units (Eqs. 3.9–3.12). This simplification makes the absorbed dose calculations less spatially precise and accurate. When activity is converted to absorbed dose, LSF is taken into account as to not overestimate the resulting absorbed dose. In other words, the prescribed absorbed dose solely considers the administered activity localized within the liver as a whole.

$$\begin{aligned} A[GBq] &= \frac{D[Gy] \text{ x } m_{liver}[kg])}{50[J/GBq] \text{ x } (1 - LSF)} \\ D[Gy] &= \text{Prescribed Dose for Perfused Normal Liver} \end{aligned} \tag{3.13}$$

Described previously, the Therasphere absorbed dose is derived from MIRD and is calculated by partitioning the liver and the lungs (Eq. 3.2–3.5). In parallel with SIR-spheres, this method takes into account either the prescribed or administered activity and is seen here:

$$\begin{aligned} D[Gy] &= \frac{50[J/GBq] \text{ x } A[GBqofAdministeredActivity] \text{ x } (1 - LSF)}{(m_{liver}[kg]} \\ D[Gy] &= \text{Administered Dose to Liver} \end{aligned} \tag{3.14}$$

It is worth noting that both SIR-spheres and Theraspheres have clinical dosimetric methods that are derived from the same MIRD formalisms (Eq. 3.1). In this regard, radioembolization treatments with SIR-sphere may apply the mono-compartmental method. More notably, Therasphere treatments may apply the SIR-sphere partition method for more accurate clinical dosimetry.

3.3.10 Shared limitations in the current clinical dosimetric methods

There are a few shared limitations within all the current clinical dosimetric methods. Mainly, the microspheres are not uniformly distributed within the treated liver. As will be subsequently discussed, the microsphere distribution is highly heterogeneous within both tumour and non-tumourous hepatic tissue. Consequently, radioembolization dosimetry is best modelled as heterogeneous clusters of point-sources that emit

beta irradiation (Kao et al., 2011). With current methods, the spatial dis- tribution of a microsphere's absorbed dose is ignored (Lau et al., 2012). Rather, an absorbed dose is attributed to an entire region. For instance, the partition method accounts for the T/N ratio, which calculates the ratio of microsphere distribution between the tumourous and non-tumourous ROIs. Assume a simple scenario where one tumour exists and the partitioned absorbed dose to that tumourous region is calculated to be 120 Gy. In this case, the tumour ROI is said to receive a uniform dose of 120 Gy, but due to a heterogeneous microsphere distribution that depends on the micro-vasculature, the real dose distribution will be variable throughout. Only specific portions of the ROI may actually receive 120 Gy. Thus, a microsphere's micro-distribution will greatly affect where the dose is deposited.

Additionally, the long beta particle range for ^{90}Y microspheres is neglected within these methods. This limitation becomes the most apparent with the partition method when the liver is divided among the tumourous and non-tumourous regions and is in close proximity to each other. Here, the ^{90}Y beta particles are arbitrarily delimited within a specific region (e.g. tumourous) and it is assumed that the entire dose is deposited within. However, the beta particles emitted from ^{90}Y may cross into and deposit their dose in the non-tumourous region. This phenomenon, when a non-targeted region obtains a dose of radiation from a neighbouring targeted region is called the "crossfire" effect. The partition method was determined as inaccurate due to the exclusion of the crossfire effect within a MIRD-5 human phantom (Kao et al., 2011). This inaccuracy was illustrated more remarkably between the tumourous and non-tumourous region when the T/N ratio and tumour involvement was high while the LSF was less than 10%. Furthermore, the dose to the liver may be underestimated within the lung boundaries due to the long range of beta particles emitted from ^{90}Y. This concept may be applied to the rest of the current clinical dosimetry methods when ^{90}Y microspheres are located at the edge of the delimited regions of the lung or liver. As a result, the beta particles emitted from ^{90}Y decay may escape and provide a lower absorbed dose than

prescribed in the specific ROI.

3.3.11 Liver microcirculation & distribution

Although the knowledge of the macroscopic hepatic vasculature is enough for radioembolization treatment, dosimetry depends on the microspheres' physical distribution within the hepatic microcirculation. Starting from the left or right hepatic arteries, hepatic microcirculation starts when these arteries divide into smaller arterioles (diameter 50–100 μm), terminal arterioles (diameters 15–50 μm), and reach the true capillary network (diameters 5–10 μm) otherwise called the sinusoids within the liver (Vollmar and Menger, 2009). With diameters of SIR-spheres or Theraspheres spanning only 20–30 or 20–60 μm, respectively, the microspheres should localize uniformly within the terminal arterioles of both the normal and tumour tissue. As was described earlier, many dose calculation formalisms base their methods after a uniform microsphere distribution within the liver. But in fact, multiple studies illustrate heterogeneous microsphere deposition. Fox et al. (1991) first described the inhomogeneity with SIR-spheres by taking two tissue samples of approximately 1 cm^3 from a representative area of normal liver tissue that had been treated (Fox et al., 1991). The authors showed that compared to the assumed uniform distribution, 86.2% of the normal tissue received less than the expected dose from a uniform distribution and up to 33.7% of the same tissue received less than one-third of this lower than expected dose. In another study, by sectioning a 10 mm piece of a resected lobe that was treated with 6x107 spheres (3.2 GBq), Campbell et al. (2000) similarly showed that normal tissue had a non-uniform distribution of microspheres (Campbell, Bailey, and Burton, 2000). Hence, the absorbed dose in normal tissues was heterogeneous rather than homogeneous. Within tumour tissue, the same authors illustrated that the microspheres deposited predominantly on the periphery of the tumour and clustered together. The microspheres were likely (90%) to cluster in groups of up to 65 microspheres with cluster sizes varying from 20 to 1500 μm in diameter. Based on Campbell's data and a basic dosimetric model, it

was found that an average of> 200 Gy was deposited within 6mm of the tumour and 2 mm into the normal tissue when measured from the tumour-normal tissue boundary (Campbell, Bailey, and Burton, 2001). Clustering of the microspheres caused an absorbed dose above average within the clusters while the absorbed dose decreased with distance from the cluster. With most of the ^{90}Y microsphere absorbed dose deposited near its source, it was shown that less than 1% of normal tissue received greater than 30 Gy. For large tumours, only the periphery would obtain a large absorbed dose.

Although these previous studies discussed SIR-spheres, it was demonstrated through four whole explanted livers that both SIR- and Theraspheres dispersed similarly within the edge of the tumour nodules (Kennedy et al., 2004). With the exception of one patient, microspheres were deposited preferentially with a ratio from 2:1 to 16:1 within the tumour periphery compared to the non-neoplastic tissue. Additionally, the authors found most of the microspheres in groups of 1 to 4, where nearly all microspheres were found lodged in the periphery of the triad units within the small and terminal arterioles (12–30 μm). Dosimetrically, the cluster had an absorbed dose cloud of 300 Gy and rapidly fell in absorbed dose to 100 Gy within 4 mm. More recently, a statistical study showed that within one patient's normal liver parenchyma the coefficient of variation (CV) of the activity concentration distribution in biopsies decreased with an increasing biopsy volume size, illustrating that the heterogeneity of microsphere deposition wasn't limited microscopically, but also relevant macroscopically to the whole liver (Hogberg et al., 2014). Through the same patient's distribution analysis of 250 sections, the same authors elaborated on the cause of whole liver non-uniformity (Hogberg et al., 2015). The authors found a linear increase in mean number of spheres per section with cluster size. Clusters of microspheres were aggregated within small arteries where small arteries were upstream of normal and terminal arterioles. As microspheres clustered within small arteries, systematic structural non- uniformity developed due to these clusters inhibiting the flow of microspheres into the smaller arterioles. Accordingly, the authors concluded that a larger number of spheres injected

would result in larger dose inhomogeneity.

With these studies, modified recommendations may arise in regards to the current methodologies of clinical practice. Repeated radioembolization treatments could become standard procedure to fully treat larger tumours. Higher threshold for administered dose based on current clinical dosimetric methods could be set. This higher threshold administration may promote a more effective treatment due to a higher absorbed dose while minimally irradiating the normal hepatic parenchyma, which receives a fraction of the dose due to non-homogenous microsphere distributions (Giammarile et al., 2011; Fox et al., 1991; Campbell, Bailey, and Burton, 2000; Hogberg et al., 2015; Lam et al., 2013; Lewandowski et al., 2014). Dosimetry implications arise as well. Radiobiological and dosimetrical effects would need to consider the effects of microsphere heterogeneous deposition. Dosimetry would further be affected by the microanatomy of a patient's liver, crossfire effects at the cellular level, microsphere bifurcation effects within hepatic arteries, and the differences in therapeutic effect when different microsphere numbers and sizes are injected within a patient. These issues are explored elsewhere (Walrand et al., 2014b; Walrand et al., 2014a; Gulec et al., 2010; Pasciak, Bourgeois, and Bradley, 2016).

3.3.12 Post-treatment imaging and its applications

Radioembolization post-imaging provides a means to document the true microsphere distribution, estimate activity in the tissue, validate predictive doses of microsphere radiation, and visualize their final bio-distribution. With the advent of quantitative SPECT (QSPECT) and PET scans, ^{90}Y has had two principle modalities of acquiring quantitative images. It is more common for patients to be imaged by SPECT than PET; however, SPECT has more limitations. ^{90}Y is a pure beta-emitter that produces mostly bremsstrahlung photons with an energy spectrum up to the maximum energy of the beta particles, i.e. 2.27 MeV. The energy spectrum of photons emerging from the patient and measured by a photon detector has no photopeak, hence, it is difficult to select a

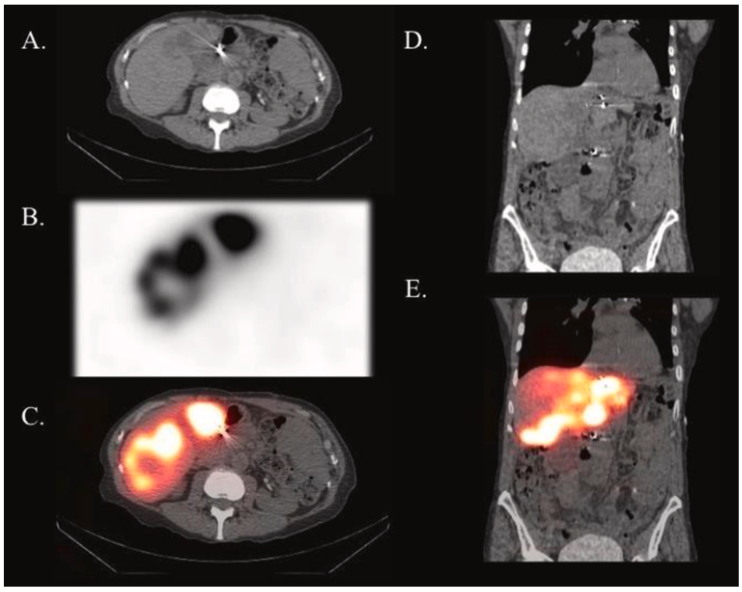

FIGURE 3.3: This figure represents a post-treatment SPECT/CT image for a radioembolization patient. Part A illustrates a standard reconstructed CT image while Part B illustrates a reconstructed SPECT intensity image. A fused image can be seen in Part C where the activity distribution of SPECT is anatomically localized in the liver CT. Part D is the same Part A image shown in a coronal slice. Furthermore, Part E is same fused image of Part C shown in the coronal slice.

proper energy window. Photons will also attenuate while interacting with the patient's tissue and may undergo the photoelectric effect, coherent scattering, and Compton scattering that cause photons to lose their original direction. In addition, the detectors used in SPECT are designed to detect photons emitted by the conventional diagnostic radionuclides, which have lower energies. The photons belonging to the highest energy region of the ^{90}Y bremsstrahlung photons may pass through the collimator septa or scatter in, lowering the image quality (Van Audenhaege et al., 2015). In fact, all raw SPECT images intrinsically contain such limitations; however, corrections can be applied during the reconstruction process. Depending on a reconstruction algorithm's corrections, SPECT images may be considered quantitative to a varying degree (Bailey and Willowson, 2014). Presently, a number of specific modeling techniques and corrections have been developed to improve the image quality of SPECT and produce good image quantification. Without these corrections, for instance for scattered photons, the resulting image would lose image contrast and present poor quantification (Bailey and

Willowson, 2014). Co-registered CT data with SPECT allows some attenuation and scatter corrections. A proper energy window optimizes the signal to noise ratio (SNR) for photons (Siman, Mikell, and Kappadath, 2016b; Rong, Du, and Frey, 2012a). More advanced algorithms can help with the image formation process that improves on attenuation, scatter and the use of a proper collimator may help with reduced photon penetration (Bailey and Willowson, 2014; Li et al., 2017; Elschot et al., 2013b; Rong et al., 2012; Dewaraja et al., 2017a). Unfortunately, QSPECT algorithms are neither readily available nor normally implemented clinically. Fig. 3.3 demonstrates an example of a post-treatment SPECT/CT image set. Hereafter, all references to SPECT/CT within this manuscript may be assumed to be quantitative (QSPECT/CT) in nature.

In contrast, PET has always been known as a quantitative imaging modality that provides higher quantification due to its superior spatial resolution and sensitivity. The decay of ^{90}Y has a minor branch to the 0+ excited state, creating a positron and electron pair every 32 in one million decays. The annihilation of this positron is used in PET imaging for radioembolization quantification (Lhommel et al., 2009). It has been shown that time-of-flight (TOF) PET and standard PET scans can both illustrate the localization and bio-distribution of ^{90}Y. TOF PET provides further ad- vantages over standard PET by providing a gain in image SNR, improved lesion detectability, and uptake measurements (Li et al., 2017; Gates et al., 2011). PET with a co-registered CT (PET/CT) additionally provides attenuation corrections (Li et al., 2017). Furthermore, image reconstruction algorithms and optimized PET/CT settings have allowed for accurate ^{90}Y-based radioembolization quantification. A multi-center study has provided a comparison between the different vendor PET/CT detectors and their quantitative results of ^{90}Y imaging (Willowson et al., 2015).

With two imaging modalities for ^{90}Y-based radioembolization, the quantitative comparisons between SPECT/CT and PET/CT have been investigated with ^{90}Y microspheres. Yue et al. (2016) compared the activity differences between SPECT with a multiple energy range (MER) reconstruction technique and non-TOF PET without

random correction based on prompt coincidences (Yue et al., 2016). The MER reconstruction technique included Monte Carlo (MC) simulations that accounted for geometric sensitivities, collimator-detector responses, and scatter kernels. The authors reported great agreement between the two imaging modalities with overall liver activities within 11% for 12 of 15 patients. At a voxel level, excellent quantitative agreement between PET and SPECT images were illustrated. However, the reconstructed voxels between SPECT and PET with low or no activities had a significant difference. More specifically, it was observed that PET overestimated the ^{90}Y in low or no activity regions. Nevertheless, the authors concluded that SPECT and non-TOF PET images were in good agreement because most general deviations could be attributed to image noise. Elschot et al. (2013) compared the latest TOF PET/CT with SPECT/ CT images and showed that with equal noise TOF PET/CT had a higher contrast recovery coefficient than SPECT/CT (Elschot et al., 2013a). The authors showed consistent data demonstrating that SPECT/CT and PET/CT were both able to visualize extra- and intra-hepatic microsphere depositions (Elschot et al., 2013a). They went further to state that PET scans were able to uniquely detect smaller accumulations of activity than SPECT. Similarly, another TOF PET and SPECT comparison was performed. Here, the authors illustrated TOF PET's superiority and concluded that PET/CT outperformed SPECT/CT in resolution, detection in non-target activity, and provided better information of ^{90}Y activity within regions of targeted tumour vascular thrombosis (Kao et al., 2013a). However, this imaging modality study was more qualitative than quantitative in nature.

Depending on the reconstruction algorithms, SPECT and PET scans may produce similar or differing reconstructed images. For example, Elschot et al. (2013) had all the PET algorithms corrected for scatter, attenuation, random coincidences, point spread function (PSF), and had TOF information while the SPECT reconstruction algorithms only

corrected for attenuation and PSF (collimator-detection) (Elschot et al., 2013a). Likewise, Kao et al. (2013) compared TOF PET/CT, which had a 3D-iterative ordered subset expectation maximum (OSEM) algorithm correcting for attenuation, scatter, random coincidence, dead time, and normalization, with SPECT/CT reconstructed with a 3D-OSEM algorithm that corrected for attenuation (Kao et al., 2013a). Therefore, these studies may have biased TOF PET performance based on image reconstruction algorithms alone. In contrast, Yue et al. (2016) corrected for photon scatter, attenuation, and collimator detection in both imaging modalities and were able to show a more comparable analysis to non-TOF PET and SPECT scans (Yue et al., 2016). Nevertheless, TOF PET scans seems to predominate in quantitative analysis by providing a more precise and accurate detection through a higher SNR and providing an intrinsic correction factor for count attenuation and intensity (Bailey and Willowson, 2014; Elschot et al., 2013a; Kao et al., 2013a).

3.3.13 Image based dosimetry and its limitations

Image based dosimetry uses SPECT/CT and PET/CT images to calculate a more accurate dose based on pre-treatment or post-treatment images. A review has summarized (3D) image based dosimetry into the general methodologies that constitutes local deposition methods, dose-kernel convolutions, and MC simulations (J, 2015). Dezarn et al. (2011) further recommend how to proceed on calculating doses at the voxel level (Dezarn et al., 2011a). While consistently investigated, image based dosimetry recommendations have yet to solidify a standardized consensus on the methodology of calculating image-based doses.

Compared to the current clinical dosimetric methods (See 3.3.9 Current Clinical Dosimetric Methods), image based dosimetry relies more directly on SPECT/CT or PET/CT images obtained from the pre-treatment or post-treatment imaging steps. Independent of tumour burden, tumour segmentation, or tumour uptake fractions, image based dosimetry estimations rely mainly on image quality such as image resolution and

reconstruction parameters (Mikell et al., 2015a). Moreover, image based dosimetry makes fewer assumptions than the current clinical dosimetric methods. In the case of direct transport MC simulations, factors such as tissue heterogeneity, crossfire effects, and non-uniform distributions can all be accounted for. Depending on the implementation, individual particles are simulated based on verified cross-sectional probabilities. Any significant particle interaction is then explored within a user-defined world and permits accurate dose calculations to the size of any given image voxel. To note, tumour and organ contouring are still necessary, but are not a requisite for voxelized dose calculations. For instance, the voxel doses based on post-treatment PET/CT voxel-based dosimetry would stay constant while the reported absorbed doses within a ROI contour may change depending on the physician's contour drawing methodology, subsequently, making image-based dosimetry a great utility for retrospective analysis.

Nevertheless, image-based methods should not be construed as without dosimetric limitations. Currently, the spatial resolution of our imaging systems cannot resolve the microsphere microscopic spatial distribution. For radioembolization, a microsphere may range from 20 to 60 μm in diameter. A CT voxel may be sub-millimeter in the x and y dimensions, but PET and to a larger regard SPECT voxels both fall closer to the multi-millimeter than sub-millimeter range. Resolution of a SPECT or PET voxel, which contains the microsphere's spatial locations, is poor when compared to a single microsphere's diameter. This will spatially limit accurate absorbed dose calculation methods such as the MC method. The problem is due to the fact that objects approximately three times less than the imaging modality's full width half max (FWHM) lead to loss of information and an underestimation of count data (Bailey and Willowson, 2014). Poor resolution may also affect image based dosimetry methods differently. Indeed, high correlations were illustrated when absorbed dose in tumours and normal liver was compared between the partition method and dose-kernel convolution method (Gallio et al., 2016). Poor resolution may have clustered the microsphere's activities and resulted in seemingly uniform absorbed dose similar to those of the

partition method. However, a MC comparison study showed much lower correlation within tumour voxels, while significant differences were observed between absorbed dose claculated with MC and current clinical dosimetric methods (Mikell et al., 2016). This result may indicate that poor imaging resolution has less of an effect on MC dosimetry due to more accurate simulatation of radiation interaction with matter. It could be argued that heterogeneous tissues may have played a role in the MC simulations; however, dose-kernel convolutions were based off S values that accounted for soft tissues similar to that of the MC simulations, which makes tissue heterogeneity a less likely dosimetric factor (Mikell et al., 2016; Lhommel et al., 2009). Most importantly, image-based dosimetry relies on the data of a reconstructed image, which is reliant on the accuracy of the image reconstruction method used. An entire field in itself, it is essential to briefly note that the accuracy and precision of an image reconstruction method becomes the core limitations to all image-based dosimetric analyses. In other words, the myriad of physics and hardware limitations that are relevant to a reconstruction process are relevant to the image-based dosimetry process as well: energy window choice, collimator choice, detector specifications, and reconstruction algorithms. A dosimetric method is only as accurate as the factors that helped reconstruct the image. Despite these limitations, however, image based dosimetry is already an improvement to the current quality of dosimetry methods. An emerging dosimetric methodology, image based dosimetry will likely improve over time.

3.3.14 Tc-MAA dosimetry

Tc-MAA injection, imaging, and results have an important diagnostic role within the radioembolization treatment. The recommendation of using Tc-MAA SPECT/CT imaging for patient based dosimetry has paved the way for investigating more accurate predictive dosimetry and the evaluation of dose to tumour responses [25,80]. Still, the efficacy of predictive dosimetry of Tc-MAA and its dose to tumour responses are debated. To start, Tc-MAA compared to ^{90}Y microspheres are inherently different in

size, radioactivity, number, and density [19]. Based on what is called the skimming effect and axial accumulation, large Tc-MAA particles could preferentially deposit in vessels of high flow while smaller particles are diverted to vessels with lower flow [19]. In other words, the larger variability in Tc-MAA's size would result in a higher heterogeneity of Tc-MAA distribution compared to those of the ^{90}Y microspheres. In addition, Wondergem et al. (2013) showed that Tc-MAA poorly predicts intrahepatic distribution of ^{90}Y SIR- spheres by studying 225 volumes of interest (VOIs) delineated from Tc- MAA SPECT/CT and ^{90}Y PET/CT images of 31 patients (Wondergem et al., 2013). Comparing SPECT/CT to PET/CT images, a difference of > 10%, 20%, and 30% were seen for 68%, 43%, and 32% of the 225 VOIs segments within a 95% confidence interval, respectively. The authors also found that compared to an optional catheter tip position, a suboptimal tip position could attribute to a higher percentage of differences between the Tc-MAA SPECT/CT images and the ^{90}Y PET/CT images. Interestingly, Kao (2013) in a letter to the editor explained that the 95% agreement was too stringent a threshold for clinical implications [81]. Kao suggested that one standard deviation or a 68% agreement would suffice. In their reply to Kao, Lam et al. (2013) agreed albeit with qualifications (Lam and Smits, 2013). First, they agreed that Tc-MAA should still be clinically utilized as long as Tc-MAA and ^{90}Y distribution differences would improve over time, but qualified that the Tc-MAA predictive distribution should be used cautiously until then. In another study, Ulrich et al. (2013) evaluated treatment response and lesion size from Tc-MAA uptake and catheter placement in 435 colorectal metastasized tumours from 66 patients (Ulrich et al., 2013). Tc-MAA uptake, catheter placement, nor their interaction effects were deemed significant to treatment response based on response evaluation criteria in solid tumours (RECIST) criteria. RECIST provides a standardized set of response on tumour shrinkage based on MRI or CT images. The criterion divides tumour shrinkage into four sections: complete and partial shrinkage, stable disease, or progressive disease (Fournier et al., 2014). However, the results from Ulrich et al. (2013) were critiqued for their poor methodology where subjective

image-based Tc-MAA uptake was used to quantify dosage without any dosimetry calculations (Ulrich et al., 2013; Kao, 2013; Lam and Smits, 2013)

Other studies have contradicted the poor predictive results of Tc-MAA. In one study, Tc-MAA predictive dosimetry was demonstrated to strongly correlate with patient responses (Garin et al., 2012). Here, a more optimistic progression- free survival (PFS) and overall survival (OS) within the European association for study of the liver (EASL) criteria was correlated for absorbed doses to tumours > 205 Gy while absorbed doses less than 205 Gy was correlated to a worse prognosis. In fact, the authors increased the prescribed activity among four patients to obtain an absorbed dose above 205 Gy that resulted in three patients responding to treatment. To note, the EASL criteria provides clinical practice guidelines and standards to diagnose, treat, and prevent liver diseases such as for HCC tumours. A more recent study had a uniform and repeatable radioembolization treatment (Gnesin et al., 2016). Using the same staff, which led to homogeneity of patient preparation, activity administration, imaging procedure, and data analysis, the authors compared both SIR-spheres and Theraspheres to Tc-MAA predictive dosimetry and illustrated that Tc-MAA and SIR-sphere dosimetry agreed overall. When comparing tumour mean doses between pre-treatment and post-treatment results Tc-MAA doses were more comparable to SIR-spheres (lin concordance, $r = 0.69$), than to Theraspheres $(r = 0.44)$. Exploring the Tc-MAA predictive compatibilities with SIR-spheres, authors found that tumours > 150 ml were more comparable $(r = 0.93 for Dmean)$. Within non-tumour liver tissue, both SIR-spheres $(r = 0.93)$ and TheraSpheres (r=0.99) had much better mean dose correlations to Tc-MAA. Thus, non-tumour liver tissue had a lower variability between predictive and post-treatment dosimetry leading to the conclusion that overdosing to normal liver parenchyma can be avoided with pre-treatment Tc-MAA injections. Similarly, Song et al. (2015) illustrated an overall and significant correlation between Tc-MAA SPECT/CT pre-treatment and ^{90}Y PET/CT treatment dosimetry (Song et al., 2015). However, the individual differences between LSF, absorbed dose to the tumour,

TABLE 3.5: ^{90}Y Post-treatment Image Based Dosimetry Studies.

Study	Imaging Modalities	Dosimetry Calculation Method	Tumour Response Criteria Microsphere Type(s)	Tumour Response by Dose (Gy)
(Strigari et al., 2010)	SPECT/CT	MC voxel dose-kernel based on water	RECIST and EASL SIR-spheres	73 Patients EASL •D_{avg} 120 Gy, D_{med} 111 for CR RECIST •D_{avg} 122 Gy, D_{med} 99 for CR
(D'Arienzo et al., 2012)* (D'Arienzo et al., 2013)*	PET/CT	MCNPX based voxel dose-kernel and CT convolution method with S Values	18-FDG PET/CT follow up at 6 months SIR-spheres	One Patient •Tumour Progression at avg. 71.6 Gy •Complete Remission at avg. 286.9 Gy
(Kao et al., 2013b)	TOF PET/CT	Voxel mean radio-concentrations	mRECIST SIR-spheres	23 Patients •D_{70} > 100 Copmlete Response •D_{70} less than 100 Partial response or no response •Smaller tumours reached D_{70} > 100 easier
(Srinivas et al., 2014)	PET/CT	MIM software and modified local deposition model	mRECIST Therapheres	98 Tumours, 56 Patient •Not significant data •Theorize > 150 Gy for SD and > 200 Gy for Response
(Chan et al., 2018)	PET/CT	Dose-Volume Kernel Method	mRECIST Therapheres	27 Patients, 38 Tumours** •D_{70} Responders = 140 Gy (28-450 Gy) vs. D_{70} Non-Responders = 24 Gy (10-133 Gy) •Responders Median = 225 Gy (51–631) vs. Non-Responders Median = 82.7 (48–199)
(Kappadath et al., 2018a)	SPECT/CT	^{90}Y SurePlan; local-deposition method	mRECIST (RECIST WHO) Therapheres	34 Patients, 53 Tumours (max 3 per patient) •WHO and RECIST showed no significance for voxel-dose and BED values*** •D_{mean} for mRECIST criteria was 263 Gy for responders and 147 Gy for non-responders •mRECIST Criteria at $D_{50\%}$ showed a mean of 160 Gy and 95% CI between 123-196 Gy •No significant correlation between D_{mean} or V_{30} Gy (Volume that receives at least 30 Gy) with toxicities

*Focuses on the dosimetry of the 2013 study, but methodology is located within the 2012 study.
**Values are of Tumour dose.
***Bed Values are not reported because they were not explained within the review.

and absorbed dose to the lungs were also deemed significant. Tc-MAA pre-treatment dosimetry led to an over-estimated LSF and an underestimated absorbed dose to the tumour and non-tumour liver tissues. Additionally, significant correlation was seen between post-treatment PET/CT dosimetry and PFS when the tumour absorbed over 200 Gy. However, for these patients the statistical analysis of the pre-treatment Tc-MAA was unavailable to make a dose to tumour comparison. Nevertheless, the authors deemed Tc-MAA a useful clinical tool for conservative dosimetric estimates for radioembolization.

3.3.15 Post-treatment image based dosimetry

After ^{90}Y treatment, post-treatment image based dosimetry may be used to retrospectively quantify the absorbed dose of an administered treatment. Studies focusing on post-treatment image based dosimetry are listed in Table 3.5. Using PET/CT, D'Arienzo

et al. (2012) conducted a voxel based dosimetry study based on convolved S values, MC simulations, and a MATLAB software (D'Arienzo et al., 2012). After verifying the software with phantom measurements, a subsequent and retrospective study was performed on one patient with metastatic colorectal cancer treated with ^{90}Y-based radioembolization (D'Arienzo et al., 2013). The authors divided the tumour ROIs into two tumourous regions, tumours with a necrotic core and those without. Calculating the dose volume histograms in both regions, the authors found that necrotic core tumours received an average dose of 71.6 Gy that was correlated with progressive disease. Within the other treated tumourous area, a complete response was documented with an average of 286.9 Gy estimated over the whole region. Within 23 patients, Kao et al. (2013) utilized a simplified dosimetric approach by calculating voxel mean and self-defined radioconcentrations rather than implementing an image-based methodology on post-treatment radioembolization PET/CT images (Kao et al., 2013b). Only 8 patients were further studied due to strict tumour criteria and of those chosen, their tumour responses were reported using the mRECIST criteria. These patients had varying tumours that included HCC, cholangiocarcinoma, and adrenal metastatic gastrointestinal stromal tumours. To clarify, the mRECIST criterion is a modified RECIST criterion that is specific to HCC tumours and only takes into account the viable portions of lesions to assess treatment efficacies (Fournier et al., 2014). Defining D_{70} as the minimum dose received by 70% of the tumour and V_{100} defined as the percent of the target volume receiving 100% of the prescribed dose, the authors found that tumours receiving D_{70} over 100 Gy had a complete response while tumour receiving D_{70} under 100 Gy had an incomplete response. In another study, a modified local deposition model was applied to a cohort of 56 HCC patients representing 98 tumours (Srinivas et al., 2014). A delivered dose ranging between 0 and 570 Gy with a mean absorbed dose of 169 Gy was observed. The authors came to the conclusion that the prescribed dose should be > 100 Gy and observed that the majority of tumours receiving such an absorbed dose were less than 100 ml in volume. The authors then assessed 48 acceptable tumours

and compared them through the mRECIST criteria. There was no statistical significance between absorbed dose and tumour response and therefore only a suggestive trend of tumour response to high-absorbed dose could be concluded. However, the authors noted that the absorbed doses in normal liver gave a significant correlation between the absorbed dose and two or more severe liver complications. The authors concluded that with every 10 Gy increase in the normal liver parenchyma, an estimated 61% increase in the odds of liver complications would ensue. Strigari et al. (2010) further calculated the absorbed dose through SPET/CT with dose- kernel calculations based on MC simulations in water (Strigari et al., 2010). Reporting a mean dose of 110 Gy to the target volume for 73 patients with HCC, the authors illustrated a complete or partial response for 74% of the tumours using the EASL criteria and a complete or partial response for 55% of the tumours using the RECIST criteria. With normal liver tissue, a median of 36 Gy was seen to cause grade 2 to 4 toxicities in a portion of the treated patients. Other authors have analyzed 27 patients and performed a per lesion analysis on 38 HCC tumours (Chan et al., 2018). Characterizing patient responses based on the mRECIST criteria, two patient groups were analyzed including a responder (Complete and Partial Response) and non-responder group (Stable Disease and Progressive Disease). The authors demonstrated that the non-responders had an absorbed dose median of 83 Gy while the responders had an absorbed dose median of 225 Gy and further reported that an absorbed tumour dose threshold of 200 Gy could predict a HCC response with 66% sensitivity. In another dosimetric study, the ^{90}Y SurePlan commercial software by MIM (Kappadath et al., 2018a) was used to perform post-treatment dosimetry on 34 patients with HCC. A total of 53 tumours were analysed with no more greater than three tumours taken from each patient. Utilizing the mRECIST criteria in this study, the logistical regression analysis demonstrated that the D_{50}% (D_x as defined by the authors is the absorbed dose that would demonstrate a x% probability in a tumour-response) was 160 Gy. The authors additionally remarked that the D_{mean}, and D_{20} to D_{80} values were able to predict an mRECIST response with significant correlation. For the normal liver, the authors found no significant correlations

between the normal liver D_{mean} to the toxicities associated with bilirubin, albumin or ascites.

3.4 Conclusion

Radioembolization is a multi-faceted and multi-disciplinary treatment. With many clinical steps, the treatment process itself is highly personalized and theoretically compelling. However, the full effectiveness of the clinical plan has not yet been realized. One of the main drawbacks with this treatment is the basic and simplified dosimetry that is clinically practiced. The literature is further riddled with varying methods for dosimetric advances. Due to a myriad of inhomogeneous methodologies and dosimetric methods, patient responses based on quantified doses becomes challenging to interpret and compare. Therefore, proper standardized dosimetry becomes a necessary first step towards a sense of congruence and comparability. Primarily palliative, more first-line treatments must be conducted to truly test its effectiveness. Artery specific, thus tumour specific, effectiveness of a personalized treatment cannot be evaluated if the therapeutic goal is diffuse tumour ablations rather than tumour-targeted and curative plans. Fortunately, the continuing advancements of imaging modalities and the increasing power of computer technology permits faster and more accurate absorbed dose calculations. Higher resolution images and image based dosimetry methods (e.g. MC method) that take into account the patient's anatomy, tissue heterogeneities, proper detector calibrations, and accurate reconstruction techniques will eventually provide a complete and accurate dosimetry toolkit.

3.5 Disclosure

The authors have nothing to disclose

TABLE 3.6: Appendix A: Recommended Radioembolization Studies.

Study*	Nature of Topic	Highlighted Content
(Salem and Thurston, 2006)	Technical: Not Necessarily Review, but a Comprehensive Study	Covers Entire Procedure in Technical Detail •Has insight at every section
(Kennedy et al., 2007)	Recommendations by REBOC	Covers Entire Procedure •Read Recommendations in Table 1
(Dezarn et al., 2011a)	Recommendations and Overview of RE	Covers Entire Procedure in Technical Detail •Dosimetry Equations •^{90}Y Calibrations •Radiation Safety for patients, staff, and rooms
(Giammarile et al., 2011)	EANM Guidelines for ^{90}Yttrium Treatment	Covers Entire Treatment Procedure •Patient Indications •Administration •Dosimetry Equations •Comparisons between SIR- and Thera-Spheres
(Cremonesi et al., 2014)	Review of Radiobiological and Dosimetric Methods	Covers Most Treatment Aspects of Radioembolization •Overall microscopic distribution •Radiobiological Modeling (EBRT vs. RE) •Radioembolization Side Effects (RILD vs. REILD, Thera vs. SIR-spheres, lungs) •Dose-response reports organized between Thera or SIR microsphere treatments
(Lau et al., 2012)	Recommendations on Safety and Activity Thresholds	Covers Entire Procedure •Treatment Planning Guide •Patient Activity Thresholds
(J, 2015)	Review of 3D Dosimetric Methods and Limitations for RE	Review Paper focusing on Dosimetry related Technicalities •Limitations on Dosimetry equations •Image Based Dosimetry Methods (Monte Carlo, Dose Kernel) Convolution, and Local Deposition •Emerging Directions (PET scans, PET isotopes, other treatment isotopes)
(Braat et al., 2015)	Review of Radioembolization in General	Covers every treatment aspect of radioembolization •Clinical indications, relative, and absolute contraindications •Tumour Response based primarily on clinical studies

3.6 Acknowledgments

This work was supported by the Collaborative Health Research Project (CHRP grant number 523394-18). The authors would like to thank Dr. Tatiana Cabrera at McGill University Health Center for her aid, which have allowed the firsthand participation in radioembolization planning steps and treatments.

References

Ahmadzadehfar, Hojjat et al. (Oct. 2015). "Evaluation of the delivered activity of yttrium-90 resin microspheres using sterile water and 5 % glucose during administration". In: *EJNMMI Research* 5.1.

Allred, J. D. et al. (2018a). "The value of (99m)Tc-MAA SPECT/CT for lung shunt estimation in (90)Y radioembolization: a phantom and patient study". In: *EJNMMI Res* 8.1, p. 50. ISSN: 2191-219X (Print). DOI: 10.1186/s13550-018-0402-8.

Bailey, D. L. and K. P. Willowson (2014). "Quantitative SPECT/CT: SPECT joins PET as a quantitative imaging modality". In: *Eur J Nucl Med Mol Imaging* 41 Suppl 1, S17–25. ISSN: 1619-7089 (Electronic), 1619-7070 (Linking).

Barentsz, M. W. et al. (2011). "Technical solutions to ensure safe yttrium-90 radioembolization in patients with initial extrahepatic deposition of (99m)technetium-albumin macroaggregates". In: *Cardiovasc Intervent Radiol* 34.5, pp. 1074–9. DOI: 10.1007/s00270-010-0088-4.

Bierman, H. R. et al. (1951). "Studies on the blood supply of tumors in man. III. Vascular patterns of the liver by hepatic arteriography in vivo". In: *J Natl Cancer Inst* 12.1, pp. 107–31. ISSN: 0027-8874 (Print), 0027-8874 (Linking).

Braat, A. J. et al. (2015). "(9)(0)Y Hepatic Radioembolization: An Update on Current Practice and Recent Developments". In: *J Nucl Med* 56.7, pp. 1079–87. ISSN: 1535-5667 (Electronic), 0161-5505 (Linking). DOI: 10.2967/jnumed.115.157446.

Campbell, A. M., I. H. Bailey, and M. A. Burton (2000). "Analysis of the distribution of intra-arterial microspheres in human liver following hepatic yttrium-90 microsphere therapy". In: *Phys Med Biol* 45.4, pp. 1023–33. ISSN: 0031-9155 (Print), 0031-9155 (Linking).

Campbell, A. M., I. H. Bailey, and M. A. Burton (2001). "Tumour dosimetry in human liver following hepatic yttrium-90 microsphere therapy". In: *Phys Med Biol* 46.2, pp. 487–98. ISSN: 0031-9155 (Print), 0031-9155 (Linking).

Chan, Keith T. et al. (June 2018). "Prospective Trial Using Internal Pair-Production Positron Emission Tomography to Establish the Yttrium-90 Radioembolization Dose Required for Response of Hepatocellular Carcinoma". In: *International Journal of Radiation Oncology∗Biology∗Physics* 101.2, pp. 358–365.

Coldwell, Douglas et al. (June 2011). "General Selection Criteria of Patients for Radioembolization of Liver Tumors". In: *American Journal of Clinical Oncology* 34.3, pp. 337–341.

Cremonesi, Marta et al. (Aug. 2014). "Radioembolization of Hepatic Lesions from a Radiobiology and Dosimetric Perspective". In: *Frontiers in Oncology* 4.

D'Arienzo, M. et al. (2012). "90Y PET-based dosimetry after selective internal radiotherapy treatments". In: *Nucl Med Commun* 33.6, pp. 633–40. ISSN: 1473-5628 (Electronic), 0143-3636 (Linking).

D'Arienzo, M. et al. (2013). "Absorbed dose to lesion and clinical outcome after liver radioembolization with 90Y microspheres: a case report of PET-based dosimetry". In: *Ann Nucl Med* 27.7, pp. 676–80. ISSN: 1864-6433 (Electronic), 0914-7187 (Linking).

Dewaraja, Y. K. et al. (2017a). "Improved quantitative (90) Y bremsstrahlung SPECT/CT reconstruction with Monte Carlo scatter modeling". In: *Med Phys* 44.12, pp. 6364–6376. ISSN: 2473-4209 (Electronic), 0094-2405 (Linking).

Dezarn, William A. et al. (Aug. 2011a). "Recommendations of the American Association of Physicists in Medicine on dosimetry, imaging, and quality assurance procedures for 90 Y microsphere brachytherapy in the treatment of hepatic malignancies". In: *Medical Physics* 38.8, pp. 4824–4845.

Elschot, M. et al. (2013a). "Quantitative comparison of PET and Bremsstrahlung SPECT for imaging the in vivo yttrium-90 microsphere distribution after liver radioembolization". In: *PLoS One* 8.2, e55742. ISSN: 1932-6203 (Electronic), 1932-6203 (Linking).

Elschot, M. et al. (2013b). "Quantitative Monte Carlo-based 90Y SPECT reconstruction". In: *J Nucl Med* 54.9, pp. 1557–63. ISSN: 1535-5667 (Electronic), 0161-5505 (Linking).

Fournier, L. et al. (2014). "Imaging criteria for assessing tumour response: RECIST, mRECIST, Cheson". In: *Diagn Interv Imaging* 95.7-8, pp. 689–703. ISSN: 2211-5684 (Electronic), 2211-5684 (Linking).

Fox, R. A. et al. (1991). "Dose distribution following selective internal radiation therapy". In: *Int J Radiat Oncol Biol Phys* 21.2, pp. 463–7. ISSN: 0360-3016 (Print), 0360-3016 (Linking).

Gallio, E. et al. (2016). "Calculation of tumour and normal tissue biological effective dose in (90)Y liver radioembolization with different dosimetric methods". In: *Phys Med* 32.12, pp. 1738–1744. ISSN: 1724-191X (Electronic), 1120-1797 (Linking).

Garin, E. et al. (2012). "Dosimetry based on 99mTc-macroaggregated albumin SPECT/CT accurately predicts tumor response and survival in hepatocellular carcinoma patients treated with 90Y-loaded glass microspheres: preliminary results". In: *J Nucl Med* 53.2, pp. 255–63. ISSN: 1535-5667 (Electronic), 0161-5505 (Linking).

Gates, V. L. et al. (2011). "Internal pair production of 90Y permits hepatic localization of microspheres using routine PET: proof of concept". In: *J Nucl Med* 52.1, pp. 72–6. ISSN: 1535-5667 (Electronic), 0161-5505 (Linking).

Germain, T. et al. (2014). "Liver segmentation: practical tips". In: *Diagn Interv Imaging* 95.11, pp. 1003–16. DOI: 10.1016/j.diii.2013.11.004.

Giammarile, Francesco et al. (Apr. 2011). "EANM procedure guideline for the treatment of liver cancer and liver metastases with intra-arterial radioactive compounds". In: *European Journal of Nuclear Medicine and Molecular Imaging* 38.7, pp. 1393–1406.

Gnesin, S. et al. (2016). "Partition Model-Based 99mTc-MAA SPECT/CT Predictive Dosimetry Compared with 90Y TOF PET/CT Posttreatment Dosimetry in Radioembolization of Hepatocellular Carcinoma: A Quantitative Agreement Comparison". In: *J Nucl Med* 57.11, pp. 1672–1678. ISSN: 1535-5667 (Electronic), 0161-5505 (Linking).

Grosser, O. S. et al. (2015). "Intrahepatic Activity Distribution in Radioembolization with Yttrium-90-Labeled Resin Microspheres Using the Body Surface Area Method–A Less than Perfect Model". In: *J Vasc Interv Radiol* 26.11, pp. 1615–21. ISSN: 1535-7732 (Electronic), 1051-0443 (Linking). DOI: 10.1016/j.jvir.2015.07.021.

Gulec, S. A., G. Mesoloras, and M. Stabin (2006). "Dosimetric techniques in 90Y-microsphere therapy of liver cancer: The MIRD equations for dose calculations". In: *J Nucl Med* 47.7, pp. 1209–11.

Gulec, S. A. et al. (2010). "Hepatic structural dosimetry in (90)Y microsphere treatment: a Monte Carlo modeling approach based on lobular microanatomy". In: *J Nucl Med* 51.2, pp. 301–10. ISSN: 1535-5667 (Electronic), 0161-5505 (Linking).

Hamami, M. E. et al. (2009). "SPECT/CT with 99mTc-MAA in radioembolization with 90Y microspheres in patients with hepatocellular cancer". In: *J Nucl Med* 50.5, pp. 688–92. DOI: 10.2967/jnumed.108.058347.

Ho, S. et al. (1996). "Partition model for estimating radiation doses from yttrium-90 microspheres in treating hepatic tumours". In: *Eur J Nucl Med* 23.8, pp. 947–52. ISSN: 0340-6997 (Print), 0340-6997 (Linking).

Ho, S. et al. (1997). "Clinical evaluation of the partition model for estimating radiation doses from yttrium-90 microspheres in the treatment of hepatic cancer". In: *Eur J Nucl Med* 24.3, pp. 293–8.

Hogberg, J. et al. (2014). "Heterogeneity of microsphere distribution in resected liver and tumour tissue following selective intrahepatic radiotherapy". In: *EJNMMI Res* 4.1, p. 48. ISSN: 2191-219X (Print).

– (2015). "Increased absorbed liver dose in Selective Internal Radiation Therapy (SIRT) correlates with increased sphere-cluster frequency and absorbed dose inhomogeneity". In: *EJNMMI Phys* 2.1, p. 10. ISSN: 2197-7364 (Print), 2197-7364 (Linking).

Hoven, Andor F. van den et al. (Jan. 2014). "Identifying Aberrant Hepatic Arteries Prior to Intra-arterial Radioembolization". In: *CardioVascular and Interventional Radiology* 37.6, pp. 1482–1493.

J, O' Doherty (2015). "A review of 3D image-based dosimetry, technical considerations and emerging perspectives in (90)Y microsphere therapy". In: *J Diagn Imaging Ther* 2.2, pp. 1–34. ISSN: 2057-3782 (Print), 2057-3782 (Linking).

Kao, Y. H. (2013). "Results confounded by a disregard for basic dose-response radiobiology". In: *J Nucl Med* 54.9, pp. 1682–3. ISSN: 1535-5667 (Electronic), 0161-5505 (Linking).

Kao, Y. H. et al. (2011). "Clinical implications of the body surface area method versus partition model dosimetry for yttrium-90 radioembolization using resin microspheres: a technical review". In: *Ann Nucl Med* 25.7, pp. 455–61. ISSN: 1864-6433 (Electronic), 0914-7187 (Linking). DOI: 10.1007/s12149-011-0499-6.

Kao, Y. H. et al. (2012). "Image-guided personalized predictive dosimetry by artery-specific SPECT/CT partition modeling for safe and effective 90Y radioembolization". In: *J Nucl Med* 53.4, pp. 559–66. ISSN: 1535-5667 (Electronic), 0161-5505 (Linking). DOI: 10.2967/jnumed.111.097469.

Kao, Y. H. et al. (2013a). "Post-radioembolization yttrium-90 PET/CT - part 1: diagnostic reporting". In: *EJNMMI Res* 3.1, p. 56. ISSN: 2191-219X (Print).

Kao, Y. H. et al. (2013b). "Post-radioembolization yttrium-90 PET/CT - part 2: dose-response and tumor predictive dosimetry for resin microspheres". In: *EJNMMI Res* 3.1, p. 57. ISSN: 2191-219X (Print).

Kao, Yung Hsiang et al. (June 2014). "Personalized predictive lung dosimetry by technetium-99m macroaggregated albumin SPECT/CT for yttrium-90 radioembolization". In: *EJNMMI Research* 4.1.

Kappadath, S. Cheenu et al. (Oct. 2018a). "Hepatocellular Carcinoma Tumor Dose Response After 90Y-radioembolization With Glass Microspheres Using 90Y-SPECT/CT-Based Voxel Dosimetry". In: *International Journal of Radiation Oncology∗Biology∗Physics* 102.2, pp. 451–461.

Kennedy, A. (2014). "Radioembolization of hepatic tumors". In: *J Gastrointest Oncol* 5.3, pp. 178–89. ISSN: 2078-6891 (Print), 2078-6891 (Linking).

Kennedy, Andrew et al. (May 2007). "Recommendations for Radioembolization of Hepatic Malignancies Using Yttrium-90 Microsphere Brachytherapy: A Consensus Panel Report from the Radioembolization Brachytherapy Oncology Consortium". In: *International Journal of Radiation Oncology∗Biology∗Physics* 68.1, pp. 13–23.

Kennedy, Andrew S. et al. (Dec. 2004). "Pathologic response and microdosimetry of 90Y microspheres in man: Review of four explanted whole livers". In: *International Journal of Radiation Oncology∗Biology∗Physics* 60.5, pp. 1552–1563.

Kis, Bela, Matthew Mills, and Sarah E. Hoffe (Sept. 2016). "Hepatic radioembolization from transradial access: initial experience and comparison to transfemoral access". In: *Diagnostic and Interventional Radiology* 22.5, pp. 444–449.

Koran, Mary Ellen et al. (Nov. 2016). "Five percent dextrose maximizes dose delivery of Yttrium-90 resin microspheres and reduces rates of premature stasis compared to sterile water". In: *Biomedical Reports* 5.6, pp. 745–748.

Lam, M. G. and M. L. Smits (2013). "Value of 99mTc-macroaggregated albumin SPECT for radioembolization treatment planning". In: *J Nucl Med* 54.9, pp. 1681–2. ISSN: 1535-5667 (Electronic), 0161-5505 (Linking).

Lam, M. G. et al. (2013). "Safety of repeated yttrium-90 radioembolization". In: *Cardiovasc Intervent Radiol* 36.5, pp. 1320–8. ISSN: 1432-086X (Electronic), 0174-1551 (Linking).

Lam, M. G. et al. (2014). "Limitations of body surface area-based activity calculation for radioembolization of hepatic metastases in colorectal cancer". In: *J Vasc Interv Radiol* 25.7, pp. 1085–93. ISSN: 1535-7732 (Electronic), 1051-0443 (Linking). DOI: 10.1016/j.jvir.2013.11.018.

Lau, Wan-Yee et al. (Jan. 2012). "Patient Selection and Activity Planning Guide for Selective Internal Radiotherapy With Yttrium-90 Resin Microspheres". In: *International Journal of Radiation Oncology∗Biology∗Physics* 82.1, pp. 401–407.

Leung, T. W. et al. (1995). "Radiation pneumonitis after selective internal radiation treatment with intraarterial 90yttrium-microspheres for inoperable hepatic tumors".

In: *Int J Radiat Oncol Biol Phys* 33.4, pp. 919–24. ISSN: 0360-3016 (Print), 0360-3016 (Linking). DOI: 10.1016/0360-3016(95)00039-3.

Leung, W. T. et al. (1994). "Measuring lung shunting in hepatocellular carcinoma with intrahepatic-arterial technetium-99m macroaggregated albumin". In: *J Nucl Med* 35.1, pp. 70–3.

Lewandowski, R. J. et al. (2014). "Sustained safety and efficacy of extended-shelf-life (90)Y glass microspheres: long-term follow-up in a 134-patient cohort". In: *Eur J Nucl Med Mol Imaging* 41.3, pp. 486–93. ISSN: 1619-7089 (Electronic), 1619-7070 (Linking).

Lewandowski, R. J. et al. (2016). "(90) Y radiation lobectomy: Outcomes following surgical resection in patients with hepatic tumors and small future liver remnant volumes". In: *J Surg Oncol* 114.1, pp. 99–105. DOI: 10.1002/jso.24269.

Lhommel, R. et al. (2009). "Yttrium-90 TOF PET scan demonstrates high-resolution biodistribution after liver SIRT". In: *Eur J Nucl Med Mol Imaging* 36.10, p. 1696. ISSN: 1619-7089 (Electronic), 1619-7070 (Linking).

Li, T. et al. (2017). "Quantitative Imaging for Targeted Radionuclide Therapy Dosimetry - Technical Review". In: *Theranostics* 7.18, pp. 4551–4565. ISSN: 1838-7640 (Electronic), 1838-7640 (Linking).

Lopez, B. et al. (2019). "Calculation of lung mean dose and quantification of error for (90) Y-microsphere radioembolization using (99m) Tc-MAA SPECT/CT and diagnostic chest CT". In: *Med Phys* 46.9, pp. 3929–3940. DOI: 10.1002/mp.13575.

Michels, Nicholas A. (Sept. 1966). "Newer anatomy of the liver and its variant blood supply and collateral circulation". In: *The American Journal of Surgery* 112.3, pp. 337–347.

Mikell, J. K. et al. (2015a). "Comparing voxel-based absorbed dosimetry methods in tumors, liver, lung, and at the liver-lung interface for (90)Y microsphere selective internal radiation therapy". In: *EJNMMI Phys* 2.1, p. 16. ISSN: 2197-7364 (Print), 2197-7364 (Linking).

Mikell, J. K. et al. (2016). "Selective Internal Radiation Therapy With Yttrium-90 Glass Microspheres: Biases and Uncertainties in Absorbed Dose Calculations Between Clinical Dosimetry Models". In: *Int J Radiat Oncol Biol Phys* 96.4, pp. 888–896. ISSN: 1879-355X (Electronic), 0360-3016 (Linking). DOI: 10.1016/j.ijrobp.2016.07.021.

Package Insert (2016). Report. Sirtex Medical Limited.

Package Insert- Therapshere Yttrium-90 Glass Microspheres. Report. Biocompatibles UK Ltd, a BTG International group company.

Pasciak, A. S., A. C. Bourgeois, and Y. C. Bradley (2016). "A Microdosimetric Analysis of Absorbed Dose to Tumor as a Function of Number of Microspheres per Unit Volume in 90Y Radioembolization". In: *J Nucl Med* 57.7, pp. 1020–6. ISSN: 1535-5667 (Electronic), 0161-5505 (Linking).

Riaz, A. et al. (2011). "Radiation segmentectomy: a novel approach to increase safety and efficacy of radioembolization". In: *Int J Radiat Oncol Biol Phys* 79.1, pp. 163–71. DOI: 10.1016/j.ijrobp.2009.10.062.

Riaz, Ahsun, Rafia Awais, and Riad Salem (July 2014). "Side Effects of Yttrium-90 Radioembolization". In: *Frontiers in Oncology* 4.

Roeske, John C. et al. (Sept. 2008). "Small-Scale Dosimetry: Challenges and Future Directions". In: *Seminars in Nuclear Medicine* 38.5, pp. 367–383.

Rong, X., Y. Du, and E. C. Frey (2012a). "A method for energy window optimization for quantitative tasks that includes the effects of model-mismatch on bias: application to Y-90 bremsstrahlung SPECT imaging". In: *Phys Med Biol* 57.12, pp. 3711–25. ISSN: 1361-6560 (Electronic), 0031-9155 (Linking).

Rong, X. et al. (2012). "Development and evaluation of an improved quantitative (90)Y bremsstrahlung SPECT method". In: *Med Phys* 39.5, pp. 2346–58. ISSN: 0094-2405 (Print), 0094-2405 (Linking).

Salem, Riad and Kenneth G. Thurston (Aug. 2006). "Radioembolization with 90Yttrium Microspheres: A State-of-the-Art Brachytherapy Treatment for Primary and Secondary Liver Malignancies". In: *Journal of Vascular and Interventional Radiology* 17.8, pp. 1251–1278.

Seidensticker, R. et al. (2012). "Hepatic toxicity after radioembolization of the liver using (90)Y-microspheres: sequential lobar versus whole liver approach". In: *Cardiovasc Intervent Radiol* 35.5, pp. 1109–18. DOI: 10.1007/s00270-011-0295-7.

Siman, W., J. K. Mikell, and S. C. Kappadath (2016b). "Practical reconstruction protocol for quantitative (90)Y bremsstrahlung SPECT/CT". In: *Med Phys* 43.9, p. 5093. ISSN: 2473-4209 (Electronic), 0094-2405 (Linking).

Smits, M. L. et al. (2015). "Radioembolization dosimetry: the road ahead". In: *Cardiovasc Intervent Radiol* 38.2, pp. 261–9. ISSN: 1432-086X (Electronic), 0174-1551 (Linking). DOI: 10.1007/s00270-014-1042-7.

Song, Y. S. et al. (2015). "PET/CT-Based Dosimetry in 90Y-Microsphere Selective Internal Radiation Therapy: Single Cohort Comparison With Pretreatment Planning on (99m)Tc-MAA Imaging and Correlation With Treatment Efficacy". In: *Medicine (Baltimore)* 94.23, e945. ISSN: 1536-5964 (Electronic), 0025-7974 (Linking).

Srinivas, Shyam M. et al. (Oct. 2014). "Determination of Radiation Absorbed Dose to Primary Liver Tumors and Normal Liver Tissue Using Post-Radioembolization 90Y PET". In: *Frontiers in Oncology* 4.

Strigari, L. et al. (Aug. 2010). "Efficacy and Toxicity Related to Treatment of Hepatocellular Carcinoma with 90Y-SIR Spheres: Radiobiologic Considerations". In: *Journal of Nuclear Medicine* 51.9, pp. 1377–1385.

Uliel, L. et al. (Nov. 2012a). "From the Angio Suite to the -Camera: Vascular Mapping and 99mTc-MAA Hepatic Perfusion Imaging Before Liver Radioembolization–A Comprehensive Pictorial Review". In: *Journal of Nuclear Medicine* 53.11, pp. 1736–1747.

Ulrich, G. et al. (2013). "Predictive value of intratumoral 99mTc-macroaggregated albumin uptake in patients with colorectal liver metastases scheduled for radioembolization with 90Y-microspheres". In: *J Nucl Med* 54.4, pp. 516–22. ISSN: 1535-5667 (Electronic), 0161-5505 (Linking).

Van Audenhaege, K. et al. (2015). "Review of SPECT collimator selection, optimization, and fabrication for clinical and preclinical imaging". In: *Med Phys* 42.8, pp. 4796–813. ISSN: 2473-4209 (Electronic), 0094-2405 (Linking).

Vauthey, J. N. et al. (2002). "Body surface area and body weight predict total liver volume in Western adults". In: *Liver Transpl* 8.3, pp. 233–40. ISSN: 1527-6465 (Print), 1527-6465 (Linking). DOI: 10.1053/jlts.2002.31654.

Vesselle, G. et al. (June 2015). "Radioembolization with yttrium-90 microspheres work up: Practical approach and literature review". In: *Diagnostic and Interventional Imaging* 96.6, pp. 547–562.

Vollmar, Brigitte and Michael D. Menger (Oct. 2009). "The Hepatic Microcirculation: Mechanistic Contributions and Therapeutic Targets in Liver Injury and Repair". In: *Physiological Reviews* 89.4, pp. 1269–1339.

Vouche, M. et al. (2013). "Radiation lobectomy: time-dependent analysis of future liver remnant volume in unresectable liver cancer as a bridge to resection". In: *J Hepatol* 59.5, pp. 1029–36. DOI: 10.1016/j.jhep.2013.06.015.

Walrand, S. et al. (2014a). "A hepatic dose-toxicity model opening the way toward individualized radioembolization planning". In: *J Nucl Med* 55.8, pp. 1317–22. ISSN: 1535-5667 (Electronic), 0161-5505 (Linking).

Walrand, S. et al. (2014b). "The low hepatic toxicity per Gray of 90Y glass microspheres is linked to their transport in the arterial tree favoring a nonuniform trapping as observed in posttherapy PET imaging". In: *J Nucl Med* 55.1, pp. 135–40. ISSN: 1535-5667 (Electronic), 0161-5505 (Linking).

Wiele, Christophe Van de et al. (July 2012). "SIRT of liver metastases: physiological and pathophysiological considerations". In: *European Journal of Nuclear Medicine and Molecular Imaging* 39.10, pp. 1646–1655.

Willowson, K. P. et al. (2015). "A multicentre comparison of quantitative (90)Y PET/CT for dosimetric purposes after radioembolization with resin microspheres : The QUEST Phantom Study". In: *Eur J Nucl Med Mol Imaging* 42.8, pp. 1202–22. ISSN: 1619-7089 (Electronic), 1619-7070 (Linking).

Wondergem, M. et al. (2013). "99mTc-macroaggregated albumin poorly predicts the intrahepatic distribution of 90Y resin microspheres in hepatic radioembolization". In: *J Nucl Med* 54.8, pp. 1294–301. DOI: 10.2967/jnumed.112.117614.

Yue, J. et al. (2016). "Comparison of quantitative Y-90 SPECT and non-time-of-flight PET imaging in post-therapy radioembolization of liver cancer". In: *Med Phys* 43.10, p. 5779. ISSN: 2473-4209 (Electronic), 0094-2405 (Linking).

Chapter 4

Image/Voxel-Based Dosimetry

Preface

^{90}Y radioembolization has several methods that may be utilized for post-treatment SPECT/CT dosimetry. The three image-based/voxel-based dosimetry methods for ^{90}Y radioembolization include the local deposition method, dose kernel convolutions, and Monte Carlo simulations. These methods have been previously compared (Pasciak and Erwin, 2009; Mikell et al., 2015b). However, each of these methods have discrete dosimetric inputs that may lie varied in implementation. Any differing inputs will lead to varied dose calculations even within a single methodology. Therefore, our second manuscript aimed to characterize these varying implementation effects based on the mono-compartmental model and local deposition method. These dosimetric methodologies were purposefully chosen due to a perceived clinical need, as methods that are most likely to be applied clinically. To aid in dosimetric comparability between voxel-based and current clinical methods, the mono-compartmental model was compared to the local deposition method. Importantly, the theoretical benefits of different dosimetric methodologies were tested while addressing the practical limitations of a clinical patient study. For reference, the voxel-based methods are described below.

Local deposition method

The local deposition method is an extension of the MIRD formalisms in equation 3.1. Instead of applying the assumptions of a homogeneous distribution at an organ level, the assumptions are applied at a voxel level. These assumptions are more favorable because the dosimetric assumptions follow the definition of a voxel. From a dosimetric perspective, the local deposition method assumes ^{90}Y microspheres are fixed after deposition and deposit their energy locally and homogeneously, i.e. the total energy produced is deposited within the same voxel (Bolch et al., 1999; Pasciak and Erwin, 2009; Pasciak, Bourgeois, and Bradley, 2014; Mikell et al., 2015b). A straightforward dose calculation, the local deposition method requires only a scalar factor to convert activities to dose. To obtain its scalar factor, the average energy of ^{90}Y emitted per beta decay is assumed to be energy absorbed per decay.

Dose Point Kernels

The DPK is a method that requires an initial Monte Carlo simulation with a point source. A DPK is generated when both electron and photon radiation transport is simulated and dose per particle fraction maps are generated at select radial distances. These dose fraction maps are then convolved to either SPECT or PET activity maps. To note, DPKs simulate volumes with homogeneous mass densities and materials, typically derived from the ICRU report 46 (White, Griffith, and Wilson, 1992; Erdi et al., 1998). A different DPK must be simulated for a different mass density and material i.e. an organ type. Fig. 4.1 nicely visualizes this process.

A type of DPK, the S-value convolution (kernel) follows the same methodology as DPKs but uses a voxel source (cubed) instead of a point source, divides the simulation volume into voxels, and measures dose per particles for every simulated voxel instead of dose per particle fractions. This resulting dose kernel is matched with the voxel sizes of PET/CT or SPECT/CT and assumes that every activity voxel has the same radiation transport, i.e. a spatially invariant kernel. These assumptions makes dose

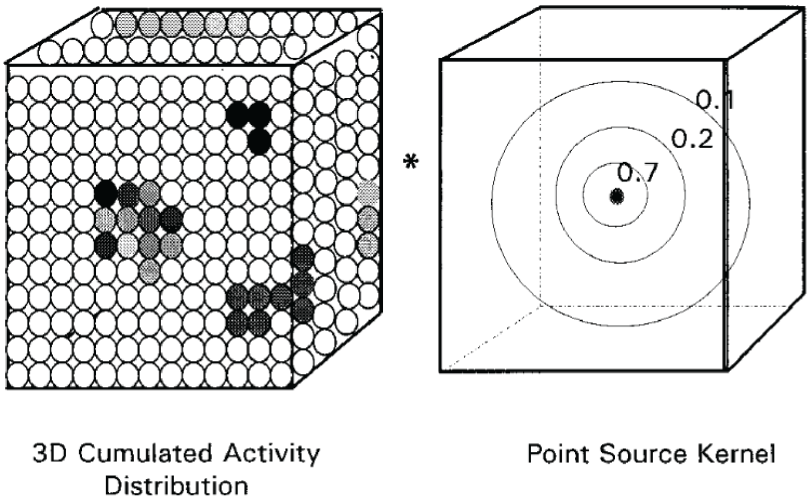

FIGURE 4.1: The matrix on the left depicts the spatial distribution of SPECT. The cube on the right depicts the $3D$ DPK. The absorbed dose calculation is the convolution of these two 3-D functions. Direct convolution is implemented as follows: (1) Position the center of the left matrix at a given point in the left matrix. (2) Multiply each voxel of right matrix by the voxel of the left matrix. (3) Sum all products. (4) Shift center to new voxel and repeat steps 2-3. Reproduced from (Erdi et al., 1998).

calculation faster than traditional DPK methods (Dezarn et al., 2011b). An even simpler approximation, the S-value method converts the same kernel to a table of S-values that allows even simpler voxel-based calculations (Bolch et al., 1999).

Monte Carlo

A full Monte Carlo simulation requires information such as the patient geometry, mass density, elemental composition of the involved tissue types, and radionuclide positions to provide an accurate and patient-specific dosimetric result. Monte Carlo simulations are theoretically the most accurate of the three dosimetric techniques. The purpose of Monte Carlo simulations are to find the golden standard or benchmark solution to be used for comparisons. However, Monte Carlo simulations are only as accurate as the inputs to the simulation. Within radioembolization, the errors that occur due to both image acquisition and processing impact the eventual Monte Carlo simulation result greatly.

Characterizing SPECT/CT dosimetry following radioembolization with yttrium-90 microspheres

Abstract

Background: Multiple post-treatment and image-based dosimetry methods are currently under investigation for Yttrium-90 (^{90}Y) radioembolization. Within each methodology, a variety of dosimetric inputs exist that affects the final dose estimate. Understanding their effects is essential to facilitating proper dose analysis and crucial in the eventual standardization of radioembolization dosimetry. The purpose of this study is to investigate dose differences due to different self-calibrations and mass density assignments in the mono-compartmental and local deposition methods. A practical mean correction method is introduced that permits dosimetry in images compromised by patient motion and partial volume effects.

Methods: 21 patients underwent ^{90}Y radioembolization and were imaged with SPECT/CT. Five different self-calibrations (FOV, Body, OAR, Liverlung, Liver) were implemented and dosimetrically compared. The mono-compartmental and local deposition method were used to perform dosimetry based on either nominal or CT calibration-based mass densities. A mean correction method was derived assuming homogeneous densities. Cumulative dose volume histograms, linear regressions, boxplots, and Bland Altman plots were utilized for analysis.

Results: Up to 270% weighted dose difference was found between self-calibrations. The local deposition and mono-compartmental methods, the liver and lung had dose differences within 0.70 Gy and 20 Gy, respectively. The local deposition method's nominal and CT calibration-based mass density implementations. Dosimetric indices were within 1.4% in the liver and 24% in the lungs. The lung mean doses calculated with the CT method were shown to be overestimated. The mean correction method demonstrated that the corrected mean doses had 95% confidence interval differences at 4.1 Gy

in the liver and within 20% of the mean doses in the lung.

Conclusions: The Body, OAR, and Liverlung calibrations may represent the lower, ideal, and upper absorbed dose limits. The mono-compartmental method was found more comparable to the local deposition method in more homogeneous organs. Due to the potential for inflated lung mean doses, the mono-compartmental and local deposition method implemented with nominal mass densities is recommended for more consistent dosimetric results. If patient motion and partial volume effects are present in the liver, our practical correction method will calculate more representative doses in images suboptimal for dosimetry.

4.1 Introduction

Three dimensional voxel-based dosimetry is an active area of investigation in an internal radiation therapy called radioembolization to improve upon its simple clinical dosimetry. Radioembolization is an angiographic procedure where a catheter is used to guide and inject Yttrium-90 (^{90}Y) microspheres into a specifically selected hepatic artery. Due to unique hepatic blood flow, the microspheres are distributed preferentially in the tumour arteries, where they are permanently deposited. The tumour is then irradiated by the β^- particles emitted from ^{90}Y decay.

Radioembolization's dosimetry may be grouped into two categories that include methods clinically practiced and those emerging within the field. The dosimetric methodologies clinically suggested are the partition and the mono-compartmental models. These models are based on the Medical Internal Radiation Dose (MIRD) schema and apply two gross assumptions; (1) the injected microsphere sources distribute uniformly within a region of interest (ROI), which may include an entire organ and (2) the dose is distributed entirely within the liver and lungs Dezarn et al., 2011b. The MIRD schema typically applies planar gamma imaging to calculate a lung shunt fraction that is later used to perform simple clinical dosimetry. Significant limitations to planar gamma

imaging exist. As a modality, planar gamma cameras lack proper attenuation, scatter, and volume corrections for dosimetry. Planar gamma imaging has been shown to overestimate lung shunt fractions Allred et al., 2018b; Elschot et al., 2014. In contrast, radioembolization's emerging methods are directly image-based and combine functional PET or SPECT images containing information regarding positions of the injected radionuclides with anatomical CT images to produce a 3D activity distribution. For SPECT/CT, reconstructions that were traditionally qualitative have significantly progressed to produce algorithms that are quantitative in nature enabling patient specific treatment planning and subsequent dose verification Rong, Du, and Frey, 2012b; Siman, Mikell, and Kappadath, 2016a; Dewaraja et al., 2017b; Porter et al., 2018. There are currently three voxel-based dosimetry methods for ^{90}Y radioembolization: the local deposition method, dose kernel convolutions including the S-value convolutions, and Monte Carlo simulations.

4.1.1 Current Status of ^{90}Y Dosimetry

Methodologies for ^{90}Y SPECT/CT dosimetry have become more established in recent years. Previous studies have demonstrated that the spatial resolution of SPECT systems is the main limitation to accurate voxel-based dosimetry due to blurring of the original source distributions by their own system dependent resolution limits and biases Ljungberg and Sjögreen-Gleisner, 2011; Pacilio et al., 2015. When comparing between voxel-based methods, all methodologies have shown comparable dosimetric differences between the true dosimetric result and those obtained from SPECT/CT images Ljungberg and Sjögreen-Gleisner, 2011; Pacilio et al., 2015. It is thought that primarily self-irradiation and negligible dosimetric differences occur because voxel sizes are equal to or greater than the mean path length of a β^- particle. Nevertheless, there has been evidence that the dosimetry performed on blurred SPECT images even with smaller voxels is the most accurate with the local deposition method over other voxel-based methodologies Pasciak and Erwin, 2009. The ease of use and potentially

improved accuracies have made the local deposition method a favoured methodology.

To produce dosimetric maps, a quantitative SPECT image is required. The quantitative image depicts the activity in each voxel rather than hardware-specific counts. In standard SPECT imaging there are two ways of obtaining the counts-to-activity calibration: either a phantom study using the same reconstruction protocol as the patient study is performed or the field-of-view (FOV) must encompass the entire patient. In ^{90}Y radioembolization, SPECT/CT images are acquired with bremsstrahlung photons that produces a wide and continuous energy spectrum; correcting for photon scatter, septal penetration, and collimator scatter cannot be adequately achieved with a phantom study **iaea2015**; Heard et al., 2003; Siman, Mikell, and Kappadath, 2016a. Instead, since the microspheres are injected directly into the patient's hepatic vasculature and become permanently deposited, it is assumed that a single abdominal FOV contains all the relevant activity. Called the self-calibration, this calibration method has been widely adopted to perform patient specific dosimetry on SPECT/CT Dieudonne et al., 2011; Chiesa et al., 2015; Pacilio et al., 2015; Mikell et al., 2015b; Kappadath et al., 2018b; Potrebko et al., 2018. There is no consensus as to the exact volume within the FOV in which it is assumed all true counts are contained.

As an open dosimetric question, different calibration assumptions have been adopted within the field. The clinical mono-compartmental and partition methods have implicitly assumed that the relevant counts are contained solely within the liver and the lung Dezarn et al., 2011b. Within emerging voxel-based methods, self-calibrations have included the liver itself, the patient's body, and the entire SPECT FOV Dieudonne et al., 2011; Chiesa et al., 2015; Pacilio et al., 2015; Mikell et al., 2015b; Potrebko et al., 2018; Kappadath et al., 2018b. A study comparing such calibrations have indicated large dosimetric variations, but the current clinical assumptions were not addressed Balagopal and Kappadath, 2018. Additionally, there is no guarantee that microspheres will deposit within the liver even after coil embolization Kim et al., 2019b. The microspheres may shunt to the lungs, and have extrahepatic depositions that include the

gallbladder, stomach, duodenum, kidneys, and lungs Kao et al., 2013c; Favelier et al., 2015. A new calibration that represents the most likely areas of hepatic depositions was explored to consider such limitations.

If acquired images are quantitative, post-treatment dosimetry may be performed with clinical methodologies when emerging voxel-based methods are not available. The comparability between the local deposition method and clinical methodologies are still unknown for ^{90}Y SPECT/CT. Moreover, the local deposition method has been implemented with different methodologies that utilize either nominal or CT based mass densities Mikell et al., 2015b; Potrebko et al., 2018; Pasciak and Erwin, 2009; Balagopal and Kappadath, 2018. Nominal densities assume that densities within organs are homogeneous while CT derived densities utilize a scanner specific Hounsfield unit to density calibration curve. Applicable to clinical methodologies, the dose effects between mass density implementations have not yet been explored. Previous studies demonstrated patient motion and partial volume factors affect dosimetric accuracy Pacilio et al., 2015; Mikell et al., 2015b; Allred et al., 2018b. Although image blurring is unavoidable in voxel based dosimetry, patient motion or partial volume effects that spread activities outside organ delineations cause the dosimetric validity on such images, especially when activities bleed between organs, to become questionable. A dosimetric correction method would be useful in addressing these imaging limitations.

The purpose of this study is to clarify the dose effects of varying dosimetric variables and introduce a method for countering imaging limitations. The overarching goal is to aid in the standardization of radioembolization's ^{90}Y SPECT/CT voxel-based dosimetry. To achieve this goal, this study has the following aims: (1) To expand upon the dosimetric effects of existing calibration and introduce a new calibration, (2) compare the dosimetry between mass density implementations of the mono-compartmental and local deposition method, and (3) demonstrate a practical correction method to account for patient motion and partial volume effects.

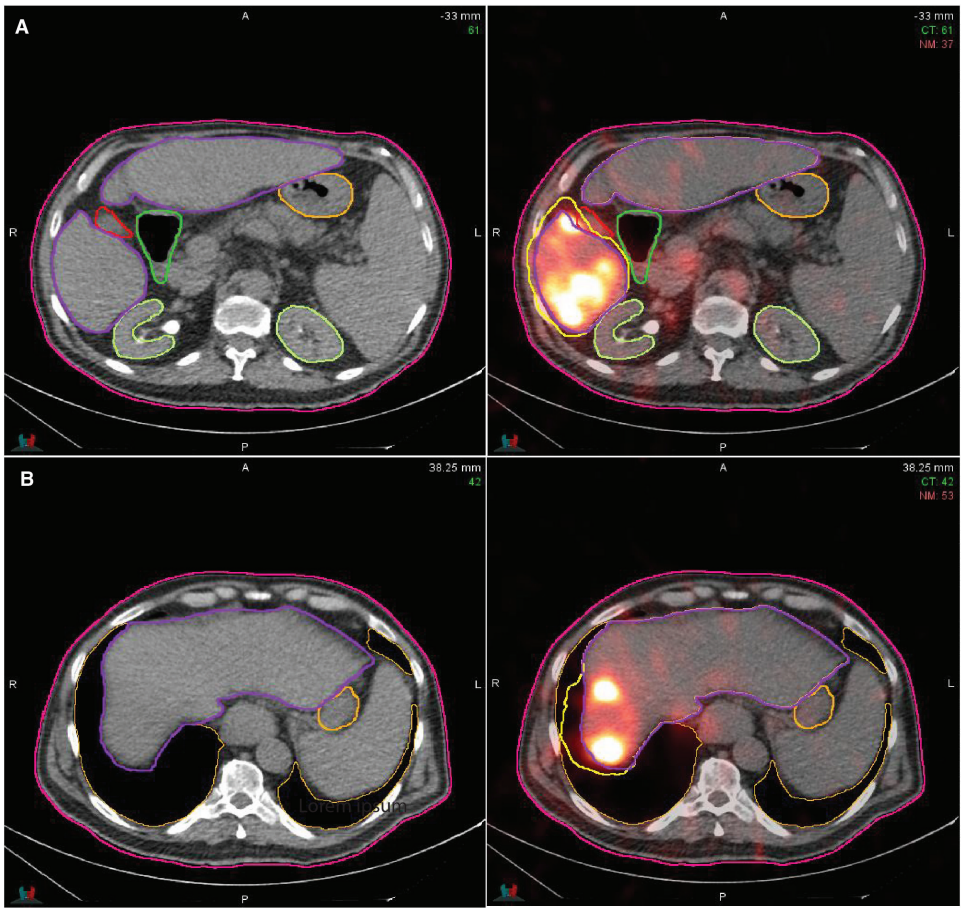

FIGURE 4.2: Contour of two axial slices for one patient are visualized where the left represents the CT and the right represents a SPECT/CT fused image. The purple contour represents the original liver contours whereas the yellow represents the correction contour that includes valid, but misplaced activities either due to partial volume effects or patient motion.

4.2 Materials and Methods

4.2.1 Patient Population

This retrospective study received approval from our institutional review board and was performed on an anonymized patient-based cohort of 21 ^{90}Y SPECT/CT image sets. All patients were treated with glass microspheres (TheraSphere; Boston Scientific, USA) and clinical dosimetry was planned using the mono-compartmental method. The mean injected activity was 3.01 ± 2.05 GBq with a range of $0.649 - 8.96$ GBq. Two patient cohorts were categorized within this study: optimal and suboptimal. Table

TABLE 4.1: List of Dosimetric Variables Tested

Tested Variable (Units)	Analysis Method	Analysis Result
1. Volumes (%)	$max(\frac{Nominal-CT}{CT}, \frac{CT-Nominal}{Nominal})$	Volume Bias
2. Interpolations ($Distance$)	Chi-square histogram	Interpolation Bias
3. Self-calibrations	Linear regression slopes	Weighted dose %s
4. Mean dose (Gy)	Bland Altman	95% CIs
5. Mass densities	Linear regression slopes	Weighted dose %s
6. Mass density DVH (Gy)	Bland Altman	95% CIs
7. MIRD vs. LDM* Methods (Gy)	Boxplots	Dose biases
8. Correction Means (Gy)	Boxplots, Bland Altman	Dose biases, 95%CI

*LDM: Local deposition method

4.1 lists a summary of all variables tested. Inclusion criteria for the optimal cohort were images that allowed for accurate organ contours on low-dose CT, counts that were completely delineated within CT contours (i.e. no motion artifacts nor excessive partial volume effects) for optimal dose comparisons, and complete dosimetry information. Only five patients remained for optimal local deposition comparisons. Six patients had CT images that were unable to be contoured due to insufficient contrast, two patients lacked sufficient treatment information to perform dosimetry, and eight patients had counts outside CT contoured delineations that were deemed from patient motion or partial volume effects. These same eight patients were categorized as the suboptimal cohort. The optimal cohort were used to test variables 1-7 while the suboptimal cohort was used to demonstrate our correction methodology. Truncated lungs within the FOV was not an exclusion criteria. Only one patient had their entire abdomen and lung visualized within the SPECT/CT FOV.

4.2.2 Image Acquisitions

All patient images were acquired on a Discovery NM/CT 670 SPECT/CT system (GE Healthcare, Cleveland, USA) with a parallel-hole medium-energy general purpose collimator. SPECT data was acquired with a 109.1–134.2 keV window for 120 views over 360with 30 s/view. Quantitative reconstructions were performed on HybridRecon

TABLE 4.2: Preprocessing Biases between the Nominal and CT image inputs are summarized for organ volume calculations and interpolation methodologies

	Volume Bias (%)		Quadratic Chi-Histogram ($Distance$)			
Patient	Liver	Lung	Nearest Neighbor	Bilinear	Biquadratic Spline	Bicubic Spline
Patient 1	0.229	1.324	$1.350e10^{-5}$	$3.677e10^{-4}$	$4.972e10^{-3}$	$5.275e10^{-3}$
Patient 2	0.050	0.798	$6.780e10^{-5}$	$1.728e10^{-4}$	$1.727e10^{-3}$	$1.863e10^{-3}$
Patient 3	0.439	3.684	$1.569e10^{-5}$	$3.340e10^{-4}$	$5.595e10^{-3}$	$5.917e10^{-3}$
Patient 4	0.487	0.273	$5.600e10^{-5}$	$2.080e10^{-4}$	$3.115e10^{-3}$	$3.316e10^{-3}$
Patient 5	0.675	0.895	$1.081e10^{-5}$	$3.204e10^{-4}$	$5.314e10^{-3}$	$5.640e10^{-3}$

(Version 1.3, Hermes Medical Solutions) and consisted of 3D ordered-subset expectation maximum (OSEM) reconstructions with attenuation correction based on a low-dose helical CT, scatter corrections based on a Monte Carlo convolution-based forced detection algorithm, and collimator detector response modeling Jong, Slijpen, and Beekman, 2001. All quantitative reconstructions were performed with an equivalent 75 iterations (15 subsets and 5 iterations) based on manufacturer recommendations Porter et al., 2018. No post-filter was applied and the reconstructed SPECT voxel sizes were isotropic at 4.417 mm.

When required, CT mass densities were calculated using a scanner-specific linear lookup table based on electron density phantom scans. The CT voxels were reconstructed with sizes 0.976 mm x 0.976 mm x 3.75 mm. All contours were drawn on the low-dose helical CT using tools from MIM Maestro v6.6 (MIM) and followed established contouring guidelines Jabbour et al., 2014. Any overlapping contours were corrected with boolean operations. The contours were verified by an experienced nuclear medicine physician.

4.2.3 pyreDose

pyreDose is an in-house open-source software package developed for this study. It used to perform image processing and dosimetry. pyreDose is written in Python and currently consists of dosimetry methods based on the local deposition, its variations, and the clinical MIRD methods. pyreDose was used to process DICOM images, create self-calibration, perform interpolations, and calculate absorbed doses. To perform such

analysis, each patient's set of SPECT and CT images and contoured structures saved in there respective DICOM formats were imported to pyreDose. With regards to contour creation, the entire voxel was deemed to be in the contoured organ if the center of a voxel was contained within a contour. The resulting contour regions of interest (ROI) were used to perform organ dosimetry and create self-calibrations.

4.2.4 Self-calibrations

Prior to performing dosimetry, SPECT counts were converted to activity specific to a self-calibration. The self-calibration was implemented by equating the administered activity to the total counts within specified SPECT ROI to convert voxel counts into activity per patient. Equation 4.1 demonstrates the calibration mathematically where image voxel activities (x_k) are calculated dependent on the total number of voxels (n) contained within a self-calibration, corresponding voxel counts (c_k), and the administered activity (A).

$$x_k = A * \frac{c_k}{\sum_{k=1}^{n} c_k} \tag{4.1}$$

The different self-calibrations were determined based on their clinical relevance and use within the literature Dieudonne et al., 2011; Chiesa et al., 2015; Pacilio et al., 2015; Mikell et al., 2015b; Kappadath et al., 2018b; Potrebko et al., 2018. The different self-calibrations were titled FOV, Body, OAR, Liverlung, and the Liver. The FOV calibration represented the assumption that all SPECT counts have valid activity. The Body calibration illustrates a conservative, but robust post-processing methodology based on MIM's auto-body contouring Balagopal and Kappadath, 2018. Because microspheres cannot travel outside the body, all body contours were manually checked to remove any inclusion of contoured arms and corrected for any air pockets. The organs at risk (OAR) calibration was introduced to test a more accurate and precise calibration. These

organs included organs with likely microsphere depositions based on a standard hepatic vasculature. These organs were the liver, lung, gallbladder, stomach, proximal duodenum, and kidneys. The Liverlung calibration contained the liver and the lung counts and represented the clinical dosimetric assumptions. Although it is well documented that microspheres travel into the lungs, standalone liver calibrations have been increasingly used for dosimetry and imaging studies Balagopal and Kappadath, 2018; Pacilio et al., 2015; Siman, Mikell, and Kappadath, 2016a. To illustrate the effects of such assumptions, the Liver calibration was included.

4.2.5 Image-based Dosimetry

Dosimetry was performed with two separate mass densities implementations for the local deposition method Pasciak, Bourgeois, and Bradley, 2014; Mikell et al., 2015b. The mono-compartmental model, subsequently labelled the MIRD method, has manufacturer guidelines, but lacks a consensus with regards to mass calculations Dezarn et al., 2011b. Therefore, differences in mass density implementations were investigated for the MIRD method.

All absorbed doses were calculated based on ^{90}Y SPECT/CT images. If nominal based densities were mapped for entire organs, it was titled the Nominal method. If voxel by voxel density assignment was based on CT values, it was titled the CT method. For voxel dosimetry, the CT method requires prepossessing so that the SPECT voxels match in size and position to the co-registered CT densities. This voxel matching may be achieved through interpolating the SPECT image to match the CT voxels, decimation of the CT image to match the SPECT voxels, or any combination of the two. To perform dosimetry without any loss of information, the SPECT image was interpolated using the nearest neighbor algorithm. This method was chosen amongst multiple interpolation methods since it performed best in a correspondence analysis.

The local deposition method was implemented following a voxel dose as indicated in Equation 4.2 with image voxel activities x_k, mass densities ρ_k, voxel volumes ΔV_k, and

a constant based on the local deposition method's conversion of activity to absorbed energy.

$$Dose_k = \frac{x_k}{\rho_k} * \frac{\overbrace{E_{avg} * 1.602 * 10^{-13} * \frac{1}{ln(2)} * t_{\frac{1}{2}}}^{const}}{\Delta V_k} \tag{4.2}$$

The MIRD method was calculated with the same parameters as Equation 4.2, but following the MIRD assumptions where n in Equation 4.3 refers to the total voxels within an organ.

$$Dose_{mird} = \frac{\sum_{k=1}^{n} x_k * const}{\sum_{k=1}^{n} \rho_k * \Delta V_k} \tag{4.3}$$

The Nominal MIRD and local deposition methods necessitate nominal densities based on ICRU report 46 to be mapped onto a SPECT image White, Griffith, and Wilson, 1992. Density values of 1.06 g/cm^3 and 0.26 g/cm^3 were used as the respective liver and lung densities for ρ_k while x_k was based on the original SPECT image. The CT MIRD and local deposition methods utilized the mass densities ρ_k derived from a CT calibration curve while x_k was derived from interpolated SPECT images.

4.2.6 Calculating Corrected Mean Doses

Especially relevant for radioembolization, imaging issues such as patient motion and partial volume effects cause dose inaccuracies when valid voxel activities become spatially misplaced. Having an abdominal FOV, activity in the liver commonly spills over into neighboring organs due to motion as scan times are long and free breathing is required. Partial volume effects may further cause activities within the liver to bleed

into the lung Mikell et al., 2015b. A potential correction may be implemented if the initial spatial locations of such activities are known, but typically this is not the case. By applying the assumptions of the local deposition method and assuming homogeneous/nominal mass densities, a theoretical relocation of counts to the correct voxel is possible without requiring a priori knowledge of its spatial location. A practical mean correction method may be derived starting with the equation of the mean dose.

$$Dose_{mean} = \frac{1}{n}\sum_{k=1}^{n}\frac{x_k}{p_k} * \frac{const}{\Delta V_k} \tag{4.4}$$

From the definition of an image, all voxel volumes are equal while the conversion from activity to dose stays constant, which permits Equation 4.5.

$$Dose_{mean} = \frac{const}{n * \Delta V}\sum_{k=1}^{n}\frac{x_k}{p_k} \tag{4.5}$$

The mean dose may be divided into voxels with activities that require no corrections (x_i) and incorrect (x_j) activities where misplaced activities y_j should be added.

$$Dose_{corr} = \frac{const}{n * \Delta V} * (\sum_{i=1}^{n_{corr}}\frac{x_i}{p_i} + \sum_{j=1}^{n_{incorr}}\frac{x_j + y_j}{p_j}) \tag{4.6}$$

$p_i = p_j$ due to homogeneous mass densities and all activities get added. Therefore, the voxels containing both correct and incorrect voxels (x_k) may be grouped together as the original activities while voxels that contain misplaced activities (y_w) are separated.

$$Dose_{corr} = \frac{const}{n * p * \Delta V} * (\sum_{k=1}^{n} x_k + \sum_{j=1}^{n_{misplaced}} y_j) \tag{4.7}$$

Equation 4.7 displays the derived correction method to calculate mean organ absorbed doses. In this study, the correction method was used to obtain more representative liver mean doses when activities in the liver bled into other organs. These corrections were achieved by first creating correction contours that included counts outside organ delineations. Illustrated in Fig. 4.2, y_j was defined as counts contained within the corrected volume, but outside the original contours. If any counts spilled into other organs such as the lungs, the same counts were excluded from the other organs. Because self-calibration are dependent on organ delineations, the corrected organ contours were utilized to create corrected self-calibrations before dosimetry.

4.2.7 Statistical Tests

All statistical tests were performed and visualized with Python. The quadratic chi-histogram distance metric was used to compare the error between interpolation methods as seen in Equation 4.8. This test measures the image correspondence between two differing images and their normalized histograms with the same binning. x_i and y_i represent the two frequency histograms and their respective bins i. A lower distance metric pertains to closer correspondence where a distance of 0 represents equated histograms.

$$distance = \frac{1}{2}\sum_{i=1}^{n}\frac{(x_i - y_i)^2}{x_i + y_i} \tag{4.8}$$

Cumulative dose volume histograms (DVHs) were computed for all compared dosimetric indices. D_x was defined as the minimum dose that x% volume would obtain. Bland Altman analysis was performed to illustrate the dosimetric differences between local deposition methodologies and correction differences. Multiple DVH indices (D_{70}, D_{50}, D_{20}, D_{10}), mean dose estimates, and all self-calibrations were used to calculate the

mean, standard deviation, and 95% confidence intervals (CI) of bias for the Bland Altman analyses. If heteroscedastic trends were observed in any Bland Altman plots, the same data was log_{10} transformed, then used to recalculate their CIs and means biases that now represented log-ratios Bland and Altman, 1986. When creating Bland Altman plots, any log-transformed CIs were then back-transformed and plotted on the regular scale for intuitive visual analysis Euser, Dekker, and Cessie, 2008. These back-transformed slopes were defined as CIs that are dependent on the mean or the x-axis of Bland Altman plots. When performing linear regressions, the same dosimetric indices were compared between the CT and Nominal local deposition methods. The correlation coefficients (*r*) and their slopes were computed.

4.3 Results

4.3.1 Image Processing Discrepancies

Table 4.2 summarizes the discrepancies in the image inputs between the Nominal and CT data. The Nominal methods utilize contours drawn on CT and overlayed to the original SPECT images, which may result in organ volume errors. The liver and lung volume differences between the CT and Nominal inputs resulted in only a maximum volume deviation of 3.7%. The CT methods require interpolations that have their own biases. All interpolation methods had small similarity distances ($< 6.0x10^{-3}$) between the interpolated SPECT images and original quantitative SPECT reconstruction demonstrating excellent correspondence.

4.3.2 Self-calibration Comparisons

Two patients and their liver and lung DVHs are shown for the MIRD and local deposition methods in Fig. 4.3. Visually, the FOV and Body calibrations and the OAR, Liverlung, Liver calibrations were grouped together to create two calibration groupings. The liver DVHs between the CT and Nominal local deposition methods were visually

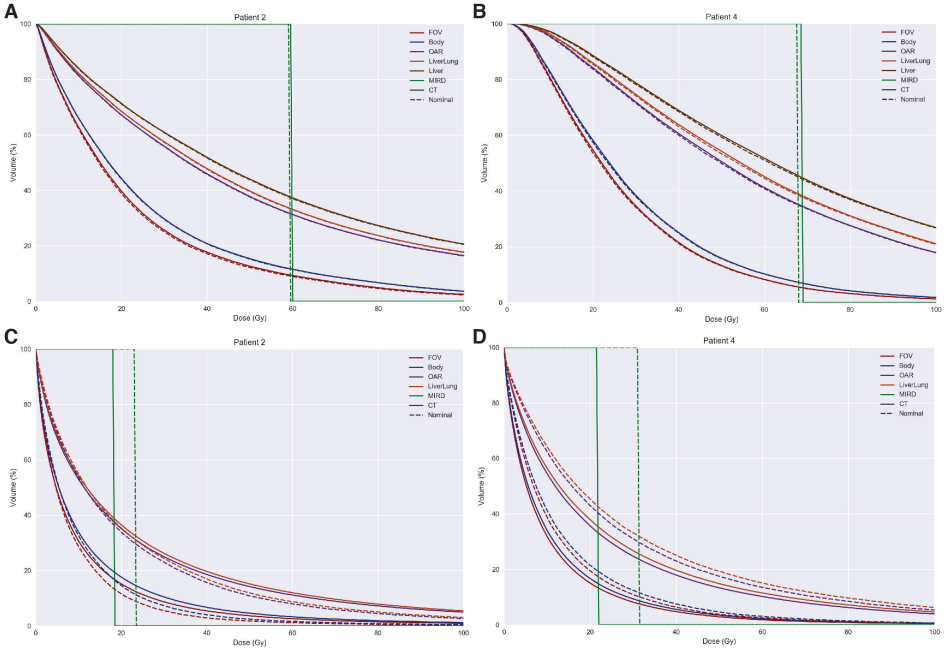

FIGURE 4.3: Liver (A-B) and Lung (C-D) cumulative dose volume histograms (DVH) are shown for two patients. Each DVH includes the CT and Nominal local deposition methods for different self-calibrations and the MIRD method calibrated solely with the Liverlung rationale.

indistinguishable from one another. The MIRD assumptions within the MIRD method created a characteristic square curve. Overall as the calibrations included smaller ROI, the DVHs shifted right and upwards.

The mean doses of multiple self-calibration were compared through linear regression slopes, which are summarized within Table 4.3. Correlation coefficients (r) were $>$ 0.958 between all mean doses of varying self-calibrations, illustrating excellent linear correlations. These linear regression slopes represent a weighted dose factor and a percentage change that occurs between mean doses of varying calibrations. In this context, the liver had an 8.8% difference in the calculated dose between the FOV and Body calibrations, and a 5.4% difference between the OAR and LiverLung calibrations. There was a $\sim$15% difference between the liver dose calculated with the Liverlung calibration and the Liver calibration. When compared to the FOV calibration, both the liver and lung mean dose factors increased as the calibrations change from the Body to the OAR and finally to the Liverlung. Within the liver, the FOV and Liver regression comparisons had the highest slope at $\sim$2.7 for both the Nominal and CT

TABLE 4.3: The CT and Nominal local deposition methods were compared to their respective calibration for both the liver and lung. These comparisons were performed on their mean doses.

		Linear Regression Slopes									
		FOV		Body		OAR		Liverlung		Liver	
Region	Parameter	CT	Nominal	CT	Nominal	CT	Nominal	CT	Nominal	CT	Nominal
Liver	FOV	**1.000**	**1.000**	1.081	1.088	2.239	2.254	2.361	2.374	2.712	2.729
	Body	0.923	0.916	**1.000**	**1.000**	2.069	2.067	2.180	2.173	2.502	2.498
	OAR	0.446	0.443	0.482	0.483	**1.000**	**1.000**	1.054	1.051	1.210	1.209
	Liverlung	0.423	0.421	0.457	0.459	0.948	0.951	**1.000**	**1.000**	1.149	1.151
	Liver	0.361	0.366	0.398	0.398	0.823	0.825	0.870	0.869	**1.000**	**1.000**
Lung	FOV	**1.000**	**1.000**	1.100	1.069	2.275	2.210	2.382	2.329	X	X
	Body	0.907	0.933	**1.000**	**1.000**	2.065	2.063	2.162	2.170	X	X
	OAR	0.439	0.451	0.483	0.483	**1.000**	**1.000**	1.046	1.053	X	X
	Liverlung	0.419	0.428	0.462	0.457	0.955	0.949	**1.000**	**1.000**	X	X

local deposition methods. For the lung, the FOV and Liverlung regression comparisons had the highest slope ranging from 2.3 to 2.4 for the CT and Nominal local deposition methods.

4.3.3 Nominal vs. CT Local Deposition Methods

The dosimetric indices between the CT and Nominal local deposition methods for all the self-calibrations were investigated. Fig. 4.4a illustrates the linear regressions and Table 4.4 lists the linear regression slopes and their corresponding *r* values. The liver regression slopes between the CT and Nominal local deposition methods demonstrated near perfect correlation with all their $r \geq 0.99$. With near perfect linear correlations, D_{70}, D_{50}, D_{10}, and mean doses demonstrated that the CT local deposition method had a liver dose that was within 1.4% of the dose calculated with the Nominal local deposition method.

In the comparisons between the CT and Nominal local deposition method, lung slopes illustrated an increasing trend as the dosimetric indices changed from D_{90} of 0.76 to D_{10} of 0.94. This trend demonstrated that as the volume of D_x decreased, the dose minimum estimates of the CT method increased at a rate faster than the Nominal method. Visually represented in Fig. 4.3, this may be seen as a right shift for the CT local deposition method at lower volumes of D_x. For the lung, all regression slopes were below

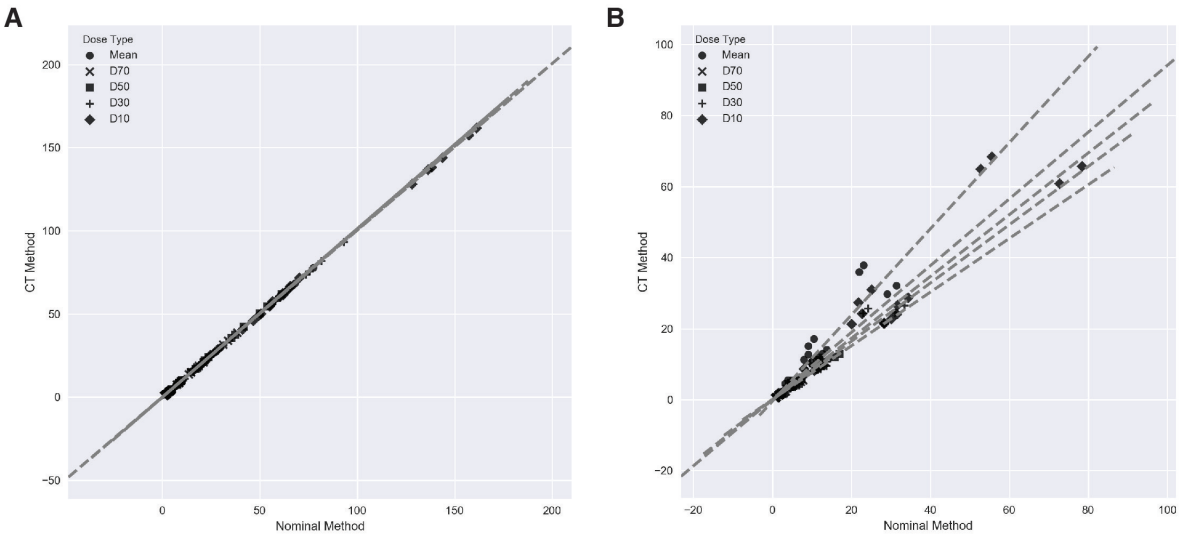

FIGURE 4.4: The linear regressions representing weighted dose factors of cumulative dose volume histogram (DVH) and mean dose estimates for the (A) liver, $N = 25$ and (B) lung, $N = 20$. Each linear regression compared the mass density effects between the CT and Nominal local deposition methods for a particular dose metric. N represents the number of data points compared for each dose metric for a particular organ.

1.0 indicating dose estimates for the Nominal local deposition method were generally greater than those of the CT method. There was one exception; the linear slope for the lung mean dose was 1.2, indicating a greater dose for the CT method over the Nominal method.

Fig. 4.5a is a Bland Altman analysis between the mean doses of the CT and Nominal local deposition methods. For both the liver and lung Bland Altman analyses, the bias was defined as the CT subtracted by Nominal mean doses of the local deposition method. The liver mean bias was 0.18 Gray with a CI -0.26-0.62 Gy while the lung mean bias was 2.1 Gy with a CI -7.5-12 Gy. Both liver and lung mean biases suggested larger mean doses for the CT local deposition method.

Similarly, Fig. 4.5b had its bias defined as the CT method subtracted by the Nominal method for local deposition method's DVH indices. The mean bias of the liver DVH indices was 0.17 Gray, indicating DVH indices based on the CT method were slightly greater than those of the Nominal method. In contrast, the mean log-ratio bias of the lung DVH was -0.1, (Table 4.6) demonstrating that the lung DVH indices based on the

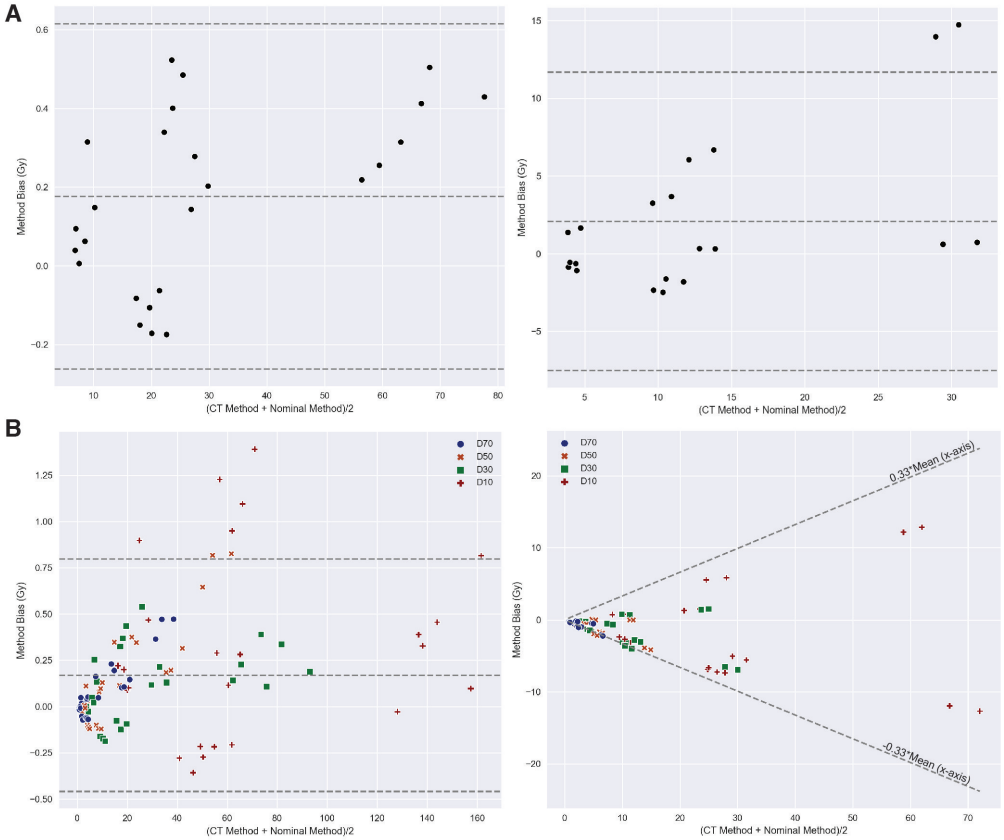

FIGURE 4.5: The liver (left) and lung (right) Bland Altman analysis between mean doses (A) and cumulative dose volume histogram (DVH) metrics (B) for the CT and Nominal local deposition methods were illustrated. Between the mean doses, the liver mean doses of all self-calibrations were include, $N = 25$ while the lung mean doses did not include the Liver calibration, $N = 20$. Between DVH metrics, the liver contained the DVH indices for every self-calibration, $N = 100$ while the lung did not contain the Liver calibration, $N = 80$. N represents the number of data points compared for each Bland Altman plot.

Nominal method were generally greater than the CT method. The back-transformed slope was 0.3, showing that the 95% CI were within 30% of the lung mean dose values.

4.3.4 MIRD Dose Comparisons

Fig. 4.6 illustrates the dosimetric comparisons between consistently calibrated methodologies. Between the Nominal and CT MIRD methods, the Liver doses were within 0.70 Gy while the lung doses were within 10 Gy. With negative values, the Nominal MIRD method demonstrated greater lung doses than those calculated with the CT MIRD method. The comparisons within the CT methods between the MIRD and local

TABLE 4.4: Linear Regression Slopes between the CT and Nominal local deposition method was summarized for multiple dose metrics

	Liver		Lung	
Metric	Slope	*r* value	Slope	*r* value
Mean	1.005	0.999	1.213	0.910
D_{70}	1.013	0.999	0.756	0.981
D_{50}	1.014	0.999	0.821	0.972
D_{30}	1.003	0.999	0.870	0.966
D_{10}	1.001	0.999	0.940	0.942

TABLE 4.5: Mean Absorbed Doses were summarized for CT and Nominal MIRD methods and CT and Nominal local deposition methods. These mean doses were based on the Liverlung calibration

		Absorbed Doses (Gy)									
		Patient 1		Patient 2		Patient 3		Patient 4		Patient 5	
Method	Organ	CT	Nominal	CT	Nominal	CT	Nominal	CT	Nominal	CT	Nominal
MIRD	Liver	23.78	23.51	59.72	59.34	19.54	19.77	68.62	67.92	19.93	20.17
	Lung	7.266	11.58	18.15	23.12	6.415	9.073	21.64	31.38	7.620	12.64
Liverlung	Liver	23.91	23.51	59.59	59.34	19.67	19.77	68.42	67.92	20.00	20.17
	Lung	9.094	11.58	37.85	23.12	12.75	9.073	32.11	31.38	10.83	12.64

deposition methods resulted in differences within 0.30 Gy for the liver and within 20 Gy for the lungs. However, all the Nominal dose differences between the MIRD and local deposition methods were 0 Gy. The mean absorbed doses for the MIRD method and local deposition methods both calibrated with the Liverlung rationale are included in Table 4.5.

4.3.5 Corrected Mean Doses

The liver tends to lose activities, which are typically gained in the lungs. This results in mean dose correction where the absolute lower limit for the liver and absolute upper limit for the lung are both 0 Gy. Therefore, these correction biases were combined and illustrated in Fig. 4.7 through boxplots and a modified Bland Altman plot. The modified Bland Altman plots illustrates the mean bias and 95% CIs for both the liver and lung. The bias was defined as corrected mean doses subtracted from the uncorrected mean doses.

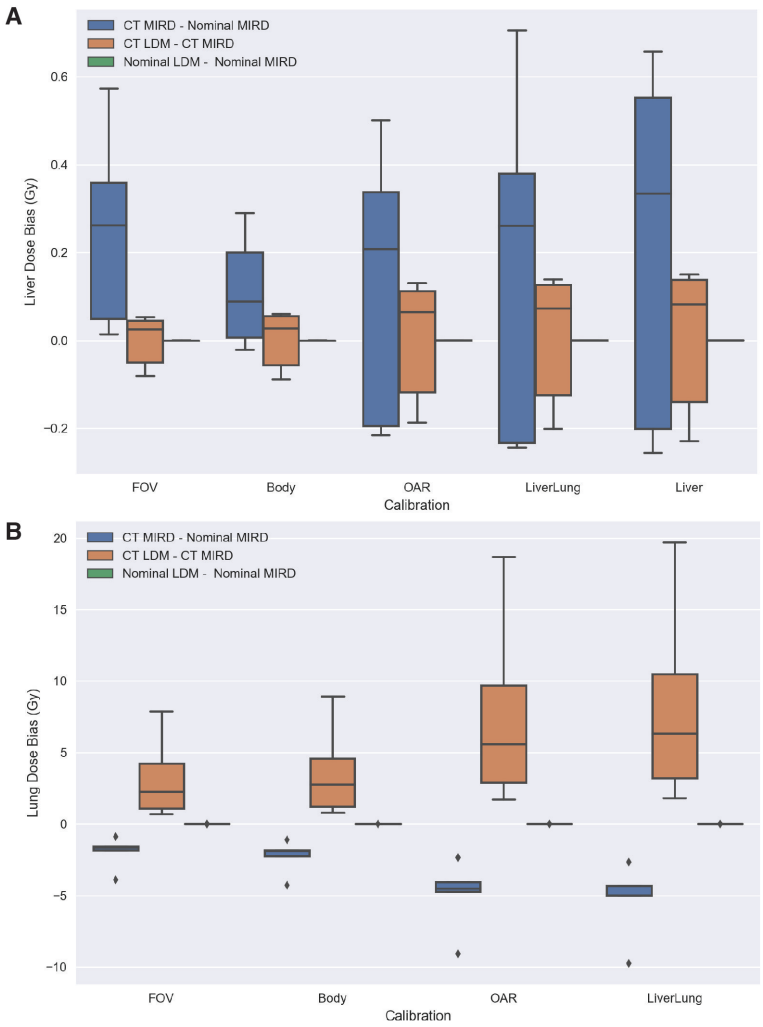

FIGURE 4.6: A boxplot of the mean dose biases between different implementations of the MIRD and local deposition methods (LDM) for the (A) liver and (B) lung. The legend summarizes the calculation performed.

As seen in Fig. 4.7a, the corrected mean doses stayed relatively consistent. On the other hand, the corrected lung doses showed a trend where smaller calibration regions lead to increasingly decreased lung dose estimates. All eight of the liver mean biases based on the liver calibration were 0 Gy. Fig. 4.7b had liver mean biases at 1.6 Gy. The liver had a 95% CI upper limit at 4.1 Gy while the lung had a 95% CI lower slope limit at -0.2 or within 20% of the mean dose lung values. Table 4.6 contains a summary of all the Bland Altman results.

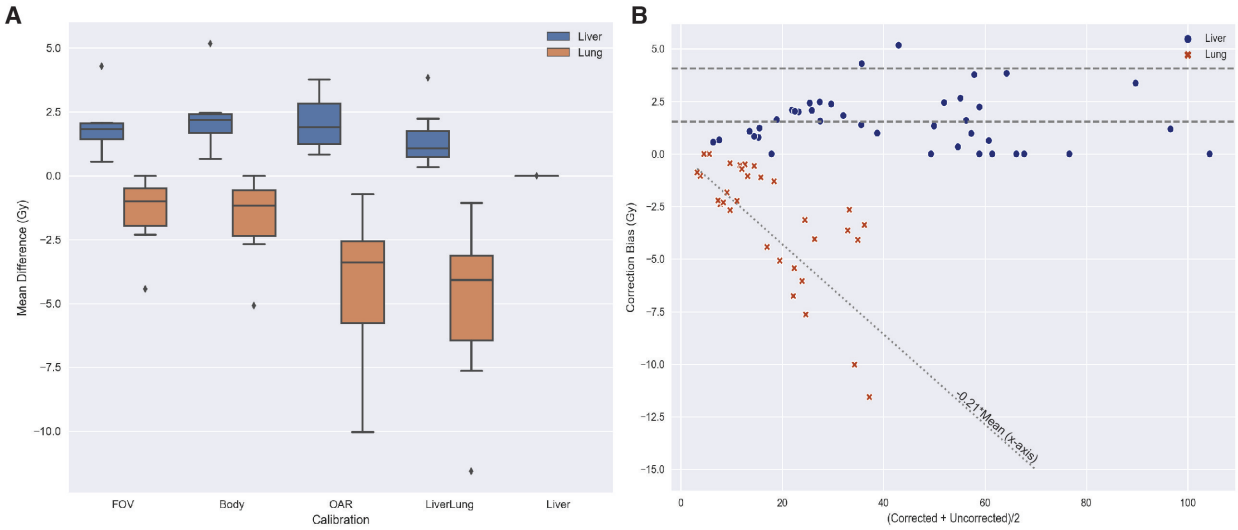

FIGURE 4.7: (A) Boxplots of corrected mean doses and (B) a modified Bland Altman plots of both the liver, $N = 40$ and lung mean corrected doses, $N = 32$. From top to bottom, the dashed lines on the Bland Altman plot represent the upper 95% CI limit and the mean bias for the liver. The dotted lines represent the 95% lower limit slope for the lungs. N represents the number of data points compared for each self-calibration for a particular organ.

4.4 Discussion

This study investigated dosimetric variables calculated with the MIRD and local deposition method. Historically, the MIRD method was implemented heuristically due to technological limitations. This assumed a uniform dose distribution over an entire organ and is known to have many limitations Kim et al., 2019b. In contrast, the local deposition method, in which information on the activity distribution within an organ is used, has been validated by different methods Mikell et al., 2015b; Pasciak and Erwin, 2009. To note, neither validation studies incorporated different self-calibrations in their methodologies. The accuracy of the combined self-calibration and voxel-based methods remains unclear.

Regardless of such uncertainties, many companies have adopted the self-calibration in conjunction with emerging voxel-based methods to develop software packages. For instance, MIM developed ^{90}Y SurePlan, which utilizes the Body calibration and the

TABLE 4.6: Summary of all Bland Altman Metrics performed within this study. Slopes are given if any plot contained log back-transformed CIs. (*) Represents the log_{10} transformed metrics

	Liver		Lung		
Fig.	Mean Bias	95% CI	Mean Bias	95% CI	Slope
Fig. 4.5a	0.177	(-0.262, 0.616)	2.097	(-7.494, 11.69)	X
Fig. 4.5b	0.169	(-0.458, 0.797)	-0.084*	(-0.229*, 0.06*)	0.330
Fig. 4.7	1.546	(0, 4.086)	-0.075*	(-0.168*, 0)	0.214

CT local deposition method Balagopal and Kappadath, 2018. Varian developed RapidSphere, which is based on the Nominal local deposition method Porter et al., 2018. Although additional studies are required to investigate the combination biases of self-calibrations and different voxel-based methodologies, empirical conclusions require phantom measurements that will not directly translate to clinical situations. Consequently, this study based on real patient data is essential for proper dosimetric interpretation and comparability. The local deposition method and its assumptions may very well be the ideal method in evaluating the variations between different dosimetric parameters. Radiation transport effects are not introduced and permits an unaltered study on dosimetric variables for ^{90}Y SPECT/CT dosimetry.

4.4.1 Self-calibrations

Many calibrations including a new OAR calibration were investigated. When comparing our results with previously reported values, our mean dose differences were much larger with a linear regression slope of $\sim$2.7 compared to their slope of $\sim$1.7 between the FOV and liver calibrations Balagopal and Kappadath, 2018. These dosimetric differences were most likely attributed to reconstruction and patient FOV differences.

With large dose differences between calibrations, a conclusion on the most appropriate self-calibration would be helpful. Definite conclusions are difficult because SPECT images contain a combination of noise, scattering, collimator errors, as well as correct count data. To accurately choose the proper self-calibration, knowledge of all ^{90}Y

spatial distributions must be known. This information requires identifying the depositions within a patient's micro-vasculature Kim et al., 2019b. Instead, we discuss the implications of each calibration rationale.

There is very likely a precision and accuracy trade-off as calibration volumes become smaller Balagopal and Kappadath, 2018. Yet, certain calibrations may be excluded due to being less than ideal. Even within a standard hepatic vasculature, microspheres commonly flow through the cystic artery and into the gallbladder. Treatment complications such as retro-grade flow, re-canalization of previously embolized coils, and missed arteries on angiographies will result in additional extrahepatic microsphere depositions Uliel et al., 2012b. Thus, the Liver calibration should not be used. In the same vein, the FOV calibration includes counts that are outside a patient's body, which strongly limits its use.

The OAR calibration seems the best compromise between accuracy and precision because it accounts for likely microsphere depositions without excluding any organs at risk. There was only a 4.6-5.4% mean dose difference (Table 4.3) between the OAR and Liverlung calibrations even after the addition of four organs. Within our patient cohort, most microsphere depositions seem to be predominately localized within the liver and lungs, which are consistent with current clinical assumptions. It is possible reconstruction errors are the culprit of the OAR calibration's differences. If due to reconstruction effects, a 5.4% underestimation is deemed clinically acceptable, but still greatly improves dosimetric precision if any significant depositions occur within any common organs at risk. However, the OAR calibration increases the bias due to operator contouring variability.

In terms of precision, the Body calibration appears to be the most precise with automatic body delineations that includes all organs within its FOV. However, its large volume becomes its main limitation by including many erroneous counts into its calibration. A recent study reported up to 50% underestimation in SPECT/CT doses with regards to more accurate ^{90}Y PET/CT doses Brosch et al., 2020. If PET/CT doses were

assumed to be close to the true dosimetric estimate, such results might indicate that background counts may cause 50% underestimation of mean dose estimates. This is similar to the percentage difference between the FOV and OAR calibration. Past clinical dosimetric results assumed the Liverlung calibration because the majority of microspheres seem to deposit within these organs. For comparability sake, dosimetry with the Liverlung calibration may be preformed. Based on this rationales, the Body, OAR and Liverlung calibrations may be used to confirm the lower, most appropriate, and upper dose estimates for voxel-based dosimetry.

4.4.2 Mass Density Differences

The SPECT/CT interpolations demonstrated near perfect correspondence to the original quantitative image regardless of its interpolation method. Minimal interpolation differences coupled with low volume differences demonstrate simple preprocessing steps are adequate for voxel-based dosimetry. Consequently, the estimated dose differences between both the MIRD and local deposition methods were found to be predominately dominated by mass density effects.

As shown in Table 4.4, the assumptions that the liver is a homogeneous organ was empirically confirmed with all dose indices within 1.4% between the CT and Nominal local deposition method. Fig. 4.5b confirmed only a mean bias of 0.18 Gy and liver dose biases were within 1.5 Gy. This indicates that all liver dose metrics are comparable regardless of its self-calibration or mass density variations. These results strongly suggest that utilizing either nominal or CT based mass density implementations lead to comparable dose estimates. On the other hand, Table 4.4 showed up to a 24% difference while Fig. 4.5 demonstrated 95% CI of the biases would be within 33% of the mean. This demonstrated that lung dose estimates between the Nominal and CT methods are highly variable.

Both Fig. 4.4 and Table 4.4 indicates lung mean doses are generally much greater for the CT method ($mean = 1.2$) while DVH show greater minimum dose estimates for the

Nominal method at the same volume coverage as the CT method ($D_{70}, D_{50}, D_{30}, D_{10} < 1.0$). These results were contradictory because greater minimum dose estimates should lead to greater mean doses. This discrepancy was found to be caused by the large distribution of lung densities within the CT method; more specifically, many voxels were identified with mass densities close to air. If any signal, however small, is interpreted as activity and converted to energy where such low density voxels are localized, these voxels would result in highly inflated absorbed doses. As seen in Fig. 4.3, these inflated dose estimates explain the rightward shift for the CT method at lower D_x volumes. In other words, the CT local deposition method's lung dose metrics, especially mean and lower volume D_x dose estimates, are sensitive to stray counts (i.e. noise, scatter, system blur) and should be interpreted with caution. The nominal mass densities may provide more consistent doses for lung dosimetry.

4.4.3 MIRD Dose Comparisons

Table 4.5 and Fig. 4.6 highlight the comparability between the MIRD and local deposition methods when image inputs are consistent: modality type, calibration, and densities. Mean dose differences between these methodologies were found to be largely attributable to differences in mass densities where more homogeneous organs provided more comparable results. Essentially following the same principles, the local deposition method applies the MIRD method's homogeneously distributed dose assumptions at a voxel level. Instead of normalizing all the accumulated energy evenly within an organ's mass, the local deposition method normalizes spatially distributed energy by voxel specific masses. Fig. 4.6 illustrates such effects when the liver's dose bias spread was smaller between the CT local deposition method and MIRD method compared to the lung's. Furthermore, equations 4.2 and 4.3 make apparent that the MIRD and local deposition methods will result in the same dose estimates when implementing nominal densities. This suggests that as long as consistent and proper quantitative reconstructions are utilized, the dose estimates from the mono-compartmental

and extended to the partition method will lead to comparable mean dose estimates to voxel-based methodologies.

4.4.4 Dosimetric Corrections

Our correction method may be used to obtain more representative mean doses for sub-optimal images when dosimetry may not otherwise be possible. In this study, the mean doses were corrected for activities in the liver that spilled over into neighboring organs. Fig. 4.7 showed that the magnitude of the mean dose corrections for the lungs were greater than the livers'. This was explained by the lung's relatively smaller fraction of activity with respect to the total included activity counts, resulting in a greater dosimetric shift with minimal correction changes. In contrast, the liver mean doses stayed relatively consistent between calibrations. This was explained by the liver's relatively large activity counts that caused only minimal dose changes when any additional misplaced activities were added.

Importantly, this correction methodology has an empirically valid basis when correcting for the liver. Studies have shown that the liver doses calculated with the local deposition method are at worst comparable and at best superior to other voxel-based methodologies Ljungberg and Sjögreen-Gleisner, 2011; Mikell et al., 2015b; Pasciak and Erwin, 2009; Pacilio et al., 2015. Our results have shown that the liver doses have minimal differences between density implementations, meaning that the correction doses will be comparable to the mean doses calculated by other voxel-based methodologies. In fact, because all liver activities have been accounted for, voxel-based dosimetry may still be performed in other organs. To note, a potential limitation exists. If all blurred activities due to patient motion or partial volume effects are accounted for, the local deposition method has the potential to overestimate the liver's mean doses Pacilio et al., 2015. However, Fig. 4.7 demonstrated that if an overestimation does occur it will likely be negligible due to the liver's relatively large activity before correction. Nonetheless,

our mean correction method will permit accurate dosimetry in other organs such as the lungs where doses were shown to be more affected by misplaced activities.

Eight mean liver doses calibrated with the Liver rationale were shown to have a mean dose bias of 0 Gy. This result highlights an important consequence of using self-calibrations; they implicitly ignore counts outside organ delineations even when attributed to patient motion and partial volume effects. For accurate dosimetry, any misplaced counts must be included during calibration because they still contribute to the relative activity distributions within an image. If not included, resulting calibrated activities would have activity distributions that are off by a dosimetric factor.

4.4.5 Limitations

Owing to the retrospective nature of this study, there were several limitations. SPECT/CT FOVs were not standardized, which resulted in patients having varying lung volume cut-offs. As with all voxel-based studies, these results were specific to one set of optimized reconstruction parameters, which limit the applicability of these results. Hermes has introduced new Monte Carlo based collimator correction, which would help with reconstruction accuracy Kim et al., 2019a. Such improved reconstructions are not commonly available. This study demonstrated a clinically more represtative and quantitative dosimetric investigation.

4.5 Conclusion

This study investigated the differences in self-calibrations, preprocessing implementations, mass density, and dosimetry between the mono-compartmental and local deposition methods. A mean correction method was also introduced. Our results indicated up to ∼270% difference between calibrations. Nominal mass densities were found to have consistent doses for the liver and be highly variable in lung doses. The mono-compartmental and local deposition method, mean doses were more comparable in

organs with homogeneous densities; in fact, mean organ doses were the same between the two methods when nominal densities were utilized. Overall, the use of local deposition method based on CT mass densities should only be used when ideal images are available. Due to ^{90}Y imaging limitations, the use of nominal mass densities for consistent and comparable dosimetric results is recommended. If patient motion effects and partial volume effects are present in the liver, our mean correction method will calculate more representative mean doses.

References

Allred, Jonathan D. et al. (June 2018b). "The value of 99mTc-MAA SPECT/CT for lung shunt estimation in 90Y radioembolization: a phantom and patient study". In: *EJNMMI Research* 8.1. DOI: 10.1186/s13550-018-0402-8.

Balagopal, A. and S. C. Kappadath (2018). "Characterization of (90) Y-SPECT/CT self-calibration approaches on the quantification of voxel-level absorbed doses following (90) Y-microsphere selective internal radiation therapy". In: *Med Phys* 45.2, pp. 875–883. DOI: 10.1002/mp.12695.

Bland, J. Martin and DouglasG. Altman (Feb. 1986). "STATISTICAL METHODS FOR ASSESSING AGREEMENT BETWEEN TWO METHODS OF CLINICAL MEASUREMENT". In: *The Lancet* 327.8476, pp. 307–310. DOI: 10.1016/s0140-6736(86)90837-8.

Bolch, W. E. et al. (1999). "MIRD Pamphlet No. 17: The dosimetry of nonuniform activity distributions radionuclide S values at the voxel level". In: *J Nucl Med* 28.40, 11S–36S.

Brosch, Julia et al. (Dec. 2020). "3D image-based dosimetry for Yttrium-90 radioembolization of hepatocellular carcinoma: Impact of imaging method on absorbed dose estimates". In: *Physica Medica* 80, pp. 317–326. DOI: 10.1016/j.ejmp.2020.11.016.

Chiesa, C. et al. (June 2015). "Radioembolization of hepatocarcinoma with 90Y glass microspheres: development of an individualized treatment planning strategy based on dosimetry and radiobiology". In: *European Journal of Nuclear Medicine and Molecular Imaging* 42.11, pp. 1718–1738. DOI: 10.1007/s00259-015-3068-8.

Dewaraja, Yuni K. et al. (Oct. 2017b). "Improved quantitative90Y bremsstrahlung SPECT/CT reconstruction with Monte Carlo scatter modeling". In: *Medical Physics* 44.12, pp. 6364–6376. DOI: 10.1002/mp.12597.

Dezarn, William A. et al. (2011b). "Recommendations of the American Association of Physicists in Medicine on dosimetry, imaging, and quality assurance procedures for 90Y microsphere brachytherapy in the treatment of hepatic malignancies". In: *Medical Physics* 38.8, pp. 4824–4845. DOI: 10.1118/1.3608909.

Dieudonne, A. et al. (2011). "Clinical Feasibility of Fast 3-Dimensional Dosimetry of the Liver for Treatment Planning of Hepatocellular Carcinoma with 90Y-Microspheres". In: *Journal of Nuclear Medicine* 52.12, pp. 1930–1937. DOI: 10.2967/jnumed.111.095232.

Elschot, Mattijs et al. (May 2014). "99mTc-MAA overestimates the absorbed dose to the lungs in radioembolization: a quantitative evaluation in patients treated with 166Ho-microspheres". In: *European Journal of Nuclear Medicine and Molecular Imaging* 41.10, pp. 1965–1975. DOI: 10.1007/s00259-014-2784-9.

Euser, Anne M., Friedo W. Dekker, and Saskia le Cessie (Oct. 2008). "A practical approach to Bland-Altman plots and variation coefficients for log transformed variables". In: *Journal of Clinical Epidemiology* 61.10, pp. 978–982. DOI: 10.1016/j.jclinepi.2007.11.003.

Favelier, S. et al. (2015). "Anatomy of liver arteries for interventional radiology". In: *Diagn Interv Imaging* 96.6, pp. 537–46. ISSN: 2211-5684 (Electronic) 2211-5684 (Linking). DOI: 10.1016/j.diii.2013.12.001.

Jabbour, S. K. et al. (2014). "Upper abdominal normal organ contouring guidelines and atlas: a Radiation Therapy Oncology Group consensus". In: *Pract Radiat Oncol* 4.2, pp. 82–89. ISSN: 1879-8519 (Electronic) 1879-8500 (Linking). DOI: 10.1016/j.prro.2013.06.004.

Jong, H.W.A.M. de, E.T.P. Slijpen, and F.J. Beekman (2001). "Acceleration of Monte Carlo SPECT simulation using convolution-based forced detection". In: *IEEE Transactions on Nuclear Science* 48.1, pp. 58–64. DOI: 10.1109/23.910833.

Kao, Y. H. et al. (2013c). "Post-radioembolization yttrium-90 PET/CT - part 2: dose-response and tumor predictive dosimetry for resin microspheres". In: *EJNMMI Res* 3.1, p. 57. ISSN: 2191-219X (Print). DOI: 10.1186/2191-219X-3-57.

Kappadath, S. Cheenu et al. (2018b). "Hepatocellular Carcinoma Tumor Dose Response After 90Y-radioembolization With Glass Microspheres Using 90Y-SPECT/CT-Based Voxel Dosimetry". In: *Int J Radiat Oncol Biol Phys* 102.2, pp. 451–461. DOI: 10.1016/j.ijrobp.2018.05.062.

Kim, Minho et al. (2019a). "Effects of collimator on imaging performance of Yttrium-90 Bremsstrahlung photons: Monte Carlo simulation". In: *Nuclear Engineering and Technology* 51.2, pp. 539–545. DOI: 10.1016/j.net.2018.11.007.

Kim, S. P. et al. (2019b). "A guide to (90)Y radioembolization and its dosimetry". In: *Phys Med* 68, pp. 132–145. ISSN: 1724-191X (Electronic) 1120-1797 (Linking). DOI: 10.1016/j.ejmp.2019.09.236.

Ljungberg, Michael and Katarina Sjögreen-Gleisner (2011). "The accuracy of absorbed dose estimates in tumours determined by Quantitative SPECT: A Monte Carlo study". In: *Acta Oncologica* 50.6, pp. 981–989. DOI: 10.3109/0284186x.2011.584559.

Mikell, J. K. et al. (2015b). "Comparing voxel-based absorbed dosimetry methods in tumors, liver, lung, and at the liver-lung interface for (90)Y microsphere selective internal radiation therapy". In: *EJNMMI Phys* 2.1, p. 16. ISSN: 2197-7364 (Print) 2197-7364 (Linking). DOI: 10.1186/s40658-015-0119-y.

Pacilio, Massimiliano et al. (2015). "Differences in 3D dose distributions due to calculation method of voxel S-values and the influence of image blurring in SPECT". In: *Physics in Medicine and Biology* 60.5, pp. 1945–1964. DOI: 10.1088/0031-9155/60/5/1945.

Pasciak, A. S., A. C. Bourgeois, and Y. C. Bradley (2014). "A Comparison of Techniques for (90)Y PET/CT Image-Based Dosimetry Following Radioembolization with Resin Microspheres". In: *Front Oncol* 4, p. 121. ISSN: 2234-943X (Print) 2234-943X (Linking). DOI: 10.3389/fonc.2014.00121.

Pasciak, A. S. and W. D. Erwin (2009). "Effect of voxel size and computation method on Tc-99m MAA SPECT/CT-based dose estimation for Y-90 microsphere therapy". In: *IEEE Trans Med Imaging* 28.11, pp. 1754–8. ISSN: 1558-254X (Electronic) 0278-0062 (Linking). DOI: 10.1109/TMI.2009.2022753.

Porter, Charlotte A. et al. (2018). "Phantom and clinical evaluation of the effect of full Monte Carlo collimator modelling in post-SIRT yttrium-90 Bremsstrahlung SPECT imaging". In: *EJNMMI Research* 8.1. DOI: 10.1186/s13550-018-0361-0.

Potrebko, Peter S. et al. (2018). "SPECT/CT image-based dosimetry for Yttrium-90 radionuclide therapy: Application to treatment response". In: *Journal of Applied Clinical Medical Physics* 19.5, pp. 435–443. ISSN: 2473-4209 (Electronic) 0094-2405 (Linking). DOI: 10.1002/acm2.12400.

Siman, W., J. K. Mikell, and S. C. Kappadath (2016a). "Practical reconstruction protocol for quantitative (90)Y bremsstrahlung SPECT/CT". In: *Med Phys* 43.9, p. 5093. ISSN: 2473-4209 (Electronic) 0094-2405 (Linking). DOI: 10.1118/1.4960629.

Uliel, L. et al. (2012b). "From the angio suite to the gamma-camera: vascular mapping and 99mTc-MAA hepatic perfusion imaging before liver radioembolization–a comprehensive pictorial review". In: *J Nucl Med* 53.11, pp. 1736–47. ISSN: 1535-5667 (Electronic) 0161-5505 (Linking). DOI: 10.2967/jnumed.112.105361.

White, D. R., R. V. Griffith, and I. J. Wilson (1992). "Report 46". In: *Journal of the International Commission on Radiation Units and Measurements* os24.1, NP–NP. DOI: 10.1093/jicru/os24.1.report46.

Chapter 5

Discussion & Conclusion

^{90}Y radioembolization lies in an interesting research position. Although its dosimetry has access to advanced methods such as Monte Carlo simulations, the bottleneck lies not in the method of calculation itself, but rather the inputted data. The accuracy and precision of the reconstructed images used in dosimetry become the main limiting factor to accurate dosimetry.

Image-based, voxel-based dosimetry is affected by any image processing that may occur. Whether manipulating the initial acquisition, the pre-processing, or the final dosimetry methodology, any errors produced before and during dosimetry calculation will be propagated into the final dosimetric map. Radioembolization dosimetry requires careful analysis that maximizes accuracy while taking into consideration practical limitations.

5.1 Preprocessing Biases

Often neglected in the discussion, pre-processing must first occur before dosimetry may even begin. Common pre-processing steps include registering images acquired from two imaging modalities together such as SPECT and CT, interpolations, and converting CT units to mass densities for dosimetry. Due to the dual nature of SPECT/CT

and PET/CT, certain methodologies may require registering an independent CT image to a SPECT image. It is assumed that these image manipulation errors are negligible, but there is likely a bias that will be introduced and such quantitative effects should somehow be quantified. Another possibility, an MRI image may be registered to SPECT, or more likely to PET. Specific for MRI registered images, attenuation coefficients must be first derived for the MRI. Such pre-processing steps introduces additional sources of error into the final dosimetric image, especially if these derived attenuation coefficients are then used for PET reconstruction. For such methodologies, it is best to dosimetrically quantify such methodologies accuracies before use or refrain from utilizing such a methodology.

Luckily, many SPECT and PET systems are pre-registered with a CT, resulting in a common global coordinate system that eliminates most, if not all registration concerns. Unfortunately, even with the same common global coordinate systems, SPECT and PET still have voxel sizes and FOVs that differ to the CT's. This is because CT is a fairly robust and quantitative imaging modality that has superior resolution resulting in smaller possible voxel sizes compared to SPECT or PET. In most cases, interpolations are required so that voxel volumes may be equated and dosimetry may be performed. There is currently no consensus nor much investigation into these issues. Table 4.2 in our second study show that interpolation errors are negligible when CT and SPECT images are already registered.

The conversion from CT houndsfield units to mass density values are another pre-processing step for dosimetry. Within our studies, density values were scanned from the same SPECT/CT system that obtained the patient images. Different material inserts with known mass densities were used as references to convert attenuation coefficients to density values. Typically, a simple linear interpolation is utilized to convert a CT's Houndsfield unit to density values. It may be theoretically ideal to include more inserts to aid in more precise and accurate density interpolations. However, our second study demonstrated that density conversions may not even be necessary for

dosimetry. Reconstructed SPECT images utilizing the CT method have a tendency to inflate mean lung doses, but liver doses are still within 1.5%. Thus, nominal densities seem reasonable as a simplification step for radioembolization dosimetry. Nonetheless, these conclusions are stated with the expectation that as SPECT reconstructions become more accurate and precise, these simplified assumptions are revisited.

5.2 Standardizing ^{90}Y Dosimetry

Within radioembolization dosimetry, there are many sources of variability in every aspect of its treatment step. The imaging modalities, imaging parameters, the reconstruction algorithms utilized, even dosimetric methods, as the second manuscript has highlighted, have implementation differences within even a single institution. Assuming constant imaging modality and reconstruction parameters, SPECT blurs spatial activity localizations, thus decreasing the quantification accuracy of the original patient's source distributions. The purpose of SPECT is to locate the the initial distribution of microspheres that contain ^{90}Y. If an accurate initial distribution is found, radiation transport may then be simulated from the resulting ^{90}Y images. Unfortunately, this is currently not the case. The most important question becomes how reconstructed images in conjunction with a dosimetric methodology differs in dose estimates from the true solution.

Aforementioned, the consensus within the literature seems to be that the local deposition method is the most ideal voxel-based methodology. Based on past studies, Monte Carlo has been said to fall in accuracies compared to the simpler local deposition method (Pasciak and Erwin, 2009). A potential limitation, however, this study utilized a phantom image that was post-reconstruction filtered. This filtering or additional blurring likely affected their results. In another more theoretical study, investigations in image blurring effects on dosimetry were performed for SPECT (Pacilio et al., 2015). Similarly, this study revealed that the local deposition performed with superior or comparable accuracies at a FWHM of around 4 mm and higher. However, S-value

convolutions were utilized as the benchmark reference instead of Monte Carlo simulations and a simple Gaussian blurring was utilized for system response modeling. Although adequate for PET, Gaussian blurring is likely an inadequate system response model for SPECT/CT (Pasciak, Bourgeois, and Bradley, 2014). Due to the limitations described and the heterogeneity between studies, additional studies are required to more robustly demonstrate the most ideal methodology.

5.3 Geant4 and reDoseMC

There are multiple Monte Carlo simulation toolkits (EGSnrc, SIMIND, MCNP) available for radiation transport simulations. Geant4 is a toolkit developed by CERN that has the most flexibility. It requires taking the various tool package outlines and creating an application specific Monte Carlo simulation. Although unused in this project, a Monte Carlo dosimetry package specific for voxel-based dosimetry was developed with Geant4. Called reDoseMC, this Monte Carlo package permits $3D$ patient or phantom-based dosimetry. It is multi-threaded, may take in CT with either PET or SPECT images, may produce particle spectrums, and has uncertainty estimations based on the history-by-history methodology (Walters, Kawrakow, and Rogers, 2002). reDoseMC has specific advantages to other Monte Carlo methods by allowing any errors associated with interpolations to be solved. As long as the global coordinate system is the same i.e. registered SPECT/CT inputs are obtained, interpolation methods between SPECT and CT are not required. Instead, sources and their corresponding volumes and worlds may be combined together in parallel.

Monte Carlo simulations are not exempt from the aforementioned imaging limitations. Currently, all patient based Monte Carlo simulations including reDoseMC are questionable in their benchmarking validity. That being said, certain considerations must still be addressed when the eventual use of Monte Carlo methods occurs for

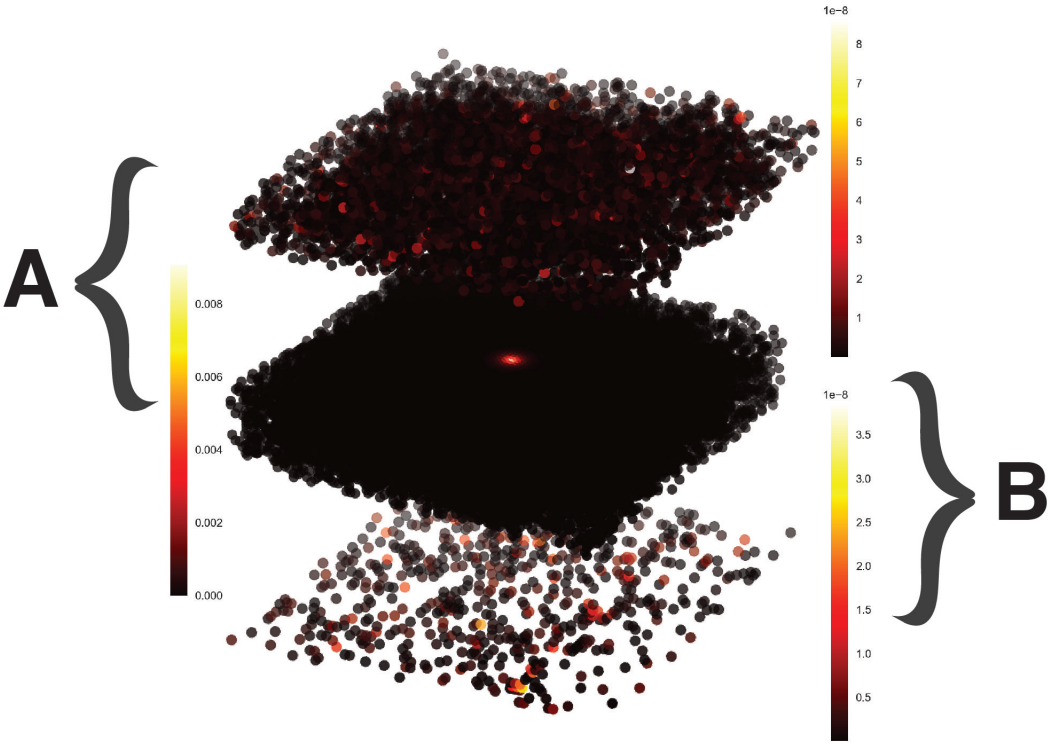

FIGURE 5.1: A 3*D* deconstructed S-value kernel at z-slices of 1, 21-40, and 71-81 are illustrated. These slices illustrate the Gy/particle per voxel for a 81x81x81 liver kernel. The space between A) slices 40 to 81 and B) 1 to 21 were not illustrated for visualization purposes.

SPECT/CT dosimetry. A potential issue, there have been several Monte Carlo simulations published with source creation based on sampling SPECT or PET activity distributions (Marcatili et al., 2013; Amato et al., 2020). Although adequate in simulations with a few sources voxels, SPECT and PET have activity maps that may contain millions of source voxels. If it is assumed that SPECT represents the true dosimetric distribution, then the exact SPECT activity distribution should be simulated. Yet, there is no guarantee that the same activity distributions will be simulated when sampling SPECT activity distributions, even if 1 billion sources are sampled. In fact, the sheer number of sources will likely produce erroneous source distribution or type A uncertainties that will affect the final simulation results. To solve this issue, reDoseMC places activity sources sequentially in the exact ratios as SPECT or PET activity distributions. This implementation has no additional computational cost while lying true to original SPECT source data.

reDoseMC has the additional capacity to create dose-point or S-value kernels. Within the field, there has been much discussion with regards to dose-point kernel methodologies, especially pertaining to S-values methodologies. Some studies argue that S-value methodologies may be used for a benchmarking reference (Pacilio et al., 2015; Siman et al., 2020). The most common S-values utilized for benchmarking are calculated for a specific volume world and were only simulated with 25 million particles (Lanconelli et al., 2012). Fig. 5.1 illustrates a similar kernel simulated with reDoseMC with 25 million primary particles simulated in a liver kernel of 81x81x81 mms. It can be seen that the majority of the dose is localized within or near the center voxel. However, each dot represents dose deposited. It can be seen dose will deposit outside its mean β^- particle length due to bremsstralung photons and its indirect energy depositions.

Many implementation questions also arose when creating such kernels. What are the acceptable energy thresholds for particles, especially concerning the created bremsstralung photons? Should we ignore any high uncertainty dose depositions? How large should the world volume simulation be for S-value creations? Finally, how many particles should we simulate? These issues are mainly predicated by the fact that ^{90}Y has both direct and indirect dose depositions. Bremmstralung photons create high uncertainty simulations due to their unpredictable transport patterns and β^- particle dependent production quantities.

Most interestingly, there is no consensus nor clear information on how S-values are created from a $3D$ kernel (Bolch et al., 1999). These additional dosimetric variables are added to the already large number of implementation uncertainties. It becomes clear that if S-value type methodologies are to be used, it must be standardized. However, its advantages seem limited nor its validity robust for ^{90}Y dosimetry.

5.4 Conclusions: A Practical Recommendation

The American Association of Physicists in Medicine (AAPM) is a professional group that creates policy guidelines for hospitals focused typically within America, but with recommendations that have an international impact. AAPM has created (TG-356) and is in the process of creating Task Groups (TG-144) to address some of the uncertainties associated with radioembolization's dosimetry. Their mandate starts with recommending the ideal practices for ^{90}Y dosimetry with the hopes of eventual standardization. Our second manuscript carefully navigated many dosimetric issues while attempting to provide results that will help with dose comparisons and analysis. With clinical implementations already underway, it is clear the local deposition method will be the primary dosimetric method utilized within clinical institutions. If so, a standardization will be required for consistent imaging and dosimetry parameters. In this regard, some recommendations are suggested.

First and foremost, a count-to-activity calibration methodology must be standardized for radioembolization. Traditionally, an activity conversion is empirically found by imaging a point source in air and using the the same reconstruction parameters in the phantom and patient images (*Nuclear Medicine Physics* 2015). However, such a conversion does not take into account patient-specific scatter effects. This methodology becomes limited because ^{90}Y requires detection of bremsstralung photons, which requires the exact patient dimensions and material compositions. The self-calibration then becomes the only choice of count-to-activity calibration method. A methodology is then proposed. First, the calibration assumption should start by assuming that all counts are contained within the liver and lungs. Based on this assumption, the international radiologist and nuclear medicine physician should then discuss any microsphere depositions outside such ROI. For instance, a bi-lobar treatment could include any organs where any large extra-hepatic arteries were connected in the patient. If such a methodology is not logistically possible, then the OAR calibration should be implemented as a calibration that includes all the likely organs for microsphere deposition,

but with negligible accuracy limitations.

In terms of the dosimetry, the local deposition method implemented with nominal densities should be utilized. This conclusion is precluded by several reasons. The resolution blurring of SPECT and PET will likely introduce many biases for voxel level analysis such as in DVHs. This effect will likely be compounded by radiation transport effects. On the other hand, mean dose estimates will be more resistant to scanner biases if all activities are included in its calculation and complete self-voxel irradiation is assumed. Although the mean doses calculated by the local deposition method may overestimate the doses within patients, the local deposition method implementing nominal densities will provide consistent dose estimates between implementation differences. This permits comparability to past dosimetric methodologies such as the mono-compartmental and partition methods where the mean doses between such methodologies may be exact. Having dosimetric endpoints such as the mean doses that are comparable will make for more comparable analysis where all methodologies will have errors of the same basis. When images become accurate enough to calculate proper patient doses, previously calculated mean dose estimates may then be retrospectively compared to validated Monte Carlo simulations for bias analysis.

Bibliography

Ahmadzadehfar, Hojjat et al. (Oct. 2015). "Evaluation of the delivered activity of yttrium-90 resin microspheres using sterile water and 5 % glucose during administration". In: *EJNMMI Research* 5.1.

Allred, J. D. et al. (2018a). "The value of (99m)Tc-MAA SPECT/CT for lung shunt estimation in (90)Y radioembolization: a phantom and patient study". In: *EJNMMI Res* 8.1, p. 50. ISSN: 2191-219X (Print). DOI: 10.1186/s13550-018-0402-8.

Allred, Jonathan D. et al. (June 2018b). "The value of 99mTc-MAA SPECT/CT for lung shunt estimation in 90Y radioembolization: a phantom and patient study". In: *EJNMMI Research* 8.1. DOI: 10.1186/s13550-018-0402-8.

Amato, Ernesto et al. (June 2020). "Full Monte Carlo internal dosimetry in nuclear medicine by means of GAMOS". In: *Journal of Physics: Conference Series* 1561, p. 012002. DOI: 10.1088/1742-6596/1561/1/012002.

Bailey, D. L. and K. P. Willowson (2014). "Quantitative SPECT/CT: SPECT joins PET as a quantitative imaging modality". In: *Eur J Nucl Med Mol Imaging* 41 Suppl 1, S17–25. ISSN: 1619-7089 (Electronic), 1619-7070 (Linking).

Balagopal, A. and S. C. Kappadath (2018). "Characterization of (90) Y-SPECT/CT self-calibration approaches on the quantification of voxel-level absorbed doses following (90) Y-microsphere selective internal radiation therapy". In: *Med Phys* 45.2, pp. 875–883. DOI: 10.1002/mp.12695.

Barentsz, M. W. et al. (2011). "Technical solutions to ensure safe yttrium-90 radioembolization in patients with initial extrahepatic deposition of (99m)technetium-albumin macroaggregates". In: *Cardiovasc Intervent Radiol* 34.5, pp. 1074–9. DOI: 10.1007/s00270-010-0088-4.

Bierman, H. R. et al. (1951). "Studies on the blood supply of tumors in man. III. Vascular patterns of the liver by hepatic arteriography in vivo". In: *J Natl Cancer Inst* 12.1, pp. 107–31. ISSN: 0027-8874 (Print), 0027-8874 (Linking).

Bland, J. Martin and DouglasG. Altman (Feb. 1986). "STATISTICAL METHODS FOR ASSESSING AGREEMENT BETWEEN TWO METHODS OF CLINICAL MEASUREMENT". In: *The Lancet* 327.8476, pp. 307–310. DOI: 10.1016/s0140-6736(86)90837-8.

Bolch, W. E. et al. (1999). "MIRD Pamphlet No. 17: The dosimetry of nonuniform activity distributions radionuclide S values at the voxel level". In: *J Nucl Med* 28.40, 11S–36S.

Braat, A. J. et al. (2015). "(9)(0)Y Hepatic Radioembolization: An Update on Current Practice and Recent Developments". In: *J Nucl Med* 56.7, pp. 1079–87. ISSN: 1535-5667 (Electronic), 0161-5505 (Linking). DOI: 10.2967/jnumed.115.157446.

Brosch, Julia et al. (Dec. 2020). "3D image-based dosimetry for Yttrium-90 radioembolization of hepatocellular carcinoma: Impact of imaging method on absorbed dose estimates". In: *Physica Medica* 80, pp. 317–326. DOI: 10.1016/j.ejmp.2020.11.016.

Campbell, A. M., I. H. Bailey, and M. A. Burton (2000). "Analysis of the distribution of intra-arterial microspheres in human liver following hepatic yttrium-90 microsphere therapy". In: *Phys Med Biol* 45.4, pp. 1023–33. ISSN: 0031-9155 (Print), 0031-9155 (Linking).

– (2001). "Tumour dosimetry in human liver following hepatic yttrium-90 microsphere therapy". In: *Phys Med Biol* 46.2, pp. 487–98. ISSN: 0031-9155 (Print), 0031-9155 (Linking).

Chan, Keith T. et al. (June 2018). "Prospective Trial Using Internal Pair-Production Positron Emission Tomography to Establish the Yttrium-90 Radioembolization Dose Required for Response of Hepatocellular Carcinoma". In: *International Journal of Radiation Oncology∗Biology∗Physics* 101.2, pp. 358–365.

Chiesa, C. et al. (June 2015). "Radioembolization of hepatocarcinoma with 90Y glass microspheres: development of an individualized treatment planning strategy based on dosimetry and radiobiology". In: *European Journal of Nuclear Medicine and Molecular Imaging* 42.11, pp. 1718–1738. DOI: 10.1007/s00259-015-3068-8.

Coldwell, Douglas et al. (June 2011). "General Selection Criteria of Patients for Radioembolization of Liver Tumors". In: *American Journal of Clinical Oncology* 34.3, pp. 337–341.

Cremonesi, Marta et al. (Aug. 2014). "Radioembolization of Hepatic Lesions from a Radiobiology and Dosimetric Perspective". In: *Frontiers in Oncology* 4.

D'Arienzo, M. et al. (2012). "90Y PET-based dosimetry after selective internal radiotherapy treatments". In: *Nucl Med Commun* 33.6, pp. 633–40. ISSN: 1473-5628 (Electronic), 0143-3636 (Linking).

D'Arienzo, M. et al. (2013). "Absorbed dose to lesion and clinical outcome after liver radioembolization with 90Y microspheres: a case report of PET-based dosimetry". In: *Ann Nucl Med* 27.7, pp. 676–80. ISSN: 1864-6433 (Electronic), 0914-7187 (Linking).

Dewaraja, Y. K. et al. (2017a). "Improved quantitative (90) Y bremsstrahlung SPECT/CT reconstruction with Monte Carlo scatter modeling". In: *Med Phys* 44.12, pp. 6364–6376. ISSN: 2473-4209 (Electronic), 0094-2405 (Linking).

Dewaraja, Yuni K. et al. (Oct. 2017b). "Improved quantitative90Y bremsstrahlung SPECT/CT reconstruction with Monte Carlo scatter modeling". In: *Medical Physics* 44.12, pp. 6364–6376. DOI: 10.1002/mp.12597.

Dezarn, William A. et al. (Aug. 2011a). "Recommendations of the American Association of Physicists in Medicine on dosimetry, imaging, and quality assurance procedures for 90 Y microsphere brachytherapy in the treatment of hepatic malignancies". In: *Medical Physics* 38.8, pp. 4824–4845.

– (2011b). "Recommendations of the American Association of Physicists in Medicine on dosimetry, imaging, and quality assurance procedures for 90Y microsphere brachytherapy in the treatment of hepatic malignancies". In: *Medical Physics* 38.8, pp. 4824–4845. DOI: 10.1118/1.3608909.

Dieudonne, A. et al. (2011). "Clinical Feasibility of Fast 3-Dimensional Dosimetry of the Liver for Treatment Planning of Hepatocellular Carcinoma with 90Y-Microspheres". In: *Journal of Nuclear Medicine* 52.12, pp. 1930–1937. DOI: 10.2967/jnumed.111.095232.

Edeline, Julien et al. (Jan. 2020). "Radioembolization Plus Chemotherapy for First-line Treatment of Locally Advanced Intrahepatic Cholangiocarcinoma". In: *JAMA Oncology* 6.1, p. 51. DOI: 10.1001/jamaoncol.2019.3702.

Elschot, M. et al. (2013a). "Quantitative comparison of PET and Bremsstrahlung SPECT for imaging the in vivo yttrium-90 microsphere distribution after liver radioembolization". In: *PLoS One* 8.2, e55742. ISSN: 1932-6203 (Electronic), 1932-6203 (Linking).

Elschot, M. et al. (2013b). "Quantitative Monte Carlo-based 90Y SPECT reconstruction". In: *J Nucl Med* 54.9, pp. 1557–63. ISSN: 1535-5667 (Electronic), 0161-5505 (Linking).

Elschot, Mattijs et al. (May 2014). "99mTc-MAA overestimates the absorbed dose to the lungs in radioembolization: a quantitative evaluation in patients treated with 166Ho-microspheres". In: *European Journal of Nuclear Medicine and Molecular Imaging* 41.10, pp. 1965–1975. DOI: 10.1007/s00259-014-2784-9.

Erdi, Alev K. et al. (Oct. 1998). "Use of the fast Hartley transform for three-dimensional dose calculation in radionuclide therapy". In: *Medical Physics* 25.11, pp. 2226–2233. DOI: 10.1118/1.598422.

Euser, Anne M., Friedo W. Dekker, and Saskia le Cessie (Oct. 2008). "A practical approach to Bland-Altman plots and variation coefficients for log transformed variables". In: *Journal of Clinical Epidemiology* 61.10, pp. 978–982. DOI: 10.1016/j.jclinepi.2007.11.003.

Favelier, S. et al. (2015). "Anatomy of liver arteries for interventional radiology". In: *Diagn Interv Imaging* 96.6, pp. 537–46. ISSN: 2211-5684 (Electronic) 2211-5684 (Linking). DOI: 10.1016/j.diii.2013.12.001.

Fournier, L. et al. (2014). "Imaging criteria for assessing tumour response: RECIST, mRECIST, Cheson". In: *Diagn Interv Imaging* 95.7-8, pp. 689–703. ISSN: 2211-5684 (Electronic), 2211-5684 (Linking).

Fox, R. A. et al. (1991). "Dose distribution following selective internal radiation therapy". In: *Int J Radiat Oncol Biol Phys* 21.2, pp. 463–7. ISSN: 0360-3016 (Print), 0360-3016 (Linking).

Gallio, E. et al. (2016). "Calculation of tumour and normal tissue biological effective dose in (90)Y liver radioembolization with different dosimetric methods". In: *Phys Med* 32.12, pp. 1738–1744. ISSN: 1724-191X (Electronic), 1120-1797 (Linking).

Garin, E. et al. (2012). "Dosimetry based on 99mTc-macroaggregated albumin SPECT/CT accurately predicts tumor response and survival in hepatocellular carcinoma patients treated with 90Y-loaded glass microspheres: preliminary results". In: *J Nucl Med* 53.2, pp. 255–63. ISSN: 1535-5667 (Electronic), 0161-5505 (Linking).

Gates, V. L. et al. (2011). "Internal pair production of 90Y permits hepatic localization of microspheres using routine PET: proof of concept". In: *J Nucl Med* 52.1, pp. 72–6. ISSN: 1535-5667 (Electronic), 0161-5505 (Linking).

Germain, T. et al. (2014). "Liver segmentation: practical tips". In: *Diagn Interv Imaging* 95.11, pp. 1003–16. DOI: 10.1016/j.diii.2013.11.004.

Giammarile, Francesco et al. (Apr. 2011). "EANM procedure guideline for the treatment of liver cancer and liver metastases with intra-arterial radioactive compounds". In: *European Journal of Nuclear Medicine and Molecular Imaging* 38.7, pp. 1393–1406.

Gnesin, S. et al. (2016). "Partition Model-Based 99mTc-MAA SPECT/CT Predictive Dosimetry Compared with 90Y TOF PET/CT Posttreatment Dosimetry in Radioembolization of Hepatocellular Carcinoma: A Quantitative Agreement Comparison". In: *J Nucl Med* 57.11, pp. 1672–1678. ISSN: 1535-5667 (Electronic), 0161-5505 (Linking).

Grosser, O. S. et al. (2015). "Intrahepatic Activity Distribution in Radioembolization with Yttrium-90-Labeled Resin Microspheres Using the Body Surface Area Method–A Less than Perfect Model". In: *J Vasc Interv Radiol* 26.11, pp. 1615–21. ISSN: 1535-7732 (Electronic), 1051-0443 (Linking). DOI: 10.1016/j.jvir.2015.07.021.

Gulec, S. A., G. Mesoloras, and M. Stabin (2006). "Dosimetric techniques in 90Y-microsphere therapy of liver cancer: The MIRD equations for dose calculations". In: *J Nucl Med* 47.7, pp. 1209–11.

Gulec, S. A. et al. (2010). "Hepatic structural dosimetry in (90)Y microsphere treatment: a Monte Carlo modeling approach based on lobular microanatomy". In: *J Nucl Med* 51.2, pp. 301–10. ISSN: 1535-5667 (Electronic), 0161-5505 (Linking).

Hamami, M. E. et al. (2009). "SPECT/CT with 99mTc-MAA in radioembolization with 90Y microspheres in patients with hepatocellular cancer". In: *J Nucl Med* 50.5, pp. 688–92. DOI: 10.2967/jnumed.108.058347.

Hanahan, Douglas and Robert A. Weinberg (Mar. 2011). "Hallmarks of Cancer: The Next Generation". In: *Cell* 144.5, pp. 646–674.

Heard, S. et al. (2003). "Monte Carlo Simulation of 90Y Bremsstrahlung Imaging". In: *IEEE*. DOI: 10.1109/nssmic.2004.1466658.

Ho, S. et al. (1996). "Partition model for estimating radiation doses from yttrium-90 microspheres in treating hepatic tumours". In: *Eur J Nucl Med* 23.8, pp. 947–52. ISSN: 0340-6997 (Print), 0340-6997 (Linking).

Ho, S. et al. (1997). "Clinical evaluation of the partition model for estimating radiation doses from yttrium-90 microspheres in the treatment of hepatic cancer". In: *Eur J Nucl Med* 24.3, pp. 293–8.

Hogberg, J. et al. (2014). "Heterogeneity of microsphere distribution in resected liver and tumour tissue following selective intrahepatic radiotherapy". In: *EJNMMI Res* 4.1, p. 48. ISSN: 2191-219X (Print).

– (2015). "Increased absorbed liver dose in Selective Internal Radiation Therapy (SIRT) correlates with increased sphere-cluster frequency and absorbed dose inhomogeneity". In: *EJNMMI Phys* 2.1, p. 10. ISSN: 2197-7364 (Print), 2197-7364 (Linking).

Hoven, Andor F. van den et al. (Jan. 2014). "Identifying Aberrant Hepatic Arteries Prior to Intra-arterial Radioembolization". In: *CardioVascular and Interventional Radiology* 37.6, pp. 1482–1493.

Hudson, H. M. and R. S. Larkin (1994). "Accelerated image reconstruction using ordered subsets of projection data". In: *IEEE Transactions on Medical Imaging* 13.4, pp. 601–609. DOI: 10.1109/42.363108.

J, O' Doherty (2015). "A review of 3D image-based dosimetry, technical considerations and emerging perspectives in (90)Y microsphere therapy". In: *J Diagn Imaging Ther* 2.2, pp. 1–34. ISSN: 2057-3782 (Print), 2057-3782 (Linking).

Jabbour, S. K. et al. (2014). "Upper abdominal normal organ contouring guidelines and atlas: a Radiation Therapy Oncology Group consensus". In: *Pract Radiat Oncol* 4.2, pp. 82–89. ISSN: 1879-8519 (Electronic) 1879-8500 (Linking). DOI: 10.1016/j.prro.2013.06.004.

Jong, H.W.A.M. de, E.T.P. Slijpen, and F.J. Beekman (2001). "Acceleration of Monte Carlo SPECT simulation using convolution-based forced detection". In: *IEEE Transactions on Nuclear Science* 48.1, pp. 58–64. DOI: 10.1109/23.910833.

Kao, Y. H. (2013). "Results confounded by a disregard for basic dose-response radiobiology". In: *J Nucl Med* 54.9, pp. 1682–3. ISSN: 1535-5667 (Electronic), 0161-5505 (Linking).

Kao, Y. H. et al. (2011). "Clinical implications of the body surface area method versus partition model dosimetry for yttrium-90 radioembolization using resin microspheres: a technical review". In: *Ann Nucl Med* 25.7, pp. 455–61. ISSN: 1864-6433 (Electronic), 0914-7187 (Linking). DOI: 10.1007/s12149-011-0499-6.

Kao, Y. H. et al. (2012). "Image-guided personalized predictive dosimetry by artery-specific SPECT/CT partition modeling for safe and effective 90Y radioembolization". In: *J Nucl Med* 53.4, pp. 559–66. ISSN: 1535-5667 (Electronic), 0161-5505 (Linking). DOI: 10.2967/jnumed.111.097469.

Kao, Y. H. et al. (2013a). "Post-radioembolization yttrium-90 PET/CT - part 1: diagnostic reporting". In: *EJNMMI Res* 3.1, p. 56. ISSN: 2191-219X (Print).

Kao, Y. H. et al. (2013b). "Post-radioembolization yttrium-90 PET/CT - part 2: dose-response and tumor predictive dosimetry for resin microspheres". In: *EJNMMI Res* 3.1, p. 57. ISSN: 2191-219X (Print).

– (2013c). "Post-radioembolization yttrium-90 PET/CT - part 2: dose-response and tumor predictive dosimetry for resin microspheres". In: *EJNMMI Res* 3.1, p. 57. ISSN: 2191-219X (Print). DOI: 10.1186/2191-219X-3-57.

Kao, Yung Hsiang et al. (June 2014). "Personalized predictive lung dosimetry by technetium-99m macroaggregated albumin SPECT/CT for yttrium-90 radioembolization". In: *EJNMMI Research* 4.1.

Kappadath, S. Cheenu et al. (Oct. 2018a). "Hepatocellular Carcinoma Tumor Dose Response After 90Y-radioembolization With Glass Microspheres Using 90Y-SPECT/CT-Based Voxel Dosimetry". In: *International Journal of Radiation Oncology∗Biology∗Physics* 102.2, pp. 451–461.

– (2018b). "Hepatocellular Carcinoma Tumor Dose Response After 90Y-radioembolization With Glass Microspheres Using 90Y-SPECT/CT-Based Voxel Dosimetry". In: *Int J Radiat Oncol Biol Phys* 102.2, pp. 451–461. DOI: 10.1016/j.ijrobp.2018.05.062.

Kennedy, A. (2014). "Radioembolization of hepatic tumors". In: *J Gastrointest Oncol* 5.3, pp. 178–89. ISSN: 2078-6891 (Print), 2078-6891 (Linking).

Kennedy, Andrew et al. (May 2007). "Recommendations for Radioembolization of Hepatic Malignancies Using Yttrium-90 Microsphere Brachytherapy: A Consensus Panel Report from the Radioembolization Brachytherapy Oncology Consortium". In: *International Journal of Radiation Oncology∗Biology∗Physics* 68.1, pp. 13–23.

Kennedy, Andrew S. et al. (Dec. 2004). "Pathologic response and microdosimetry of 90Y microspheres in man: Review of four explanted whole livers". In: *International Journal of Radiation Oncology∗Biology∗Physics* 60.5, pp. 1552–1563.

Kim, Minho et al. (2019a). "Effects of collimator on imaging performance of Yttrium-90 Bremsstrahlung photons: Monte Carlo simulation". In: *Nuclear Engineering and Technology* 51.2, pp. 539–545. DOI: 10.1016/j.net.2018.11.007.

Kim, S. P. et al. (2019b). "A guide to (90)Y radioembolization and its dosimetry". In: *Phys Med* 68, pp. 132–145. ISSN: 1724-191X (Electronic) 1120-1797 (Linking). DOI: 10.1016/j.ejmp.2019.09.236.

Kis, Bela, Matthew Mills, and Sarah E. Hoffe (Sept. 2016). "Hepatic radioembolization from transradial access: initial experience and comparison to transfemoral access". In: *Diagnostic and Interventional Radiology* 22.5, pp. 444–449.

Koran, Mary Ellen et al. (Nov. 2016). "Five percent dextrose maximizes dose delivery of Yttrium-90 resin microspheres and reduces rates of premature stasis compared to sterile water". In: *Biomedical Reports* 5.6, pp. 745–748.

Lam, M. G. and M. L. Smits (2013). "Value of 99mTc-macroaggregated albumin SPECT for radioembolization treatment planning". In: *J Nucl Med* 54.9, pp. 1681–2. ISSN: 1535-5667 (Electronic), 0161-5505 (Linking).

Lam, M. G. et al. (2013). "Safety of repeated yttrium-90 radioembolization". In: *Cardiovasc Intervent Radiol* 36.5, pp. 1320–8. ISSN: 1432-086X (Electronic), 0174-1551 (Linking).

Lam, M. G. et al. (2014). "Limitations of body surface area-based activity calculation for radioembolization of hepatic metastases in colorectal cancer". In: *J Vasc Interv Radiol* 25.7, pp. 1085–93. ISSN: 1535-7732 (Electronic), 1051-0443 (Linking). DOI: 10.1016/j.jvir.2013.11.018.

Lanconelli, N et al. (Jan. 2012). "A free database of radionuclide voxel S values for the dosimetry of nonuniform activity distributions". In: *Physics in Medicine and Biology* 57.2, pp. 517–533. DOI: 10.1088/0031-9155/57/2/517.

Lau, Wan-Yee et al. (Jan. 2012). "Patient Selection and Activity Planning Guide for Selective Internal Radiotherapy With Yttrium-90 Resin Microspheres". In: *International Journal of Radiation Oncology∗Biology∗Physics* 82.1, pp. 401–407.

Leung, T. W. et al. (1995). "Radiation pneumonitis after selective internal radiation treatment with intraarterial 90yttrium-microspheres for inoperable hepatic tumors". In: *Int J Radiat Oncol Biol Phys* 33.4, pp. 919–24. ISSN: 0360-3016 (Print), 0360-3016 (Linking). DOI: 10.1016/0360-3016(95)00039-3.

Leung, W. T. et al. (1994). "Measuring lung shunting in hepatocellular carcinoma with intrahepatic-arterial technetium-99m macroaggregated albumin". In: *J Nucl Med* 35.1, pp. 70–3.

Lewandowski, R. J. et al. (2014). "Sustained safety and efficacy of extended-shelf-life (90)Y glass microspheres: long-term follow-up in a 134-patient cohort". In: *Eur J Nucl Med Mol Imaging* 41.3, pp. 486–93. ISSN: 1619-7089 (Electronic), 1619-7070 (Linking).

Lewandowski, R. J. et al. (2016). "(90) Y radiation lobectomy: Outcomes following surgical resection in patients with hepatic tumors and small future liver remnant volumes". In: *J Surg Oncol* 114.1, pp. 99–105. DOI: 10.1002/jso.24269.

Lhommel, R. et al. (2009). "Yttrium-90 TOF PET scan demonstrates high-resolution biodistribution after liver SIRT". In: *Eur J Nucl Med Mol Imaging* 36.10, p. 1696. ISSN: 1619-7089 (Electronic), 1619-7070 (Linking).

Li, T. et al. (2017). "Quantitative Imaging for Targeted Radionuclide Therapy Dosimetry - Technical Review". In: *Theranostics* 7.18, pp. 4551–4565. ISSN: 1838-7640 (Electronic), 1838-7640 (Linking).

Ljungberg, Michael and Katarina Sjögreen-Gleisner (2011). "The accuracy of absorbed dose estimates in tumours determined by Quantitative SPECT: A Monte Carlo study". In: *Acta Oncologica* 50.6, pp. 981–989. DOI: 10.3109/0284186x.2011.584559.

Lopez, B. et al. (2019). "Calculation of lung mean dose and quantification of error for (90) Y-microsphere radioembolization using (99m) Tc-MAA SPECT/CT and diagnostic chest CT". In: *Med Phys* 46.9, pp. 3929–3940. DOI: 10.1002/mp.13575.

Marcatili, S et al. (Mar. 2013). "Development and validation of RAYDOSE: a Geant4-based application for molecular radiotherapy". In: *Physics in Medicine and Biology* 58.8, pp. 2491–2508. DOI: 10.1088/0031-9155/58/8/2491.

Michels, Nicholas A. (Sept. 1966). "Newer anatomy of the liver and its variant blood supply and collateral circulation". In: *The American Journal of Surgery* 112.3, pp. 337–347.

Mikell, J. K. et al. (2015a). "Comparing voxel-based absorbed dosimetry methods in tumors, liver, lung, and at the liver-lung interface for (90)Y microsphere selective

internal radiation therapy". In: *EJNMMI Phys* 2.1, p. 16. ISSN: 2197-7364 (Print), 2197-7364 (Linking).

Mikell, J. K. et al. (2015b). "Comparing voxel-based absorbed dosimetry methods in tumors, liver, lung, and at the liver-lung interface for (90)Y microsphere selective internal radiation therapy". In: *EJNMMI Phys* 2.1, p. 16. ISSN: 2197-7364 (Print) 2197-7364 (Linking). DOI: 10.1186/s40658-015-0119-y.

Mikell, J. K. et al. (2016). "Selective Internal Radiation Therapy With Yttrium-90 Glass Microspheres: Biases and Uncertainties in Absorbed Dose Calculations Between Clinical Dosimetry Models". In: *Int J Radiat Oncol Biol Phys* 96.4, pp. 888–896. ISSN: 1879-355X (Electronic), 0360-3016 (Linking). DOI: 10.1016/j.ijrobp.2016.07.021.

Nuclear Medicine Physics (2015). Non-serial Publications. Vienna: INTERNATIONAL ATOMIC ENERGY AGENCY. ISBN: 978-92-0-143810-2.

Pacilio, Massimiliano et al. (2015). "Differences in 3D dose distributions due to calculation method of voxel S-values and the influence of image blurring in SPECT". In: *Physics in Medicine and Biology* 60.5, pp. 1945–1964. DOI: 10.1088/0031-9155/60/5/1945.

Package Insert (2016). Report. Sirtex Medical Limited.

Package Insert- Therapshere Yttrium-90 Glass Microspheres. Report. Biocompatibles UK Ltd, a BTG International group company.

Pasciak, A. S., A. C. Bourgeois, and Y. C. Bradley (2014). "A Comparison of Techniques for (90)Y PET/CT Image-Based Dosimetry Following Radioembolization with Resin Microspheres". In: *Front Oncol* 4, p. 121. ISSN: 2234-943X (Print) 2234-943X (Linking). DOI: 10.3389/fonc.2014.00121.

– (2016). "A Microdosimetric Analysis of Absorbed Dose to Tumor as a Function of Number of Microspheres per Unit Volume in 90Y Radioembolization". In: *J Nucl Med* 57.7, pp. 1020–6. ISSN: 1535-5667 (Electronic), 0161-5505 (Linking).

Pasciak, A. S. and W. D. Erwin (2009). "Effect of voxel size and computation method on Tc-99m MAA SPECT/CT-based dose estimation for Y-90 microsphere therapy".

In: *IEEE Trans Med Imaging* 28.11, pp. 1754–8. ISSN: 1558-254X (Electronic) 0278-0062 (Linking). DOI: 10.1109/TMI.2009.2022753.

Physics in Nuclear Medicine (2012). Elsevier. DOI: 10.1016/c2009-0-51635-2.

Podgoršak, Ervin B et al. (2006). *Radiation physics for medical physicists*. Springer.

Porter, Charlotte A. et al. (2018). "Phantom and clinical evaluation of the effect of full Monte Carlo collimator modelling in post-SIRT yttrium-90 Bremsstrahlung SPECT imaging". In: *EJNMMI Research* 8.1. DOI: 10.1186/s13550-018-0361-0.

Potrebko, Peter S. et al. (2018). "SPECT/CT image-based dosimetry for Yttrium-90 radionuclide therapy: Application to treatment response". In: *Journal of Applied Clinical Medical Physics* 19.5, pp. 435–443. ISSN: 2473-4209 (Electronic) 0094-2405 (Linking). DOI: 10.1002/acm2.12400.

Quantitative Nuclear Medicine Imaging: Concepts, Requirements and Methods (2014). Human Health Reports 9. Vienna: INTERNATIONAL ATOMIC ENERGY AGENCY. ISBN: 978-92-0-141510-3.

Riaz, A. et al. (2011). "Radiation segmentectomy: a novel approach to increase safety and efficacy of radioembolization". In: *Int J Radiat Oncol Biol Phys* 79.1, pp. 163–71. DOI: 10.1016/j.ijrobp.2009.10.062.

Riaz, Ahsun, Rafia Awais, and Riad Salem (July 2014). "Side Effects of Yttrium-90 Radioembolization". In: *Frontiers in Oncology* 4.

Roeske, John C. et al. (Sept. 2008). "Small-Scale Dosimetry: Challenges and Future Directions". In: *Seminars in Nuclear Medicine* 38.5, pp. 367–383.

Rong, X., Y. Du, and E. C. Frey (2012a). "A method for energy window optimization for quantitative tasks that includes the effects of model-mismatch on bias: application to Y-90 bremsstrahlung SPECT imaging". In: *Phys Med Biol* 57.12, pp. 3711–25. ISSN: 1361-6560 (Electronic), 0031-9155 (Linking).

Rong, X. et al. (2012). "Development and evaluation of an improved quantitative (90)Y bremsstrahlung SPECT method". In: *Med Phys* 39.5, pp. 2346–58. ISSN: 0094-2405 (Print), 0094-2405 (Linking).

Rong, Xing, Yong Du, and Eric C Frey (May 2012b). "A method for energy window optimization for quantitative tasks that includes the effects of model-mismatch on bias: application to Y-90 bremsstrahlung SPECT imaging". In: *Physics in Medicine and Biology* 57.12, pp. 3711–3725. DOI: 10.1088/0031-9155/57/12/3711.

Salem, Riad and Kenneth G. Thurston (Aug. 2006). "Radioembolization with 90Yttrium Microspheres: A State-of-the-Art Brachytherapy Treatment for Primary and Secondary Liver Malignancies". In: *Journal of Vascular and Interventional Radiology* 17.8, pp. 1251–1278.

Salem, Riad et al. (May 2019). "Clinical and dosimetric considerations for Y90: recommendations from an international multidisciplinary working group". In: *European Journal of Nuclear Medicine and Molecular Imaging* 46.8, pp. 1695–1704. DOI: 10.1007/s00259-019-04340-5. URL: https://doi.org/10.1007/s00259-019-04340-5.

Seidensticker, R. et al. (2012). "Hepatic toxicity after radioembolization of the liver using (90)Y-microspheres: sequential lobar versus whole liver approach". In: *Cardiovasc Intervent Radiol* 35.5, pp. 1109–18. DOI: 10.1007/s00270-011-0295-7.

Shepp, L. A. and Y. Vardi (1982). "Maximum Likelihood Reconstruction for Emission Tomography". In: *IEEE Transactions on Medical Imaging* 1.2, pp. 113–122. DOI: 10.1109/TMI.1982.4307558.

Siman, W., J. K. Mikell, and S. C. Kappadath (2016a). "Practical reconstruction protocol for quantitative (90)Y bremsstrahlung SPECT/CT". In: *Med Phys* 43.9, p. 5093. ISSN: 2473-4209 (Electronic) 0094-2405 (Linking). DOI: 10.1118/1.4960629.

– (2016b). "Practical reconstruction protocol for quantitative (90)Y bremsstrahlung SPECT/CT". In: *Med Phys* 43.9, p. 5093. ISSN: 2473-4209 (Electronic), 0094-2405 (Linking).

Siman, W. et al. (2020). "Systematic and random errors of PET-based (90) Y 3D dose quantification". In: *Med Phys* 47.6, pp. 2441–2449. ISSN: 0094-2405. DOI: 10.1002/mp.14117.

Smits, M. L. et al. (2015). "Radioembolization dosimetry: the road ahead". In: *Cardiovasc Intervent Radiol* 38.2, pp. 261–9. ISSN: 1432-086X (Electronic), 0174-1551 (Linking). DOI: 10.1007/s00270-014-1042-7.

Song, Y. S. et al. (2015). "PET/CT-Based Dosimetry in 90Y-Microsphere Selective Internal Radiation Therapy: Single Cohort Comparison With Pretreatment Planning on (99m)Tc-MAA Imaging and Correlation With Treatment Efficacy". In: *Medicine (Baltimore)* 94.23, e945. ISSN: 1536-5964 (Electronic), 0025-7974 (Linking).

Srinivas, Shyam M. et al. (Oct. 2014). "Determination of Radiation Absorbed Dose to Primary Liver Tumors and Normal Liver Tissue Using Post-Radioembolization 90Y PET". In: *Frontiers in Oncology* 4.

Strigari, L. et al. (Aug. 2010). "Efficacy and Toxicity Related to Treatment of Hepatocellular Carcinoma with 90Y-SIR Spheres: Radiobiologic Considerations". In: *Journal of Nuclear Medicine* 51.9, pp. 1377–1385.

Tai, Wai Meng David et al. (May 2020). "A phase II open-label, single-center, nonrandomized trial of Y90-radioembolization in combination with nivolumab in Asian patients with advanced hepatocellular carcinoma: CA 209-678." In: *Journal of Clinical Oncology* 38.15_suppl, pp. 4590–4590. DOI: 10.1200/jco.2020.38.15_suppl.4590.

Uliel, L. et al. (Nov. 2012a). "From the Angio Suite to the -Camera: Vascular Mapping and 99mTc-MAA Hepatic Perfusion Imaging Before Liver Radioembolization–A Comprehensive Pictorial Review". In: *Journal of Nuclear Medicine* 53.11, pp. 1736–1747.

– (2012b). "From the angio suite to the gamma-camera: vascular mapping and 99mTc-MAA hepatic perfusion imaging before liver radioembolization–a comprehensive pictorial review". In: *J Nucl Med* 53.11, pp. 1736–47. ISSN: 1535-5667 (Electronic) 0161-5505 (Linking). DOI: 10.2967/jnumed.112.105361.

Ulrich, G. et al. (2013). "Predictive value of intratumoral 99mTc-macroaggregated albumin uptake in patients with colorectal liver metastases scheduled for radioembolization with 90Y-microspheres". In: *J Nucl Med* 54.4, pp. 516–22. ISSN: 1535-5667 (Electronic), 0161-5505 (Linking).

Van Audenhaege, K. et al. (2015). "Review of SPECT collimator selection, optimization, and fabrication for clinical and preclinical imaging". In: *Med Phys* 42.8, pp. 4796–813. ISSN: 2473-4209 (Electronic), 0094-2405 (Linking).

Vauthey, J. N. et al. (2002). "Body surface area and body weight predict total liver volume in Western adults". In: *Liver Transpl* 8.3, pp. 233–40. ISSN: 1527-6465 (Print), 1527-6465 (Linking). DOI: 10.1053/jlts.2002.31654.

Vesselle, G. et al. (June 2015). "Radioembolization with yttrium-90 microspheres work up: Practical approach and literature review". In: *Diagnostic and Interventional Imaging* 96.6, pp. 547–562.

Vollmar, Brigitte and Michael D. Menger (Oct. 2009). "The Hepatic Microcirculation: Mechanistic Contributions and Therapeutic Targets in Liver Injury and Repair". In: *Physiological Reviews* 89.4, pp. 1269–1339.

Vouche, M. et al. (2013). "Radiation lobectomy: time-dependent analysis of future liver remnant volume in unresectable liver cancer as a bridge to resection". In: *J Hepatol* 59.5, pp. 1029–36. DOI: 10.1016/j.jhep.2013.06.015.

Walrand, S. et al. (2014a). "A hepatic dose-toxicity model opening the way toward individualized radioembolization planning". In: *J Nucl Med* 55.8, pp. 1317–22. ISSN: 1535-5667 (Electronic), 0161-5505 (Linking).

Walrand, S. et al. (2014b). "The low hepatic toxicity per Gray of 90Y glass microspheres is linked to their transport in the arterial tree favoring a nonuniform trapping as observed in posttherapy PET imaging". In: *J Nucl Med* 55.1, pp. 135–40. ISSN: 1535-5667 (Electronic), 0161-5505 (Linking).

Walters, B. R. B., I. Kawrakow, and D. W. O. Rogers (Nov. 2002). "History by history statistical estimators in theBEAMcode system". In: *Medical Physics* 29.12, pp. 2745–2752. DOI: 10.1118/1.1517611.

White, D. R., R. V. Griffith, and I. J. Wilson (1992). "Report 46". In: *Journal of the International Commission on Radiation Units and Measurements* os24.1, NP–NP. DOI: 10.1093/jicru/os24.1.report46.

Wiele, Christophe Van de et al. (July 2012). "SIRT of liver metastases: physiological and pathophysiological considerations". In: *European Journal of Nuclear Medicine and Molecular Imaging* 39.10, pp. 1646–1655.

Willowson, K. P. et al. (2015). "A multicentre comparison of quantitative (90)Y PET/CT for dosimetric purposes after radioembolization with resin microspheres : The QUEST Phantom Study". In: *Eur J Nucl Med Mol Imaging* 42.8, pp. 1202–22. ISSN: 1619-7089 (Electronic), 1619-7070 (Linking).

Wondergem, M. et al. (2013). "99mTc-macroaggregated albumin poorly predicts the intrahepatic distribution of 90Y resin microspheres in hepatic radioembolization". In: *J Nucl Med* 54.8, pp. 1294–301. DOI: 10.2967/jnumed.112.117614.

Yue, J. et al. (2016). "Comparison of quantitative Y-90 SPECT and non-time-of-flight PET imaging in post-therapy radioembolization of liver cancer". In: *Med Phys* 43.10, p. 5779. ISSN: 2473-4209 (Electronic), 0094-2405 (Linking).